

Assessment of the global impact of aerosols on tropospheric oxidants

Xuexi Tie,¹ Sasha Madronich,¹ Stacy Walters,¹ David P. Edwards,¹ Paul Ginoux,² Natalie Mahowald,¹ RenYi Zhang,³ Chao Lou,⁴ and Guy Brasseur^{1,5}

Received 17 August 2004; revised 27 October 2004; accepted 24 November 2004; published 10 February 2005.

[1] We present here a fully coupled global aerosol and chemistry model for the troposphere. The model is used to assess the interactions between aerosols and chemical oxidants in the troposphere, including (1) the conversion from gas-phase oxidants into the condensed phase during the formation of aerosols, (2) the heterogeneous reactions occurring on the surface of aerosols, and (3) the effect of aerosols on ultraviolet radiation and photolysis rates. The present study uses the global three-dimensional chemical/transport model, Model for Ozone and Related Chemical Tracers, version 2 (MOZART-2), in which aerosols are coupled with the model. The model accounts for the presence of sulfate, soot, primary organic carbon, ammonium nitrate, secondary organic carbon, sea salt, and mineral dust particles. The simulated global distributions of the aerosols are analyzed and evaluated using satellite measurements (Moderate-Resolution Imaging Spectroradiometer (MODIS)) and surface measurements. The results suggest that in northern continental regions the tropospheric aerosol loading is highest in Europe, North America, and east Asia. Sulfate, organic carbon, black carbon, and ammonium nitrate are major contributions for the high aerosol loading in these regions. Aerosol loading is also high in the Amazon and in Africa. In these areas the aerosols consist primarily of organic carbon and black carbon. Over the southern high-latitude ocean (around 60°S), high concentrations of sea-salt aerosol are predicted. The concentration of mineral dust is highest over the Sahara and, as a result of transport, spread out into adjacent regions. The model and MODIS show similar geographical distributions of aerosol particles. However, the model overestimates the sulfate and carbonaceous aerosol in the eastern United States, Europe, and east Asia. In the region where aerosol loading is high, aerosols have important impacts on tropospheric ozone and other oxidants. The model suggests that heterogeneous reactions of HO₂ and CH₂O on sulfate have an important impact on HO_x (OH + HO₂) concentrations, while the heterogeneous reaction of O₃ on soot has a minor effect on O₃ concentrations in the lower troposphere. The heterogeneous reactions on dust have very important impacts on HO_x and O₃ in the region of dust mobilization, where the reduction of HO_x and O₃ concentrations can reach a maximum of 30% and 20%, respectively, over the Sahara desert. Dust, organic carbon, black carbon, and sulfate aerosols have important impacts on photolysis rates. For example, the photodissociation frequencies of ozone and nitrogen dioxide are reduced by 20% at the surface in the Sahara, in the Amazon, and in eastern Asia, leading to 5–20% reduction in the concentration of HO_x and to a few percent change in the O₃ abundance in these regions.

Citation: Tie, X., S. Madronich, S. Walters, D. P. Edwards, P. Ginoux, N. Mahowald, R. Zhang, C. Lou, and G. Brasseur (2005), Assessment of the global impact of aerosols on tropospheric oxidants, *J. Geophys. Res.*, *110*, D03204, doi:10.1029/2004JD005359.

¹National Center for Atmospheric Research, Boulder, Colorado, USA.

²Geophysical Fluid Dynamics Laboratory, NOAA, Princeton, New Jersey, USA.

³Department of Atmospheric Science, Texas A&M University, College Station, Texas, USA.

⁴Institute for Computational Earth Systems Science, University of California, Santa Barbara, California, USA.

⁵Also at Max Planck Institute of Meteorology, Hamburg, Germany.

1. Introduction

[2] Tropospheric aerosols have received increasing recognition regarding their importance in climate change and climate prediction. The focus of the present study is to understand the impact of aerosols on tropospheric oxidants. In past years, several effects of aerosols on tropospheric chemistry have been studied. For example, hydrolysis of N₂O₅ on sulfate aerosols was examined by *Dentener et al.* [1993] and more recently by *Tie et al.* [2001a], showing a significant impact on the tropospheric NO_x and O₃ budgets,

although the effect is limited to high latitudes in the Northern Hemisphere. Subsequently, field observations during Tropospheric Ozone Production about the Spring Equinox (TOPSE) provided evidence that hydrolysis of N_2O_5 affects substantially the budget of NO_x in the remote regions of the northern high latitudes during winter [Tie *et al.*, 2003a]. Dentener and Crutzen [1996] studied the role of mineral dust aerosol as a reactive surface in the troposphere. Their study showed that, although the heterogeneous reaction rates on mineral dust are highly uncertain, the interaction of N_2O_5 , O_3 , and HO_2 with mineral dust could produce a 10% decrease in O_3 nearby the mineral dust areas. Jacob [2000], Tie *et al.* [2001a], and Martin *et al.* [2003] discussed the atmospheric impact of the heterogeneous reaction of HO_2 on sulfate aerosol. Their results suggest that aerosol uptake of HO_2 significantly affects the HO_x budget in the lower troposphere. The impact of aerosol on ultraviolet (UV) radiation and photolysis rates has been studied by He and Carmichael [1999] and by Liao *et al.* [1999]. Recent developments of global model simulations facilitate a more detailed investigation of the photochemical effects of aerosols on tropospheric O_3 and OH [Martin *et al.*, 2003; Liao *et al.*, 2003; Bian and Zender, 2003]. Martin *et al.* [2003], for example, use precalculated global aerosol distributions to evaluate the sensitivity of tropospheric OH, O_3 , and ozone precursors to the photochemical effects resulting from the presence of aerosols. Liao *et al.* [2003] use a more advanced coupled aerosol and photochemical model to study the interactions between aerosol and chemical oxidants. Bian and Zender [2003] investigate the impact of mineral dust on the tropospheric photochemistry. Their results show that tropospheric oxidants such as O_3 and HO_x can be significantly affected by aerosols at regional scales through the aerosol effects of photolysis and heterogeneous reactions.

[3] Aerosols can potentially interact with many compartments of the surface-atmosphere system. These include direct modification of the atmospheric radiative budget as well as more complex perturbations of the hydrological cycle, as aerosol can induce changes in the formation of clouds and precipitation, which in turn can affect aerosol removal. Wet deposition of aerosol ammonium can contribute to the biogenic nitrogen cycles of the surface [Hansson and Holmen, 2001]. Changes in climate, esp. those in temperature and general circulation, can in turn produce significant impacts on tropospheric aerosol and chemical oxidants.

[4] In order to study the interaction between aerosols, climate, and oxidants, we have developed a global chemical/transport/aerosol model. The model is an upgrade of the Model for Ozone and Related Chemical Tracers, version 2 (MOZART-2), chemical transport model [Horowitz *et al.*, 2003]. It includes the standard MOZART-2 chemistry scheme, a dynamical module (Model of Atmospheric Transport and Chemistry (MATCH) [Rasch *et al.*, 1997]) that calculates the hydrological cycle with cloudiness and precipitation, a coupled aerosol model that provides the distribution of various types of aerosols, and a radiative transfer model (Tropospheric Ultraviolet Visible (TUV), developed at NCAR) that calculates photolysis rates [Madronich, 1987]. By integrating these different components, the model provides information on the interactions between aerosols

and oxidants, and on the impact of future chemical emissions and climate change on the distribution and abundance of aerosols and oxidants.

[5] In section 2, we describe the model adopted for the present study. In section 3, the model formation adopted for each type of aerosols is described more specifically, and the calculated global distributions of aerosol loadings are presented. In section 4, calculated aerosol abundances are compared to satellite and surface measurements. In section 5, the impact of aerosols on oxidants is discussed.

2. Description of Upgraded MOZART-2

[6] MOZART-2 is a global chemical transport model developed at NCAR together with the NOAA Geophysical Fluid Dynamics Laboratory (Princeton), and the Max Planck Institute of Meteorology (Hamburg). It simulates the distribution of tropospheric ozone and its chemical precursors. In its standard configuration, MOZART-2 calculates the concentrations of 63 chemical species from the surface up to the middle stratosphere. It can use meteorological inputs derived from either a general circulation model or from meteorological analyses. MOZART-2 is described by Horowitz *et al.* [2003], who provided an extensive evaluation of the model including a comparison of calculated concentrations with CMDL surface measurements (CO and O_3), global O_3 sonde data, and measurements from aircraft (O_3 , CO , NO_x , PAN, HNO_3 , various NMHC, CH_2O , etc.).

[7] The “standard” MOZART-2 is developed in the framework of the transport model Model of Atmospheric Transport and Chemistry (MATCH) [Rasch *et al.*, 1997], which includes a representation of advection, convective transport, boundary layer mixing, and wet and dry deposition. Surface emissions of chemical species include those from fossil fuel and industrial activity, biomass burning, biogenic emissions from vegetation and soils, and oceanic emissions. Aircraft emissions of NO_x and CO are included in the model, based on Friedl [1997]. The chemical scheme used in MOZART-2 accounts for the oxidation of ethane, propane, ethene, propene, isoprene, α -pinene (as a surrogate for all terpenes), and n-butane (as a surrogate for all hydrocarbons with 4 or more carbons, excluding isoprene and terpenes). Heterogeneous reactions of N_2O_5 and NO_3 on sulfate aerosols are included, using a prescribed sulfate aerosol distribution [Tie *et al.*, 2001a]. Photolysis frequencies are calculated using a precalculated “lookup” table [Brasseur *et al.*, 1998]. The adopted source of NO_x from lightning is 4 TgN/y for the present day climate, distributed according to the location of convective clouds, and based on the parameterization of Price *et al.* [1997] with a “C-shaped” vertical profile [Pickering *et al.*, 1998].

[8] The model has been applied in numerous scientific studies, including the analysis of data obtained from field campaigns and satellite observations, and the impacts of physical and chemical processes on tropospheric oxidants and ozone distributions. Brasseur *et al.* [1998], Hauglustaine *et al.* [1998], and Horowitz *et al.* [2003] provide a detailed model description and evaluation. The impacts of biomass burning, NO_x production from lightning, and aerosols on tropospheric oxidants have also been investigated by Hauglustaine *et al.* [1999, 2001] and Tie *et al.* [2001a,

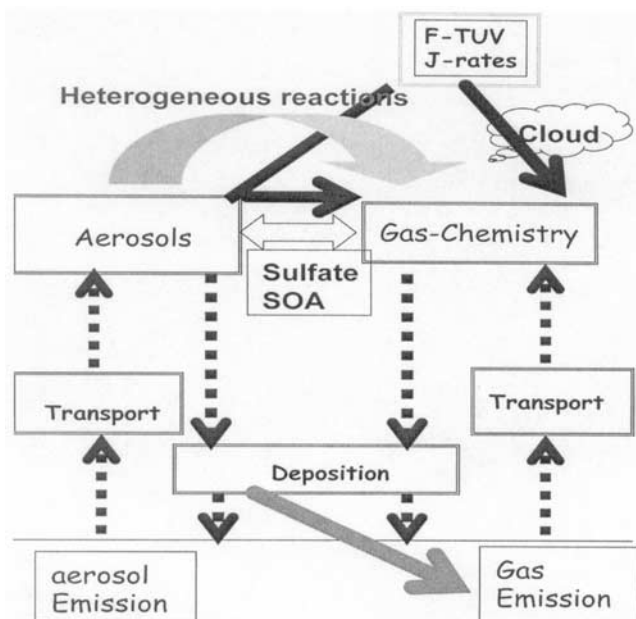


Figure 1. Schematic representation of the structure adopted for the MOZART-2 model. The dotted arrows show the connections among the different components of the model. The white arrow represents the conversion from gas-phase oxidants into the condensed phase during the formation of aerosols; the light gray arrow highlights the heterogeneous reactions occurring on the surface of aerosols; the black arrows represent the effects of aerosols on ultraviolet radiation and on photolysis rates; and the dark gray arrow represents the effects of aerosol on the surface deposition of nitrogen.

2001b, 2002]. MOZART-2 has been used to study the ozone and NO_x budget over east Asia and over the United States [Mauzerall *et al.*, 2000; Zhang *et al.*, 2003], the effect of cloud droplets and biogenic methanol on the tropospheric oxidants [Tie *et al.*, 2003b, 2003c], and to analyze field campaign data and satellite observations, including TRACE-A, TRACE-P, TOPSE and MAPS [Cunnold *et al.*, 2002; Emmons *et al.*, 2000, 2003; Lamarque and Hess, 2003; Lamarque *et al.*, 1999; Tie *et al.*, 2003a; Edwards *et al.*, 2003].

[9] For this study, we will use a new version of MOZART-2, in which (1) the “look-up” photolysis tables have been replaced by an online radiative transfer model (NCAR’s Tropospheric Ultraviolet Visible model (TUV)) [Madronich, 1987], and (2) the aerosol distributions have been explicitly calculated. This model setting is appropriate to address the question of aerosol/oxidant interactions in the troposphere.

[10] The TUV model has been implemented in MOZART-2 with some modifications from the original version. In order to be optimized on the NCAR computer architecture, the TUV model has been simplified and is now called “fast TUV” (FTUV). FTUV includes the same physical processes, except that the number of wavelength bins between 121 and 750 nm has been reduced from 140 to 17. As a result, FTUV is about 8 times faster than the original TUV. The differences in the calculated photolysis

frequencies between TUV and FTUV are in most cases smaller than 5% in the troposphere. With the coupling of the FTUV model into MOZART-2, the impact of cloud and aerosol particles on photolysis frequencies can be simulated. A mixed random and maximum overlap method [Stubenrauch *et al.*, 1997] for subgrid cloud vertical distributions is used. The details of the FTUV model and the application in studying the effect of clouds photolysis and oxidants are given by Tie *et al.* [2003b].

[11] The distributions of sulfate and soot aerosols calculated with an early version of the model (MOZART-1) have been compared previously with observations and other global models [Tie *et al.*, 2001a; Intergovernmental Panel on Climate Change (IPCC), 2001]. More recently, we have added primary organic carbon, ammonium nitrate, sea-salt, and secondary organic aerosols to the aerosol scheme. Mineral dust is included in the MATCH model with the same transport scheme and dynamical inputs as used in MOZART-2. The calculated concentrations of dust are included to study the effect of its surface reactions and radiation perturbations on tropospheric oxidants. Figure 1 shows the model structure and the interactions between aerosols and chemical oxidants considered in MOZART-2. This integrated model account for the conversion from gas-phase oxidants into the condensed phase during the formation of aerosols (white arrow), the heterogeneous reactions occurring on the surface of aerosols (light gray arrow), the effect of aerosols on ultraviolet radiation and photolysis rates (black arrow), and the effects of aerosol on the surface deposition of nitrogen (dark gray arrow). In this calculation, the interaction between chemistry and aerosols is fully coupled.

3. Aerosol Model and Global Aerosol Simulation

[12] In this section, we will briefly describe the chemical and physical processes that affect sulfate, ammonium nitrate, organic carbon, secondary organic carbon, black carbon, sea-salt, and mineral dust aerosols. We also present some calculated global aerosol distributions.

3.1. Sulfate

[13] Sulfate (SO₄²⁻) is formed by gas phase reaction and by aqueous phase conversion of SO₂ in cloud droplets. The reactions and reaction rate constants and gas-aqueous equilibrium constants (Henry law constants) are the same as the rates given by Tie *et al.* [2001a]. The rate of reaction S(IV) (the sum of HSO₃⁻ and SO₃²⁻ ions dissolved in the aqueous phase) with O₃ depends strongly on pH values in clouds. The pH values are also calculated online in the model as follows:

$$\text{pH} = -\log[\text{H}^+]$$

where

$$[\text{H}^+] + [\text{NH}_4^+] = [\text{OH}^-] + [\text{HCO}_3^-] + [\text{NO}_3^-] + [\text{HSO}_3^-] + 2[\text{SO}_4^{2-}]$$

Here [OH⁻] accounts for the dissociation of pure water, while [HCO₃⁻] results from the presence of dissolved carbon

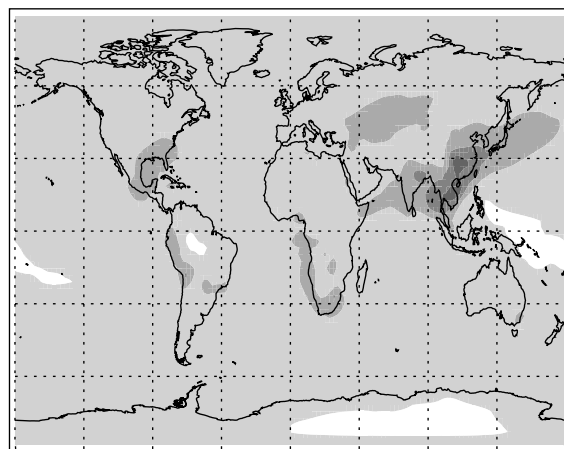
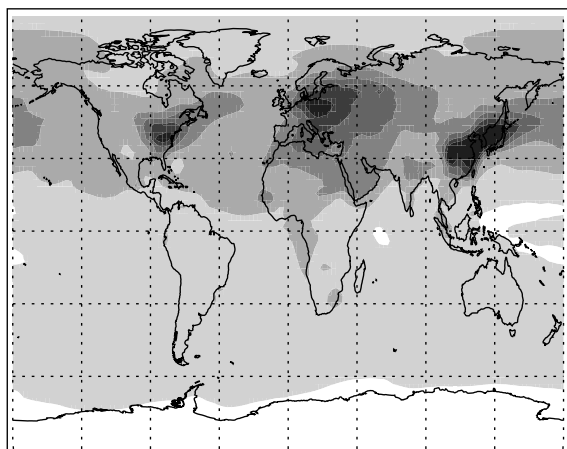
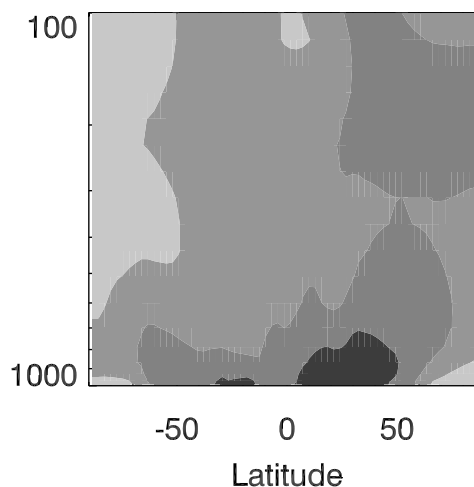
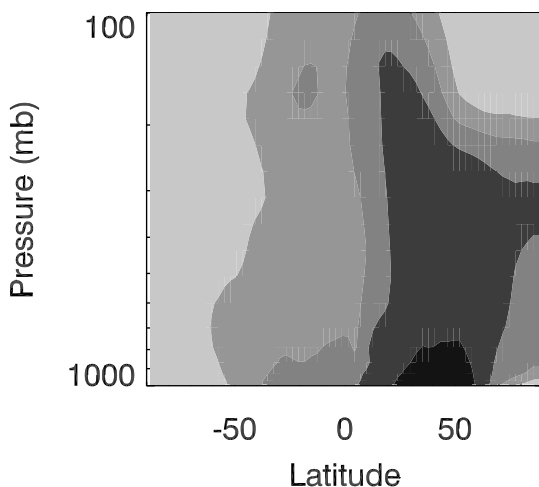
SO₄ Column (mg/m²) (June)SO₄ Column (mg/m²) (Dec.)Zonal SO₄ (pptv) (June)Zonal SO₄ (pptv) (Dec)

Figure 2. (top) Calculated sulfate tropospheric column loadings (mg/m²) and (bottom) zonally averaged sulfate volume mixing ratios (pptv) in June and December.

dioxide in the water droplets; $[\text{NO}_3^-]$ accounts for the effect of nitric acid, and $[\text{NH}_4^+]$ for the effect of ammonia on the overall acidity. The equilibrium constants for the dissolution and dissociation reactions are given by Tie *et al.* [2001a].

[14] SO₂ is emitted predominantly from fuel combustion and industrial activities. In addition to direct emission, SO₂ is also formed from the oxidation of dimethylsulfide (DMS). The reaction and its reaction rates are given by Chin *et al.* [1996]. Global emission inventories for SO₂ are taken from the third IPCC report [IPCC, 2001] and DMS concentrations are calculated on the basis of the surface

emission provided by the International Global Atmospheric Chemistry/Global Emissions Inventory Activity (IGAC/GEIA) [Benkovitz *et al.*, 1994, 1996].

[15] Removal of chemical compounds from the atmosphere is represented by dry deposition and wet scavenging. The dry deposition velocity for sulfate aerosol [Feichter *et al.*, 1996] is assumed to be constant and equal to 0.2 cm/s. The wet deposition scheme includes in-cloud as well as below-cloud scavenging, using the formulation described by Brasseur *et al.* [1998].

[16] In the following sections, the column mass and zonally averaged concentrations of aerosols are shown.

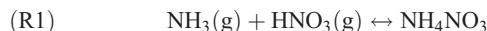
The column mass distribution can be used to examine the horizontal distributions of aerosols averaged over the height of the troposphere, and the zonally averaged concentrations can be used to study vertical and latitudinal distributions of these aerosol particles. The calculated global distributions of column mass of sulfate are shown in Figure 2 (upper panels) for June and December conditions. Significant spatial and temporal variations in the global distribution of sulfate are predicted by the MOZART-2 model. The maximum column mass varies from 15 to 25 mg/m² with the highest values occurring in eastern China, Europe, and the eastern United States, i.e., in regions where the anthropogenic sources of SO₂ are large. Along with the high column mass in these regions, a significant seasonal variability is also predicted with the highest and lowest column mass being found in June and December, respectively. For example, a very small sulfate mass column density (2 to 5 mg/m²) is predicted for the eastern United States in December. In June, the sulfate mass increases rapidly in this region with a maximum of 15 to 25 mg/m². The seasonal variation of the rate of SO₂ oxidation plays an important role in the calculated seasonal cycle of the sulfate mass. During winter, the rate of chemical oxidation of SO₂ is low (very low OH and H₂O₂ concentrations), leading to a lower sulfate production. However, in summer, the oxidation of SO₂ is considerably faster, producing higher sulfate loadings than in winter.

[17] Figure 2 (lower panels) shows that the maximum concentration of sulfate is located in the boundary layer at northern midlatitudes. The lifetime of sulfate aerosols is sufficiently long (about a week [Chin *et al.*, 2000]), to allow convective activity to transport sulfate aerosols from the surface boundary layer into the upper troposphere. The maximum convective transport of sulfate aerosols takes place at midlatitudes in the Northern Hemisphere during June. The zonally averaged sulfate mixing ratio is about 500 pptv at the surface and about 200 pptv at 300 mbar at 40°N (see Figure 1). In December, the convective transport of sulfate is significantly reduced, but remains sufficiently intense (i.e., in frontal systems) to inject about 100 pptv sulfate aerosols at 300 mbar. Compared to the earlier version of MOZART (MOZART version 1), the convective transport of sulfate is stronger in MOZART-2 since a deep convection scheme [Zhang and McFarlane, 1995] has been added to the shallow convective transport scheme [Hack *et al.*, 1993] used in MOZART-1.

3.2. Ammonium Nitrate

[18] Ammonium nitrate aerosols affect the level of tropospheric oxidants in several ways. First, the formation of ammonium nitrate reduces the concentrations of ammonia and plays a key role in determining the pH values in clouds as indicated in equation (3). Second, the deposition of ammonium nitrates provides an important source of nitrogen for the biosphere, and facilitates the surface emission of NO_x and CO₂ [Friedlingstein *et al.*, 1995]. Finally, the formation of ammonium nitrate perturbs the formation of ammonium sulfate, which has an important impact on the degree of acidity in cloud drops. According to Seinfeld and Pandis [1998], the production of ammonium nitrate (NH₄NO₃) results primarily from the reaction

of gas-phase ammonia (NH₃) and nitric acid (HNO₃) through the reaction:



The equilibrium dissociation constant K₇ depends on both temperature and relative humidity, and was calculated by Stelson and Seinfeld [1982]. When the following condition is satisfied,

$$[\text{TN}][\text{TA}] > K_7$$

particles of ammonium nitrate are formed. Here [TN] represents the sum of gas and aqueous phase concentrations of total nitrate ([HNO₃(g)] + [NO₃⁻]), and [TA] is the sum of gas and aqueous phase concentrations of total ammonia ([NH₃(g)] + [NH₄⁺]). The concentration of ammonium nitrate is then calculated as follows:

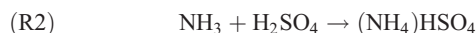
$$[\text{NH}_4\text{NO}_3] = 0.5([\text{TA}] + [\text{TN}] - X_a)$$

where

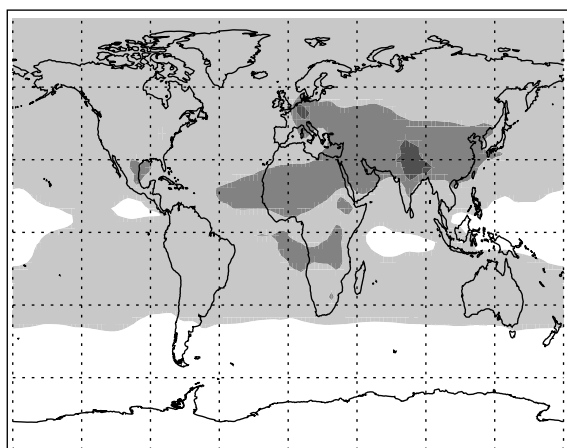
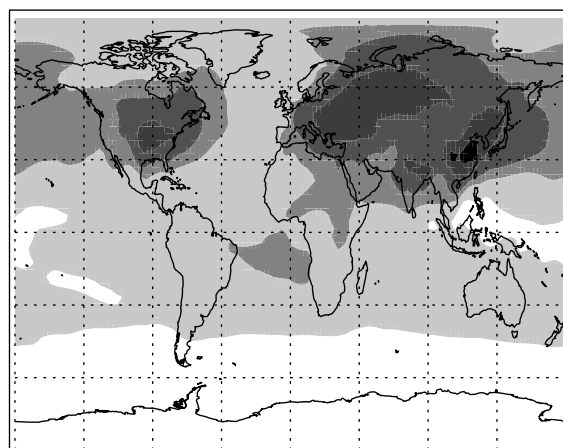
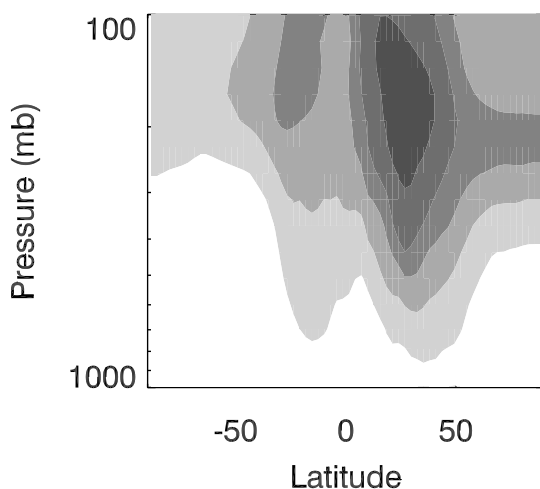
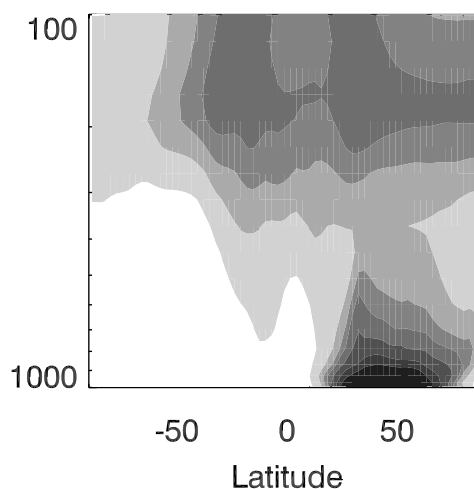
$$X_a = \left\{ ([\text{TA}] + [\text{TN}])^2 - 4([\text{TA}][\text{TN}]) \right\}^{1/2}$$

[19] The ammonium nitrate aerosol is produced by the gas-phase precursors NH₃ and HNO₃, which are calculated online in MOZART-2. HNO₃ is not directly emitted from the surface, but is mainly formed by the reaction of OH + NO₂ in the atmosphere. A detailed analysis of HNO₃ calculation is given by Horowitz *et al.* [2003]. The analysis shows that simulated concentrations of HNO₃ are in reasonable agreement with observations, and that the calculated HNO₃ concentrations are highly sensitive to the parameterization of wet deposition. The primary source of NH₃ is surface emission. Global emission inventories for NH₃ are given by Bouwman *et al.* [1997]. The dominant emission of NH₃ is from animals with 21.5 Tg/yr, followed by fertilizer use (9 Tg/yr), oceanic emissions (8.1 Tg/yr), crop production (3.6 Tg/yr), biomass burning (3.5 Tg/yr), human activities (2.6 Tg/yr), soil emissions (2.4 Tg/yr), and biofuel use (2.1 Tg). Removal of ammonium nitrate from the atmosphere is represented by dry deposition and wet scavenging. The dry deposition velocity for ammonium nitrate is assumed to be constant and equal to the deposition velocity of HNO₃, which is calculated according to Wesely [1989]. The scheme adopted for the in- and below-cloud wet deposition is the same that the scheme used for sulfate aerosol.

[20] In addition to forming aerosol ammonium nitrate, NH₃ can also be converted into ammonium sulfate as suggested by Dentener and Crutzen [1994]:



The rate coefficients K₈ and K₉ are dependent on the sulfate surface area density (A) and the uptake coefficient (γ). The

NH₄NO₃ Column (mg/m²) (June)NH₄NO₃ Column (mg/m²) (Dec.)Zonal NH₄NO₃ (pptv) (June)Zonal NH₄NO₃ (pptv) (Dec)**Figure 3.** Same as Figure 2 but for ammonium nitrate.

global distribution of the sulfate surface area (A) is calculated from the mass of sulfate with an assumed mean radius for the particles. The uptake coefficient (γ) is set to 0.5 following the suggestion of *Dentener and Crutzen* [1994].

[21] The calculated global distributions of ammonium nitrate column mass are shown in Figure 3. There is a significant seasonal variation in the abundance of these particles. In December, the mass of ammonium nitrate is highest in the Northern Hemisphere. The maximum values range from 1 to 6 mg/m² with the highest values occurring in east China, Europe, India, and the eastern United States, which indicates that the higher concentrations of NH₃ and HNO₃ also occur in these regions. This result is similar to the calculation by *Adams et al.* [1999]. In June, the concentrations of ammonium nitrate are substantially lower.

The decrease in the ammonium nitrate abundance is due to the fact that in June the concentrations of sulfate aerosol are highest at middle and high latitudes in the Northern Hemisphere. The highest concentrations of sulfate are located in eastern China, Europe, India, and the eastern United States (see Figure 2), which coincides with the higher ammonia concentrations in these regions. As a result, the gas phase concentrations of ammonia are greatly reduced through conversion to ammonium sulfate, leading to a significant reduction on the formation of ammonium nitrate.

[22] Figure 3 (lower panels) shows the zonally average concentration of ammonium nitrate in June and in December. In December the highest concentrations of ammonium nitrate (zonally averaged concentrations of 50 to 150 pptv) are located between 30 and 60°N. The concentrations decrease rapidly with altitude. This suggests that the con-

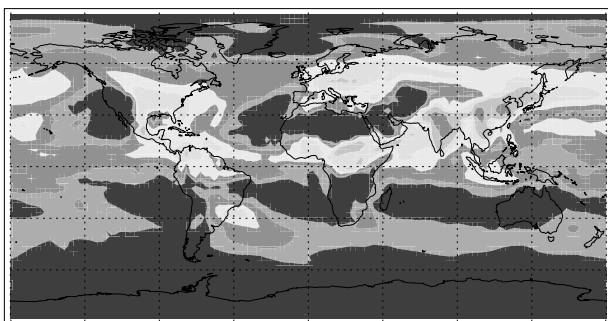
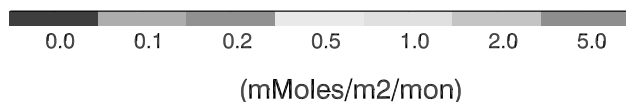
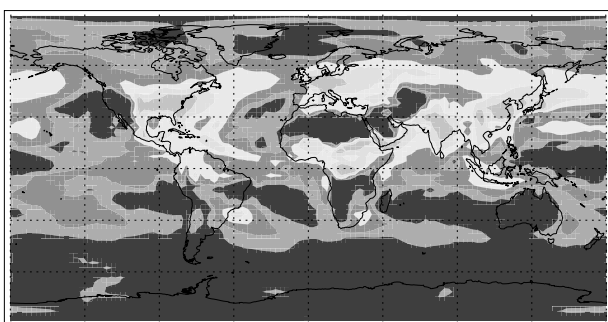
NH₄ Wet DepositionNO₃ Wet Deposition

Figure 4. Calculated global distribution of annually averaged ammonium (NH₄⁺) and nitrate (NO₃⁻) deposition (mmol/m²/month). See color version of this figure at back of this issue.

version of gas-phase ammonia to particle phase ammonium nitrate competes with the conversion of ammonium sulfate. In December the concentrations of sulfate in the boundary layer are smaller. As a result, a larger amount of ammonium nitrate is formed. In June, however, the sulfate concentration increases rapidly in the boundary layer, converting a significant amount of ammonia to ammonium sulfate and resulting in very small production of ammonium nitrate in the boundary layer. In June, most ammonium nitrate is formed in the upper troposphere with a zonally averaged concentration reaching 60 pptv.

[23] The ammonium ions (NH₄⁺) present in ammonium nitrate and ammonium sulfate are deposited to the ground through the washout of ammonium nitrate and ammonium sulfate (wet deposition), providing nitrogen deposition (N) on the surface. Figure 4 shows that the wet deposition of NH₄⁺ (upper panel) provides important N deposition in the eastern United States, the Amazon, southern Africa, Europe, India, and eastern China. The washout of nitric acid and ammonium nitrate (NO₃⁻) provide an additional source of nitrogen to soils (lower panel). The spatial distribution of nitrate deposition is similar to that of ammonium, but with different magnitudes. In eastern China and India, the am-

monium deposition is significantly larger than the nitrate deposition, while in Europe it is only slightly larger. In the Amazon and southern Africa, the deposition of both compounds is comparable. In the eastern United States, the ammonium deposition is smaller than the nitrate deposition. Overall, this calculation shows that ammonium nitrate and ammonium sulfate play an important role in controlling the N deposition on the surface.

[24] Figure 5 compares the calculated nitrate deposition rates with those observed by the National Atmospheric Deposition Program (NADP) [Gilliland *et al.*, 2002] in the United States. Strong seasonal and spatial distributions are seen, with higher deposition rates in July than in January, and higher values in the eastern United States than in the western United States. In July, the highest deposition rates extended to the central United States. The calculated values are seen to be in reasonable agreement with the observation.

3.3. Carbonaceous Aerosols

[25] Three types of carbonaceous aerosol are considered in this study, i.e., organic carbon (OC), including primary and secondary organic carbon aerosol (SOA), and black carbon (BC). BC aerosols are strong absorbers of solar radiation [Liousse *et al.*, 1996] while OC aerosols mainly scatter solar light. Primary organic carbon is directly emitted from biomass burning, fossil fuel, and vegetation [Liousse *et al.*, 1996], while secondary organic carbon is formed through oxidation of atmospheric volatile organic compounds (VOCs). Because of their different physical and chemical characteristics, black carbon, primary organic carbon, and secondary organic carbon play different roles in affecting tropospheric oxidants. Laboratory measurements suggest that heterogeneous reactions occur on the surface of black carbon [Golden and Manion, 1992; Fendel *et al.*, 1995; Rogaski *et al.*, 1997; DeMore *et al.*, 2000]. Black carbon strongly absorbs solar radiation at ultraviolet (UV) and visible wavelengths, which are relevant to the photolysis rates of many oxidants. Generally, organic carbon is more abundant than black carbon in the troposphere, and can also affect UV light and oxidants. As a strong scatterer, it enhances UV above the aerosol layer and reduces UV below it. In addition to the effect on photolysis, secondary organic carbon has also important impacts on its chemical precursors, which involves some important oxidants such as HO_x, NO_x, and O₃ [Lack *et al.*, 2004].

3.3.1. Black Carbon (BC)

[26] The regional black carbon (soot) budget is determined by its emission, sink, and transport. Black carbon is released by the combustion of hydrocarbons [Cooke and Wilson, 1996; Liousse *et al.*, 1996]. Fossil fuel and biomass burning provide therefore the primary emissions for these particles. The global emission of black carbon has been estimated to be 12.3 Tg C/year by Liousse *et al.* [1996], 18 Tg C/year by Cooke and Wilson [1996], and 24 Tg C/year by Penner *et al.* [1993]. The total emission adopted in this study is 12.4 Tg C/year for the year 2000, and is based on the estimation by IPCC [2001].

[27] Two forms of black carbon particles are distinguished in MOZART-2, i.e., hydrophobic and hydrophilic particles. Hydrophobic BC is directly emitted from the surface, and after entering the atmosphere, mixes with other aerosols or cloud drops to form hydrophilic particles

NADP Monthly Mean Nitrate Wet Deposition (mMoles/m²/mon)

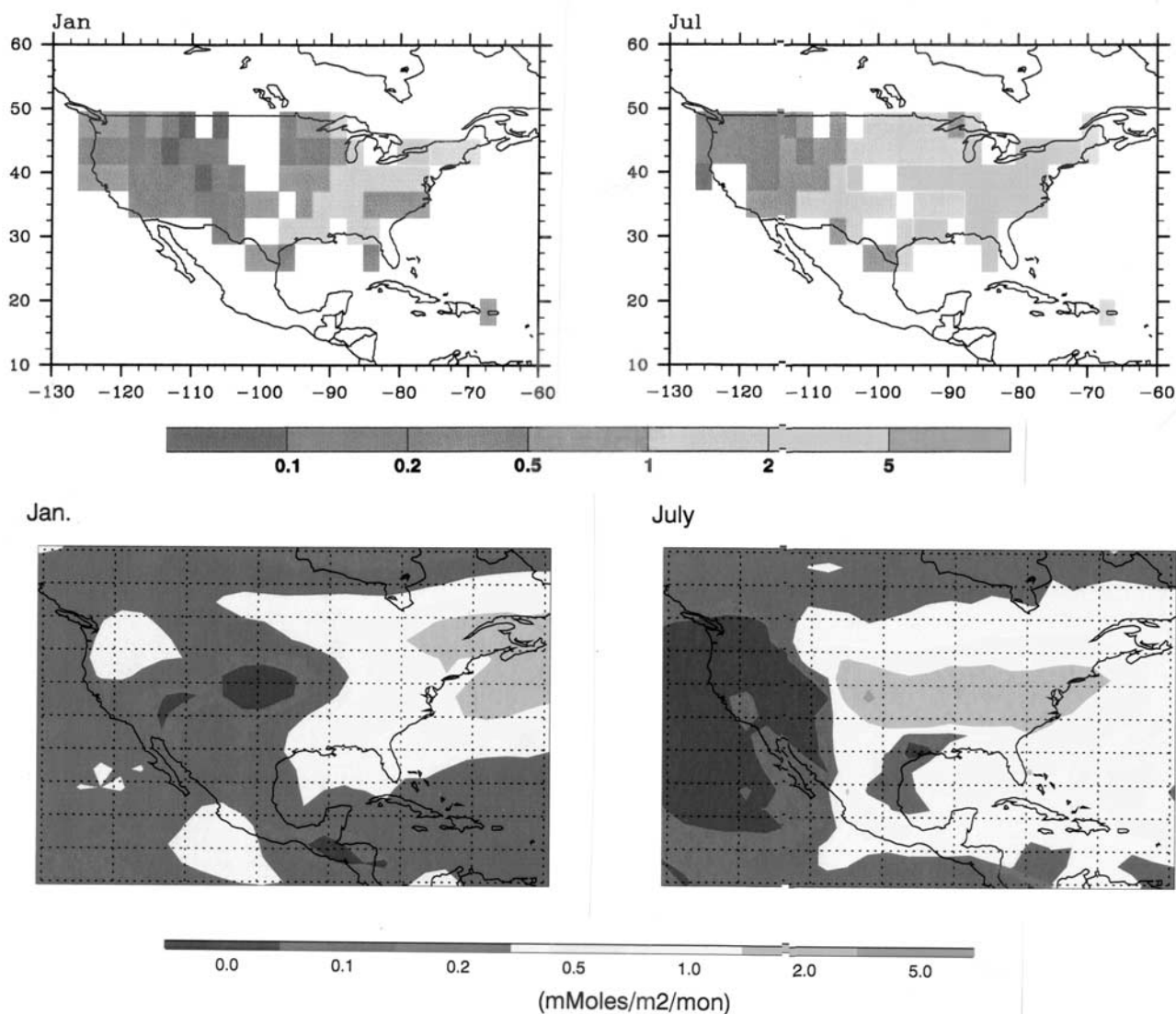


Figure 5. Calculated and observed (NADP) ammonium (NH_4^+) and nitrate (NO_3^-) deposition ($\text{mmol/m}^2/\text{month}$) in the United States in January and July. See color version of this figure at back of this issue.

[Hagen *et al.*, 1992; Parungo *et al.*, 1994; Liousse *et al.*, 1993]. The time constant to convert hydrophobic BC to hydrophilic BC is assumed to be 1 day, based on the work by Cooke and Wilson [1996]. Both hydrophobic and hydrophilic particles are transported in the same fashion by convection, advection, and diffusion, but hydrophobic BC is not subject to wet scavenging. It is, however, subject to dry deposition with a deposition velocity of 0.1 cm/s [Cooke and Wilson, 1996]. In contrast to hydrophobic BC, hydrophilic BC is subject to both wet and dry deposition, but is not directly emitted at the surface. Its removal rate by wet scavenging is assumed to be the same as for sulfate particles.

[28] BC particle concentrations are strongly affected by surface emissions, including biomass burning, which undergo seasonal variability. For example, during the dry season in the Amazon, biomass-burning events are much

more frequent than during the wet season. Figure 6 shows that the BC global distribution is characterized by substantial spatial and temporal variations in March, June, September, and December. The column mass of BC is highest in Europe, eastern Asia, Amazon, and Africa. Because the emission of BC is provided by both fossil fuel (6.7 TgC/year) and biomass burning (5.7 TgC/year), the high concentrations of BC in different regions can be related to these two types of emissions. For example, the high BC column mass in Europe and in eastern Asia is associated with fossil fuel emissions. These high column mass densities are subject to relatively small seasonal variability, as fossil fuel emissions of BC take place all year around. However, in the Amazon and in Africa, the high column mass changes considerably with season because it is dominated by the biomass burning emissions, which undergo a strong dry/wet season variation. In the Amazon, the maximum of column mass of BC is about

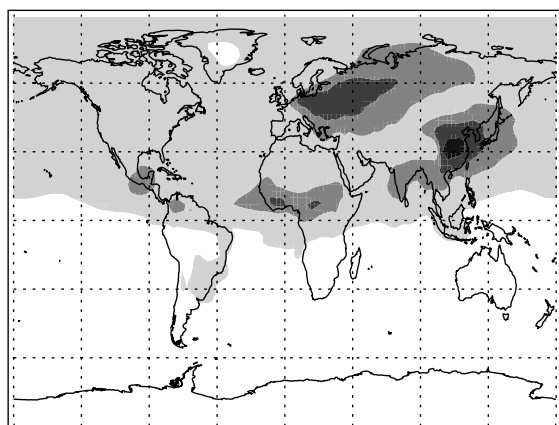
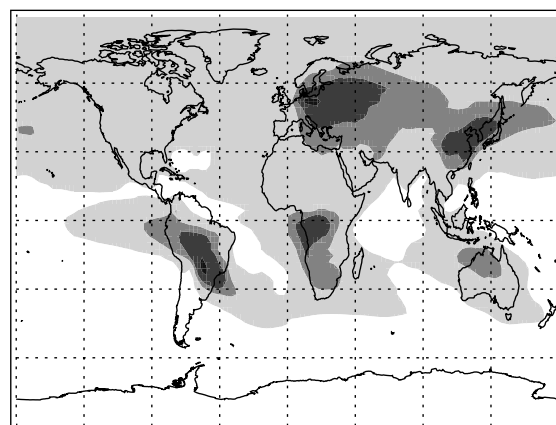
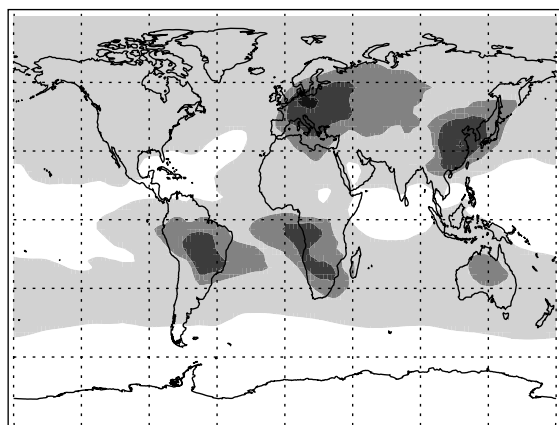
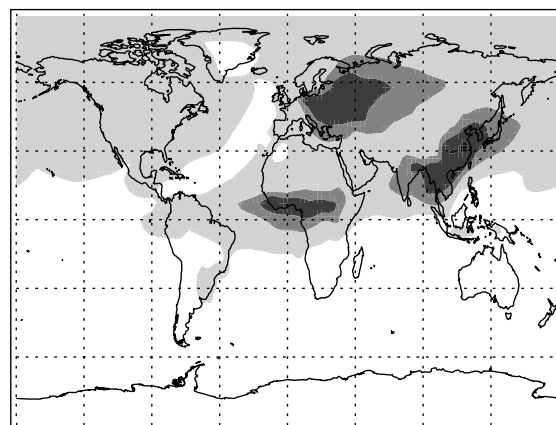
CBS Column (mg/m²) (March)CBS Column (mg/m²) (June)CBS Column (mg/m²) (Sept.)CBS Column (mg/m²) (Dec.)

Figure 6. Calculated black carbon (named CBS in the figure) tropospheric column loadings (mg/m²) in March, June, September, and December.

6 mg/m² in June, and is reduced to 0.1 mg/m² in December. In central Africa, the maximum column mass is about 2 to 6 mg/m² in December and March, and is displaced southward in June and September.

3.3.2. Organic Carbon (OC) and Secondary Organic Aerosol (SOA)

[29] Organic carbon aerosol (OC) includes primary organic carbon and secondary organic aerosol (SOA). As in the case of black carbon, primary organic carbon is directly emitted at the surface. The major emission of primary OC is provided by biomass burning and fossil fuel combustion. However, the ratio between the biomass burning to fossil fuel emission in the case of OC (1.6) is higher than the case of BC (0.8), indicating that biomass burning plays a more important role in controlling the OC budget [Liousse *et al.*,

1996]. The total primary OC emission adopted in this study is 62 Tg/yr on the basis of IPCC [2001] estimates for year 2000.

[30] Unlike primary OC, secondary organic carbon (SOA) is not directly emitted from the surface emission, but is formed through oxidation of atmospheric volatile organic compounds (VOCs). The chemical scheme of MOZART-2 includes about 50 organic species. According to the experiments performed by Seinfeld and Pandis [1998], only certain VOCs and their products produce SOA. In MOZART-2, we assume that formation of SOA results from α -pinene (C₁₀H₁₆) and “*n*-butane” (in MOZART-2, “*n*-butane” represents as a surrogate for all hydrocarbons with 4 or more carbons, excluding isoprene and terpenes) oxidation. The surface emission of α -pinene

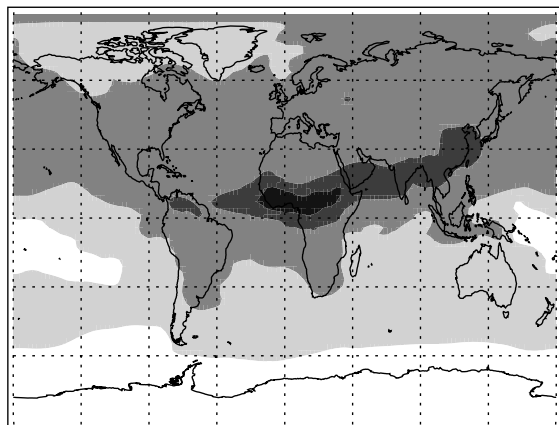
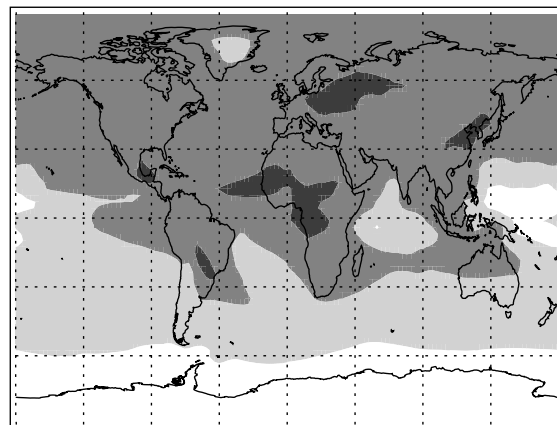
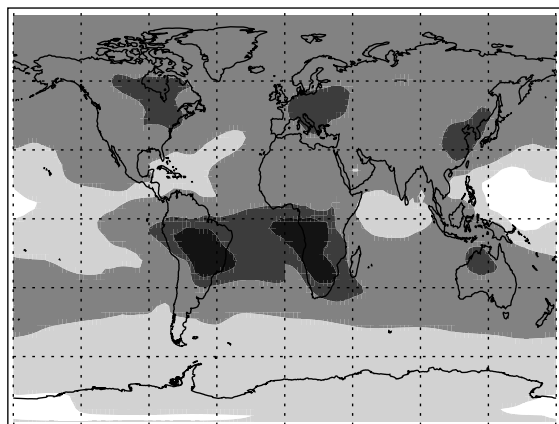
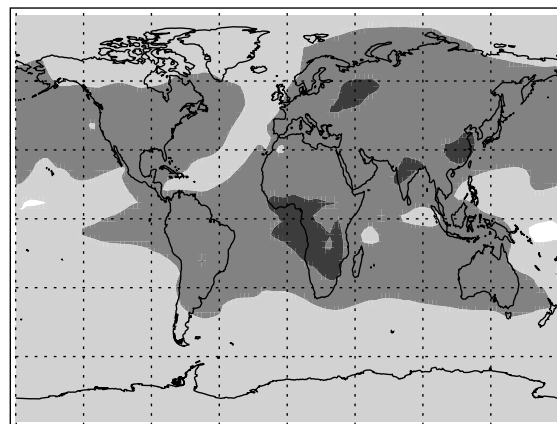
OCS Column (mg/m²) (March)OCS Column (mg/m²) (Jun.)OCS Column (mg/m²) (Sept.)OCS Column (mg/m²) (Dec.)

Figure 7. Same as Figure 6 but for primary organic carbon aerosol.

results mainly from biogenic activity (129 Tg-C/yr), and the emissions of *n*-butane considered in MOZART-2 include industrial, biomass and ocean sources (29 Tg-C/yr). α -pinene and “*n*-butane” react with OH, O₃, and NO₃ to produce carbonyl products and other oxygenated species that lead to the formation of SOA. The method of estimating the SOA mass is through an estimate of the bulk aerosol yields from the parent VOC. Rates of aerosol formation yields have been derived from smog chamber experiments and represent the maximum amount of SOA that can be produced from a unit of reacting VOC. According to *Seinfeld and Pandis* [1998], the bulk SOA yield coefficients are 762 $\mu\text{g}/\text{m}^3/\text{ppm}$ for α -pinene and 78 $\mu\text{g}/\text{m}^3/\text{ppm}$ for “*n*-butane” (the method to get yield coefficients of “*n*-butane” is described by *Lack et al.* [2004]). Because α -pinene has a

much higher bulk yield coefficient and a higher emission than *n*-butane, SOA is mainly formed by the oxidation of α -pinene [*Lack et al.*, 2004] and is expressed in MOZART-2 as

$$\frac{d[\text{SOA}]}{dt} = B_f \{ (k_1 \cdot [\text{C}_{10}\text{H}_{16}] \cdot [\text{OH}]) + (k_2 \cdot [\text{C}_{10}\text{H}_{16}] \cdot [\text{O}_3]) + (k_3 \cdot [\text{C}_{10}\text{H}_{16}] \cdot [\text{NO}_3]) \}$$

where B_f is the bulk yield coefficient for α -pinene, k_1 is the reaction rate coefficient for $\text{C}_{10}\text{H}_{16} + \text{OH}$, k_2 is the reaction coefficient for $\text{C}_{10}\text{H}_{16} + \text{O}_3$, and k_3 is the reaction coefficient for $\text{C}_{10}\text{H}_{16} + \text{NO}_3$. A detailed description of the SOA formation is given by *Lack et al.* [2004].

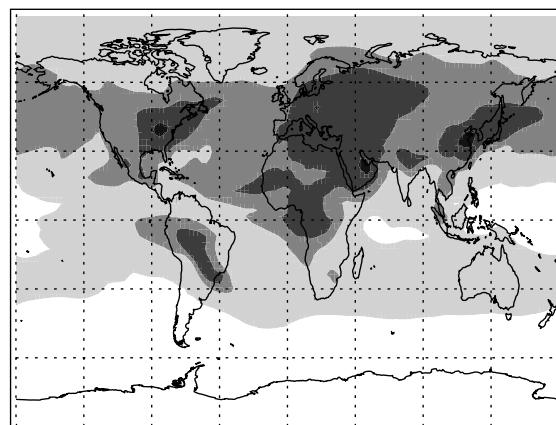
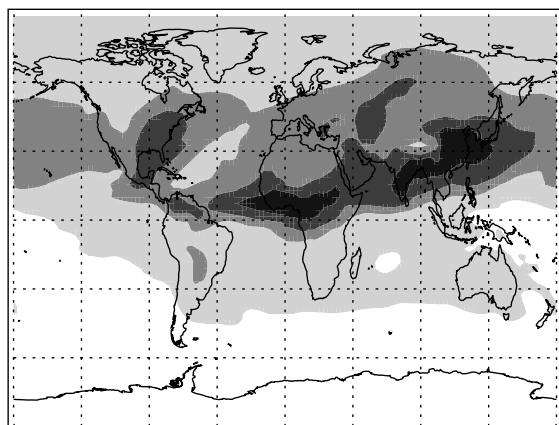
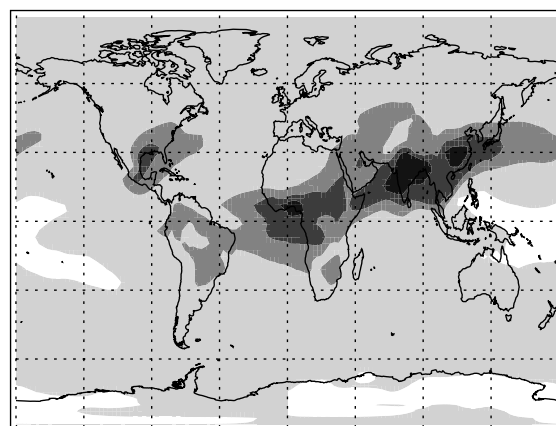
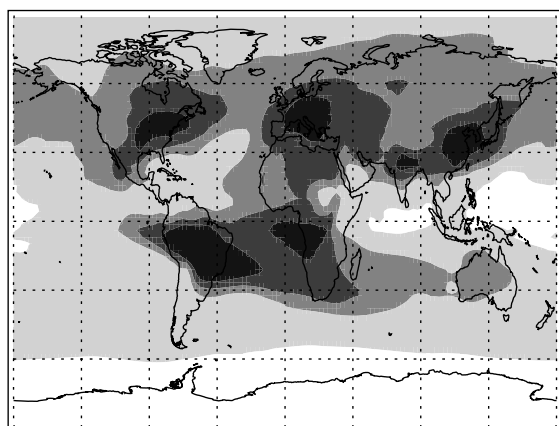
SOA Column (mg/m²) (March)SOA Column (mg/m²) (Jun.)SOA Column (mg/m²) (Sept.)SOA Column (mg/m²) (Dec.)

Figure 8. Same as Figure 6 but for secondary organic carbon aerosol.

[31] As in the case of black carbon, OC is also distributed between hydrophobic and hydrophilic particles. In MOZART-2, the hydrophobic OC is not subject to wet scavenging, but hydrophilic OC is subject to both wet and dry deposition. The rate of deposition of OC is assumed to be the same as the rate for black carbon.

[32] Figure 7 shows the calculated global distribution of primary OC. In general, the column mass of primary OC is higher than that of BC. The highest concentrations of primary OC are found in the eastern United States, Europe, eastern Asia, India, Amazon, and central Africa. These maximum concentrations result primarily from the high surface emissions in these regions (fossil fuel emissions in the eastern United States, Europe, and eastern Asia, but biomass burning in the Amazon and in Africa). Because of high seasonal variability of biomass burning (dry and wet seasons), the column mass of primary OC in the Amazon is highest in September with

a maximum value of 15 mg/m², and lowest in March (about 2 to 3 mg/m²). In central Africa, the maximum column mass is highest in March, and is displaced southward in September.

[33] Figure 8 shows the calculated global distribution of secondary OC (SOA). In general, the column mass of SOA is 5–10 times smaller than that of the primary OC. Since SOA is produced from α -pinene, the highest concentrations of SOA are found in the Amazon, in Africa, southeastern Asia, eastern United States, and Europe. The seasonal variability of SOA is also different than that of primary OC, because SOA formation is driven by the rate of oxidation of α -pinene by oxidants, such as OH and O₃, which are more abundant in summer than in winter. As a result, the mass density of SOA is highest in summer and rapidly decreases in winter. For example, in Europe the column mass of SOA is much smaller in December than in June.

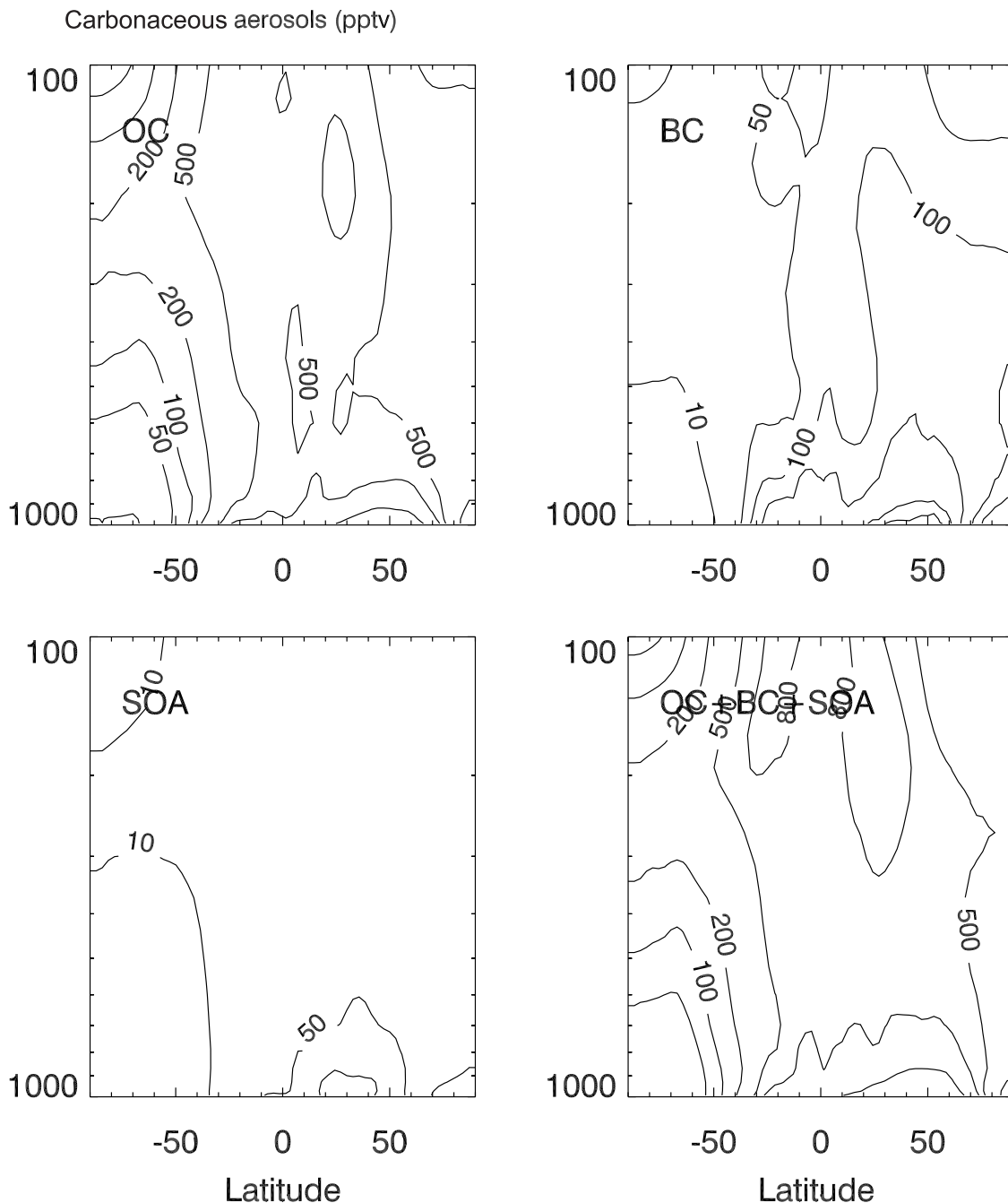


Figure 9. Calculated annual mean of the zonally averaged volume mixing ratio of primary organic carbon, black carbon, secondary organic carbon, and total carbon aerosol concentrations (pptv).

[34] Figure 9 shows the zonally averaged concentration of BC, primary OC, SOA, and of total carbonaceous aerosols (annual average values). Because the concentration of BC is strongly influenced by fossil fuel emissions that occur mostly in the Northern Hemisphere, the maximum concentration of BC is located at midlatitudes in the Northern Hemisphere. There is evidence that convection transports BC into the upper troposphere in the Northern Hemisphere. The concentrations of primary OC are significantly affected by biomass burning, leading to high OC concentrations in the tropics, where convective transport is stronger than at midlatitudes. As a result, large amounts of primary OC are

transported from the boundary layer into the upper troposphere in the tropics. SOA concentration is also high in the tropics because of the relatively high α -pinene emissions.

[35] The concentrations of SOA are considerably smaller than the concentrations of primary OC, especially in the lower troposphere. As a result, SOA do not affect substantially the photolysis rates compared to the effects of primary OC. However, SOA formation leads to the reduction in the oxidation products of VOCs. Because some of these products are important for ozone production, SOA formation has the potential to modify the ozone concentration. Figure 10 shows the changes in surface CH_2O and O_3 (percent) due to

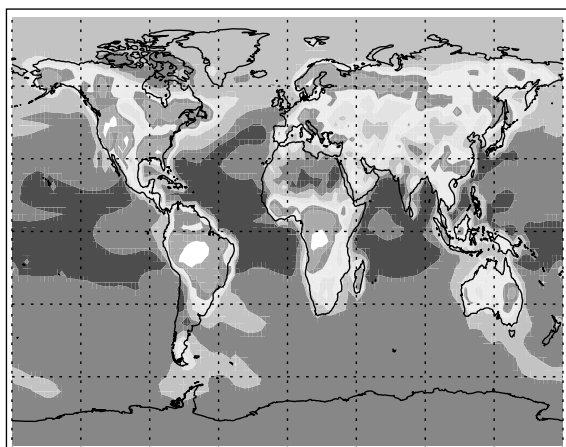
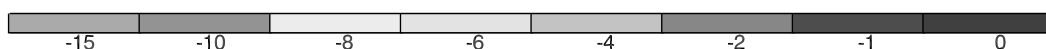
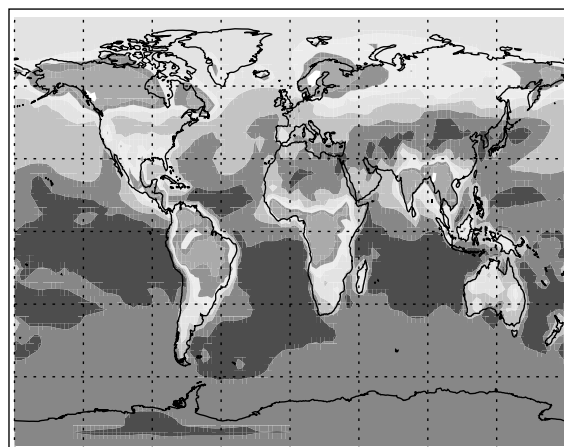
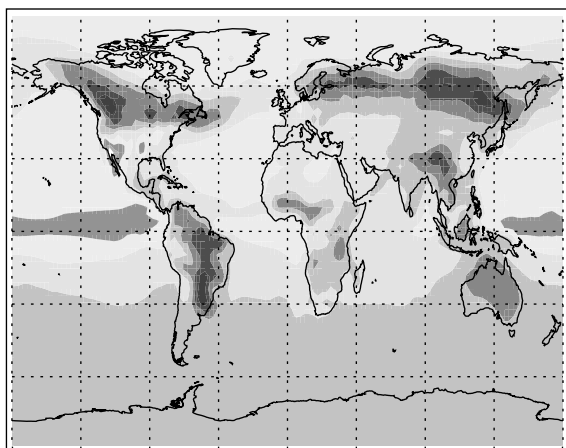
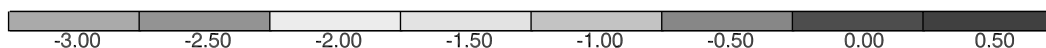
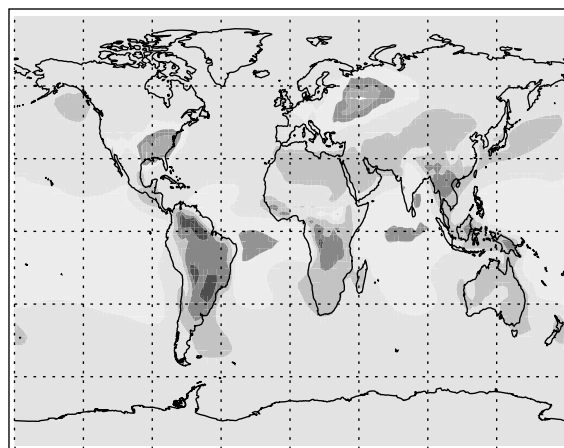
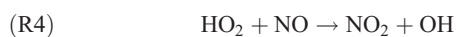
Changes in CH₂O(%) (June)Changes in CH₂O(%) (Dec.)Changes in O₃(%) (June)Changes in O₃(%) (Dec.)

Figure 10. Calculated changes in the surface concentration of CH₂O and O₃ (%) due to the formation of SOA in June and December. See color version of this figure at back of this issue.

the formation of SOA. The maximum reduction of O₃ (~3%) occurs in the eastern United States and in the regions of the tropical ocean. However, in the Amazon, where the concentrations of SOA are the highest, the impact on O₃ concentrations is smallest (nearly unchanged). The main effect of the SOA is to reduce concentrations of precursors of peroxy radicals (HO₂ and organic analogues), as shown in Figure 10 (upper panels) for formaldehyde whose photolysis is an important source of HO₂. The effect of this peroxy radical reduction on O₃ is dependent on the NO_x levels: At high NO_x levels, peroxy radicals lead to O₃ production via their rate-limiting reactions with NO, e.g.,



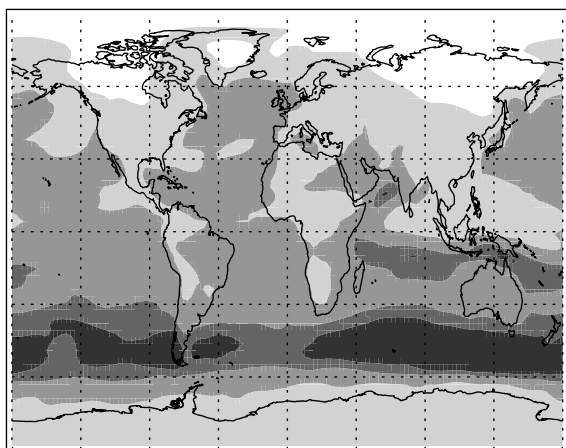
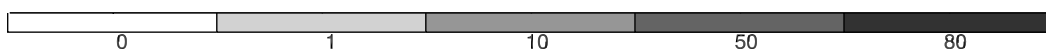
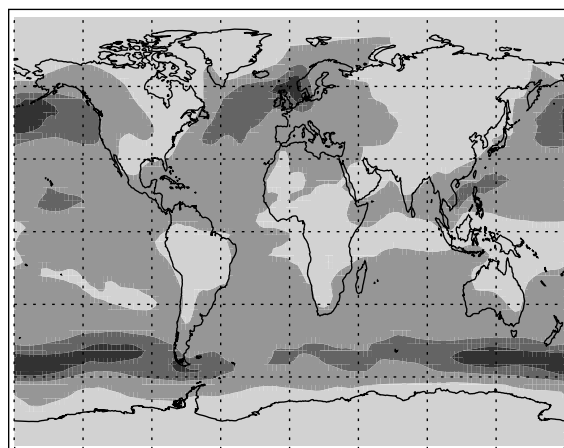
so that a lowering of peroxy radical levels will result in less O₃ production, as noted over the United States. Where NO concentrations are low (e.g., about 40 pptv in the Amazon), any changes in the production of O₃ by (R4) are partly offset by the reaction



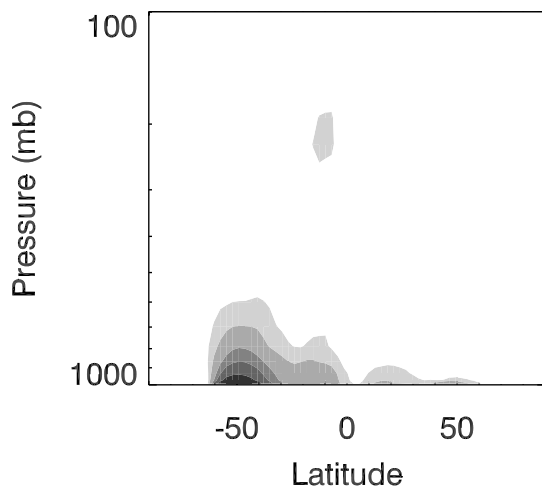
so that the net effect on O₃ concentrations is negligible.

3.4. Sea Salt

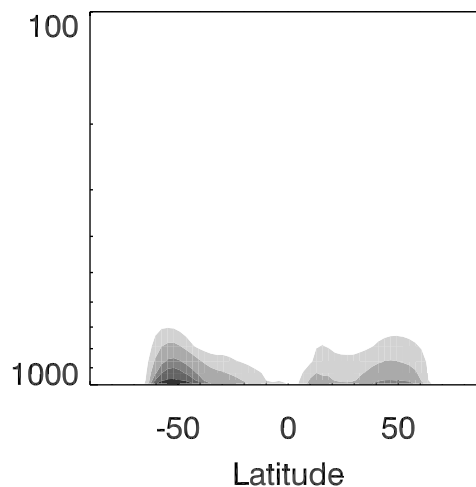
[36] The distribution of sea-salt aerosol is calculated using the scheme developed by *Chin et al.* [2000]. The concentrations of sea salt are controlled by emissions,

SALT Column (mg/m²) (June)SALT Column (mg/m²) (Dec.)

Zonal SALT (ppbv) (June)



Zonal SALT (ppbv) (Dec)

**Figure 11.** Same as Figure 2 except for sea-salt aerosol.

transport, dry and wet deposition, and gravitational settling. Sea-salt emissions are strongly dependent on wind speed near the surface, and the relationship between the surface flux F (particles/m²/s) and the particle radius r (μm) can be derived from the empirical relationship given by *Gong et al.* [1997]:

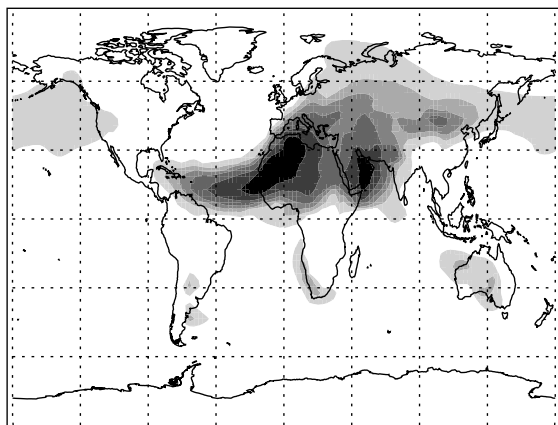
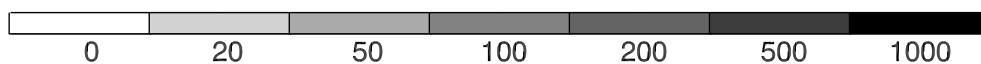
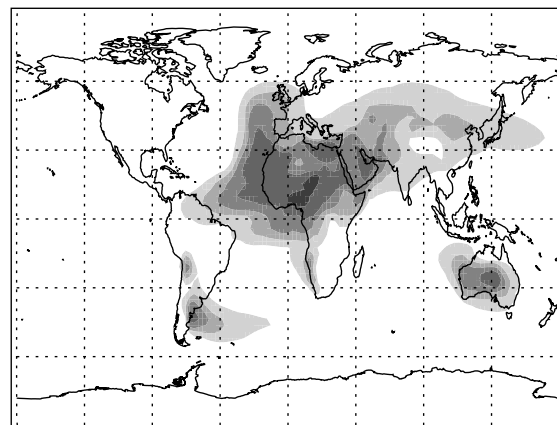
$$dF/dr = 1.37 U_{10}^{3.41} r^{-3} (1 + 0.057 r^{1.05}) 10^B \quad (1)$$

where U_{10} (m/s) is the wind speed at 10 m above the surface, and $B = \{1.19 \exp [-(0.380 - \log r)/0.65]\}^2$. The gravitational settling velocity V (m/s) varies with the size of the particles, and is calculated as follows:

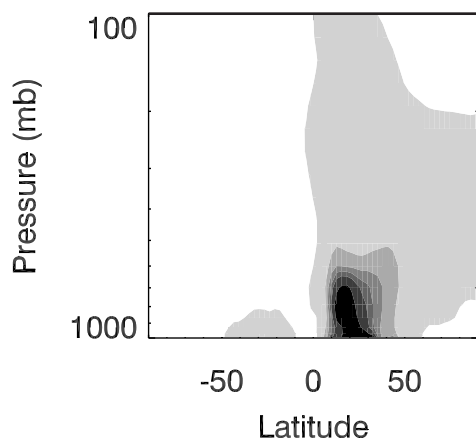
$$V = 2 g \rho_d (r_m)^2 / (0.5 d_v) \quad (2)$$

where $g = 9.81$ (m/s²) is the gravitational acceleration, ρ_d (2200 kg/m³) is the density of sea-salt particles, r_m is the medium radius (m), and d_v (1.5×10^{-5} kg/m²/s) is the coefficient of dynamical viscosity. Because the emission flux and gravitational settling are strongly dependent on the size of the particles, we adopt a size distribution that is represented by four bins (median radius of 0.26, 1.2, 2.4, and 7.6 μm , respectively). Sea-salt aerosols are subject to rapid growth as the ambient relative humidity (RH) increases. For example, if the RH is 80%, the particle size is twice the size of the dry particles. Advective transport and wet deposition are assumed to occur independently of the size of the particles.

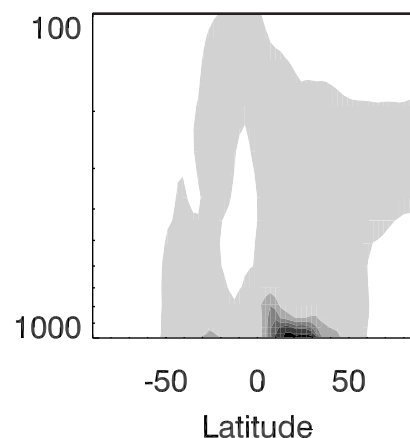
[37] Figure 11 (upper panels) represents the global distributions of the calculated column mass for sea-salt aerosols. It shows that the concentrations are highest between

DUST Column (mg/m²) (June)DUST Column (mg/m²) (Dec.)

Zonal DUST (ppbv) (June)



Zonal DUST (ppbv) (Dec)

**Figure 12.** Same as Figure 2 except for mineral dust aerosol.

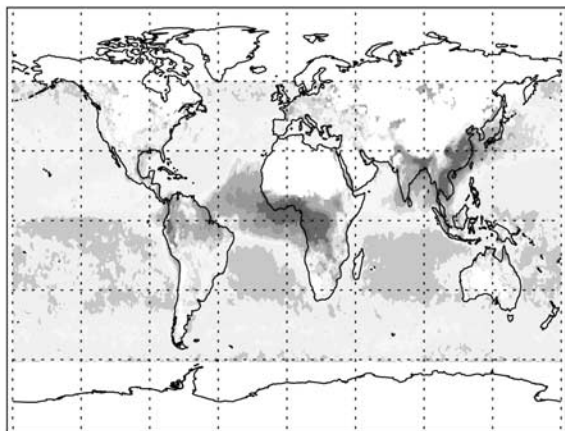
40° and 60° in both hemispheres because of the strong winds blowing over the oceans. The maximum column mass in these regions is 40 to 80 mg/m². The seasonal variability is also evident. The column mass is highest during December in the Northern Hemisphere, and during June in the Southern Hemisphere. Figure 11 (lower panels) shows that the sea-salt concentrations are contained in the marine boundary layer. For example, the concentrations reaches 30 ppbv below 900 mbar, and 10 ppbv are below 800 mbar. The major processes in controlling sea-salt concentrations are the surface emissions and gravitational settling, especially in the case of large sea-salt particles. For example, for the smallest sea-salt particles (radius = 0.26 μm) the settling velocity is about 33 m/day, while for the larger sea-salt particles (radius = 7.6 μm) it is about 28 km/day. The fast gravitational settling removes sea salt quickly from the atmosphere. Therefore the larger sea-salt particles remain

primarily in the marine boundary layer. As a result of high concentration of sea salt over the oceans, several studies suggested that sea-salt aerosols could affect oxidants in the marine boundary layer, especially due to the halogen chemistry [Sander *et al.*, 1999; McFiggans *et al.*, 2002]. The corresponding processes are not yet included in MOZART-2.

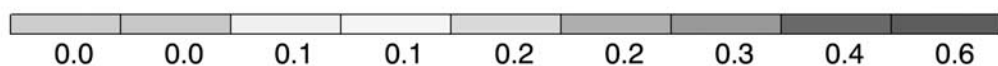
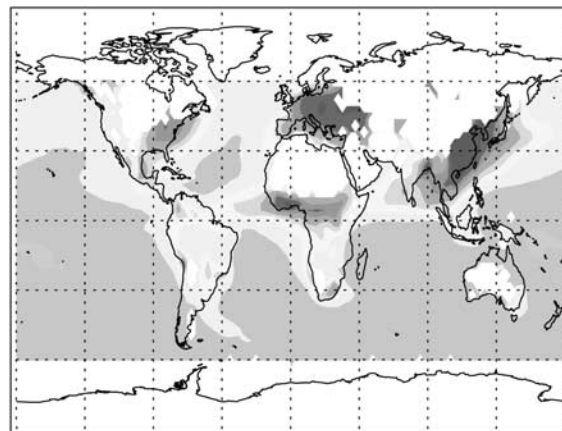
3.5. Dust

[38] Unlike other aerosols, the dust module is currently decoupled from MOZART-2. The dust distributions are calculated in MATCH using the same transport parameterizations [Rasch *et al.*, 1997], but different advection scheme and wet deposition scheme. Dust mobilization and dry deposition are calculated using the Dust Entrainment and Deposition module [Zender *et al.*, 2003], which is based on wind tunnel studies in dust source regions. The source at

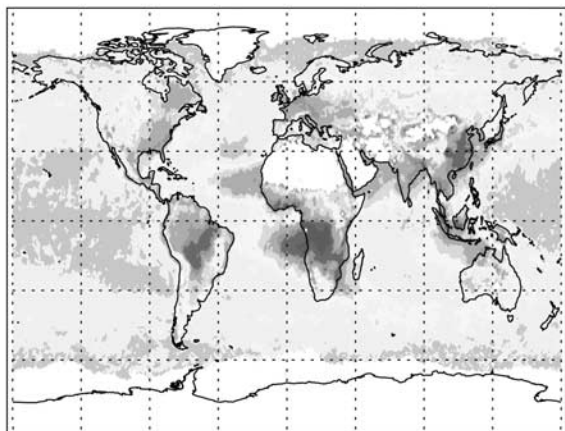
MODIS Fine Mode (Feb)



MOZART-2 Fine Mode (Feb)



MODIS Fine Mode (Sept)



MOZART-2 Fine Mode (Sept)

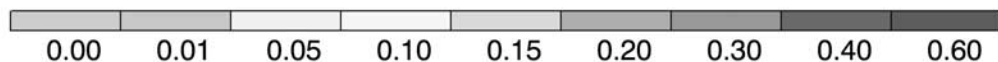
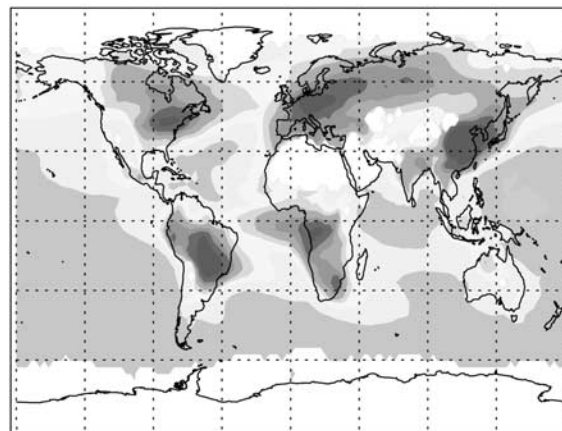


Figure 13. Calculated (right column) and observed (MODIS) (left column) optical depth at 550 nm for fine mode aerosol (including sulfate, black carbon, organic carbon, and ammonium nitrate). See color version of this figure at back of this issue.

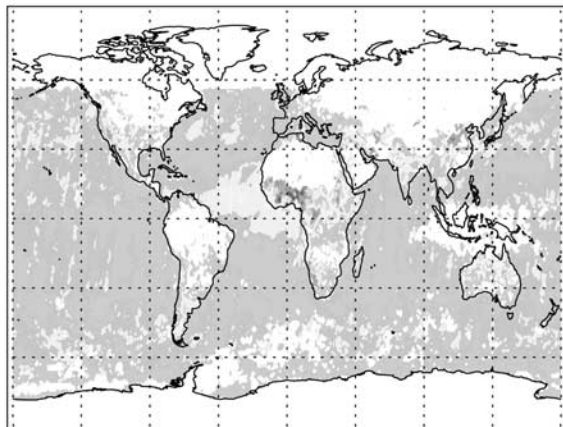
every grid point is derived from the monthly mean dust entrainment calculated in a 1979–2000 simulation using the NCEP reanalysis [Luo *et al.*, 2003]. However the dust entrainment into the atmosphere is allowed to occur on specific days, and is assumed to be proportional to the third power of the surface winds. This methodology ensures that the monthly mean source used in the model is consistent with observations, even though general circulation models have difficulty capturing the spatial and temporal variability of the sources [e.g., Tegen and Miller, 1998], and simulating the event-based nature of desert dust transport. The source areas are identified by Ginoux *et al.* [2001] to be dry, unvegetated regions that have relatively low topography. Four size bins (with mean radius of 0.75, 1.25, 2.50, 4.50 μm) are included in the model to better simulate the size-dependent dry deposition processes.

[39] Figure 12 (upper panels) shows that the dust column mass is very high in the northern low latitudes. The high

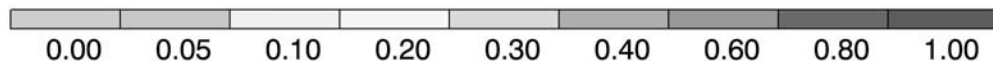
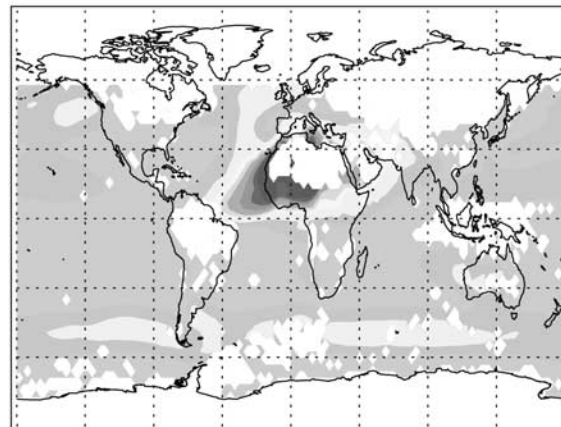
column mass in this region is attributed primarily to the emission from the Sahara desert. The dust mass is also high in the vicinity of mideastern Asia, northern India, and Mongolia. The maximum column mass exceeds 500 mg/m^2 . Long-range transport of dust is evident, and it is illustrated by the transport to the Atlantic and Pacific oceans. There is also considerable seasonal variability in the abundance of dust aerosol. In June more dust is transported into the Atlantic than in December. Compared to other aerosols, dust has a high mass loading. It is interesting to note that dust is present in largest abundance at low latitudes, while sea-salt aerosols are most abundant at high latitudes. As photochemical processes are most active in the tropics, dust aerosols could play important roles in controlling tropospheric oxidants through both heterogeneous chemical processes and photolysis.

[40] Figure 12 (lower panels) shows the zonally averaged dust concentrations in June and December, respectively. The

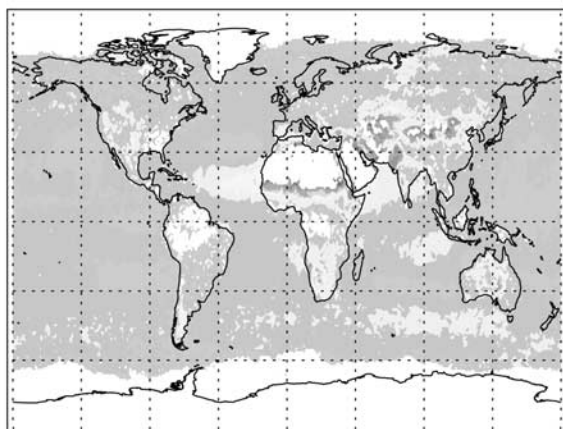
MODIS Coarse Mode (Feb)



MOZART-2 Coarse Mode (Feb)



MODIS Coarse Mode (Sept)



MOZART-2 Coarse Mode (Sept)

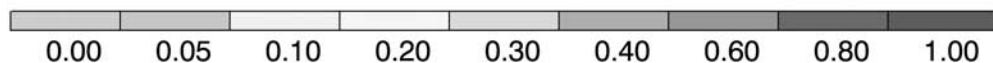
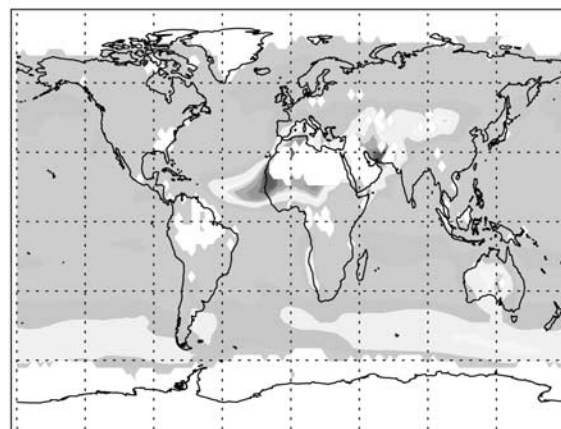


Figure 14. Calculated (right column) and observed (MODIS) (left column) total vertical optical depth at 550 nm for coarse mode aerosols (including mineral dust and sea salt). See color version of this figure at back of this issue.

dust concentrations are high between 10° and 40°N . The concentrations are highest in the boundary layer (above 60 ppbv) and rapidly decrease with altitude. However, unlike sea-salt aerosol, there is evidence that dust is transported into the upper troposphere by convective process, especially in summer when convection is strongest. The dust in the upper troposphere consists mostly of small size particles since these particles remain suspended much longer (10 days) than the large size particles (1 day) in the atmosphere.

4. Comparison With Observations

[41] Satellite measurements offer the best opportunity for making global measurements of tropospheric aerosol and trace gases over extended periods of time. The Moderate-Resolution Imaging Spectroradiometer (MODIS) instru-

ment provides a global view of aerosol distributions. The MODIS aerosol data are provided at a spatial resolution (pixel size) of 10×10 km at nadir. Using multichannel information and preassumptions on the general structure of the aerosol type and size distribution, it is possible to estimate the fraction of the optical depth due to fine aerosols (accumulation mode particles with a radius smaller than $0.5 \mu\text{m}$), and due to coarse aerosols (particles with radius larger than about $0.5 \mu\text{m}$) [Kaufman *et al.*, 1997; Tanre *et al.*, 1997; Chu *et al.*, 2003]. The product provided by MODIS offers a good opportunity to evaluate our model aerosol burdens and, to some extent, their speciation.

[42] In order to compare the model results with the values measured from space, the atmospheric optical depth is derived from the mass of aerosols calculated by the model. The relationship between the aerosol column mass density

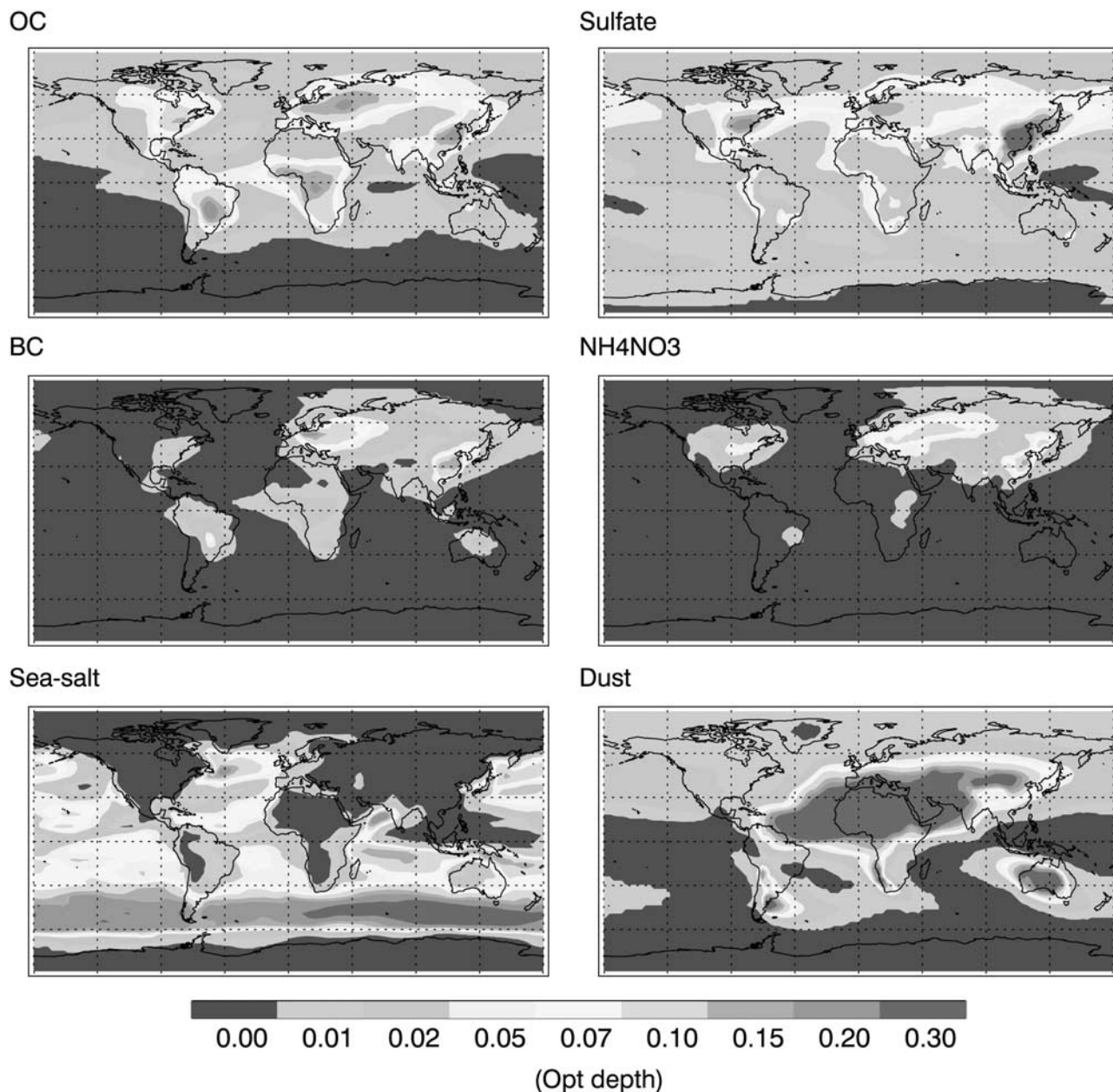


Figure 15. Calculated annual mean total vertical optical depth at 550 nm for sulfate, black carbon, organic carbon, ammonium nitrate, sea-salt, and mineral dust aerosols. See color version of this figure at back of this issue.

(M (g/cm^2)) and the optical depth (τ , dimensionless) at a wavelength (λ) of 550 nm is given by *Lacis and Mishchenko* [1995], and can be expressed as

$$\tau = 3 QM/(4\rho r_m) \quad (3)$$

where ρ is the aerosol density (g/cm^3), r_m is the mean radius of aerosol (cm), and Q is the extinction coefficient at $\lambda = 550$ nm, which is calculated from Mie-scattering theory and depends on the optical properties of the aerosols [*Hansen and Travis*, 1974]. Aerosols have different degrees of hygroscopic growth with atmospheric relative humidity (RH). The growth rates for different aerosol types are given by *Chin et al.* [2000]. In their study, sulfate, OC, and sea-

salt aerosols grow very rapidly with relative humidity. For example, at 80% humidity, the aerosols radius is a factor of 50% to 100% larger than their dry radius. Hydrophilic BC are assumed to be about 20% larger than hydrophobic BC. For dust, *Chin et al.* [2000] assume that particles do not change with relative humidity, since dust aerosols contain little hygroscopic material [*Li-Jones et al.*, 1998].

[43] With these assumptions, we define the aerosol mass M as the sum of dry aerosol mass M_d and water mass M_w and express the optical depth τ as

$$\tau = f_d(3Q_dM_d/(4\rho_d r_e)) + (1 - f_d)(3Q_wM_w/(4\rho_w r_e)) \quad (4)$$

where f_d is the weight fraction of dry aerosol, r_e is the aerosol radius after the hygroscopic growth, ρ_d and ρ_w

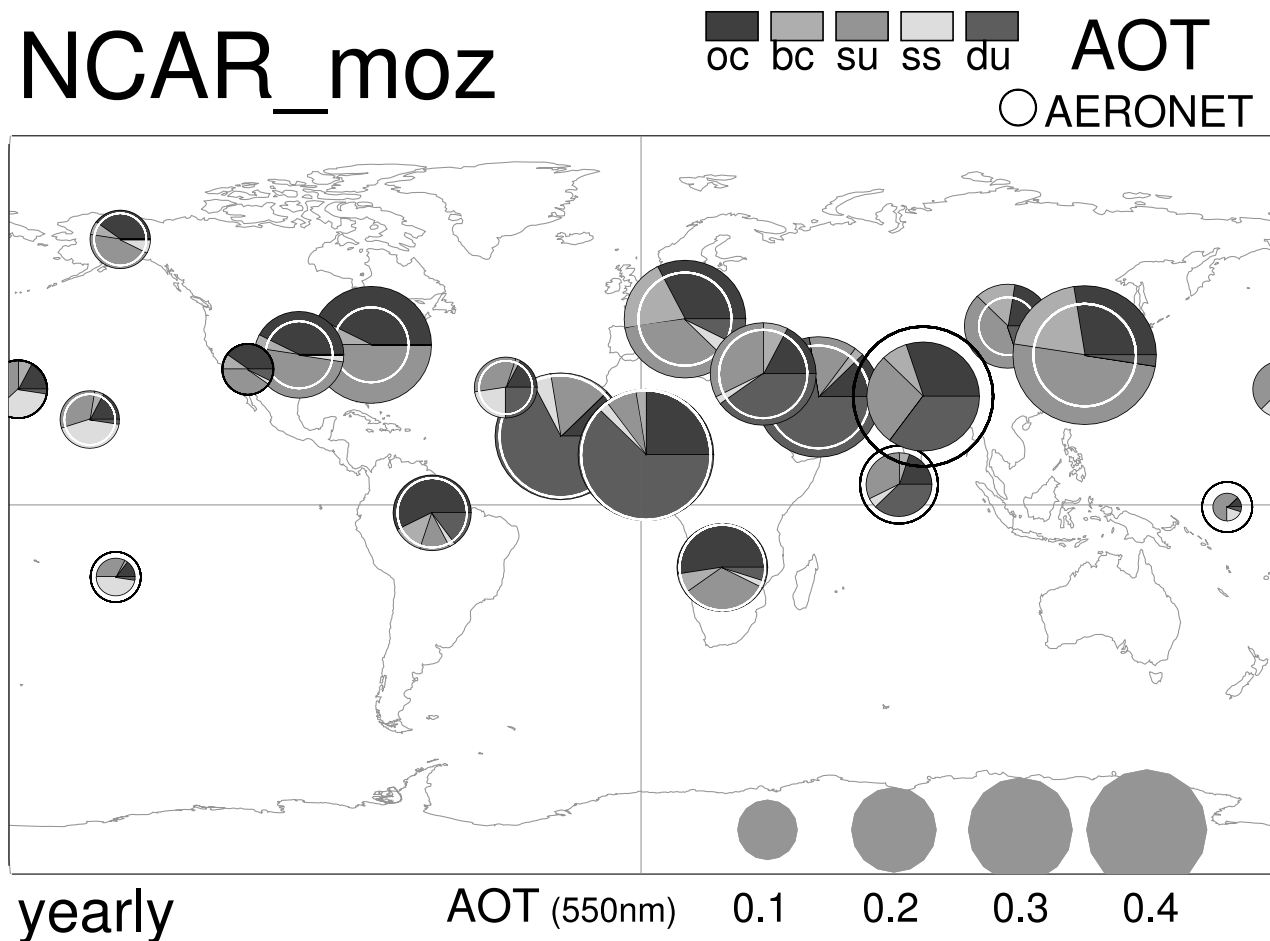


Figure 16a. Comparison between calculated and measured aerosol optical depth (AOT) at different AERONET sites. The colors represent the calculated contribution of different types of aerosols to the AOT (blue for organic carbon, light blue for black carbon, green for sulfate, yellow for sea salt, and red for dust). The circles represent the AERONET measurement for the total AOT. See color version of this figure at back of this issue.

are the densities of dry aerosol and water, M_d and M_w are the masses of dry aerosol and water, and Q_d and Q_w are the extinction coefficients for dry aerosol and water, respectively.

[44] The calculated relative humidity (RH) in the lower troposphere (not shown) indicates that RH is highest (>80%) in polar regions, where the temperature is low. However, in these regions, the aerosol concentrations are normally low, so that hygroscopic growth of aerosol is not important. In contrast, in Europe aerosols (such as sulfate and OC) have high concentrations and the RH values can reach 70%. In this case, the hygroscopic growth of aerosol is significant in determining the aerosol surface area and the optical depth. The RH values are also high in India, southeast China, Amazonia, and south Africa, where aerosol concentrations are usually high. Unlike in Europe, where the RH is constantly high, strong seasonal variations in the RH appear in the Amazon. In this region the RH is about 70% in wet season, and is reduced to 40% in dry season. In general, the calculated hygroscopic growth produces higher optical depth than its dry aerosol mass (not shown).

[45] Figure 13 (left columns) shows the Terra/MODIS global distributions of the fine mode aerosol optical depth

($\lambda = 550 \text{ nm}$) for February and September 2000. Several interesting features can be identified from this image, including the industrial and urban pollution over North America and Europe, the outflow from Asia over the Pacific Ocean, and the strong plumes due to biomass burning in southern Africa and South America. In the model, we assume that fine particles are composed of sulfate, ammonium nitrate, black carbon, and organic carbon aerosols, and that their median radii are generally smaller than $0.5 \mu\text{m}$. The corresponding modeled optical depth is shown in the right panels of Figure 13. The comparison between the calculated and the measured fine mode aerosol optical depths (AOD) suggests several similarities and discrepancies. The measured AOD are characterized by maxima in southern Africa, Amazon, and eastern Asia, which are also shown by the model data. The maximum AOP in these regions are between 0.4 and 0.5, as shown by both calculation and measurement. The observed outflow of the aerosols from southern Africa into the Atlantic is also well reproduced by the model. Beside these similarities between MODIS and MOZART-2, some discrepancies, however, are also noted. For example, the calculated AOD is overestimated in Europe. In this region, the major contribution to

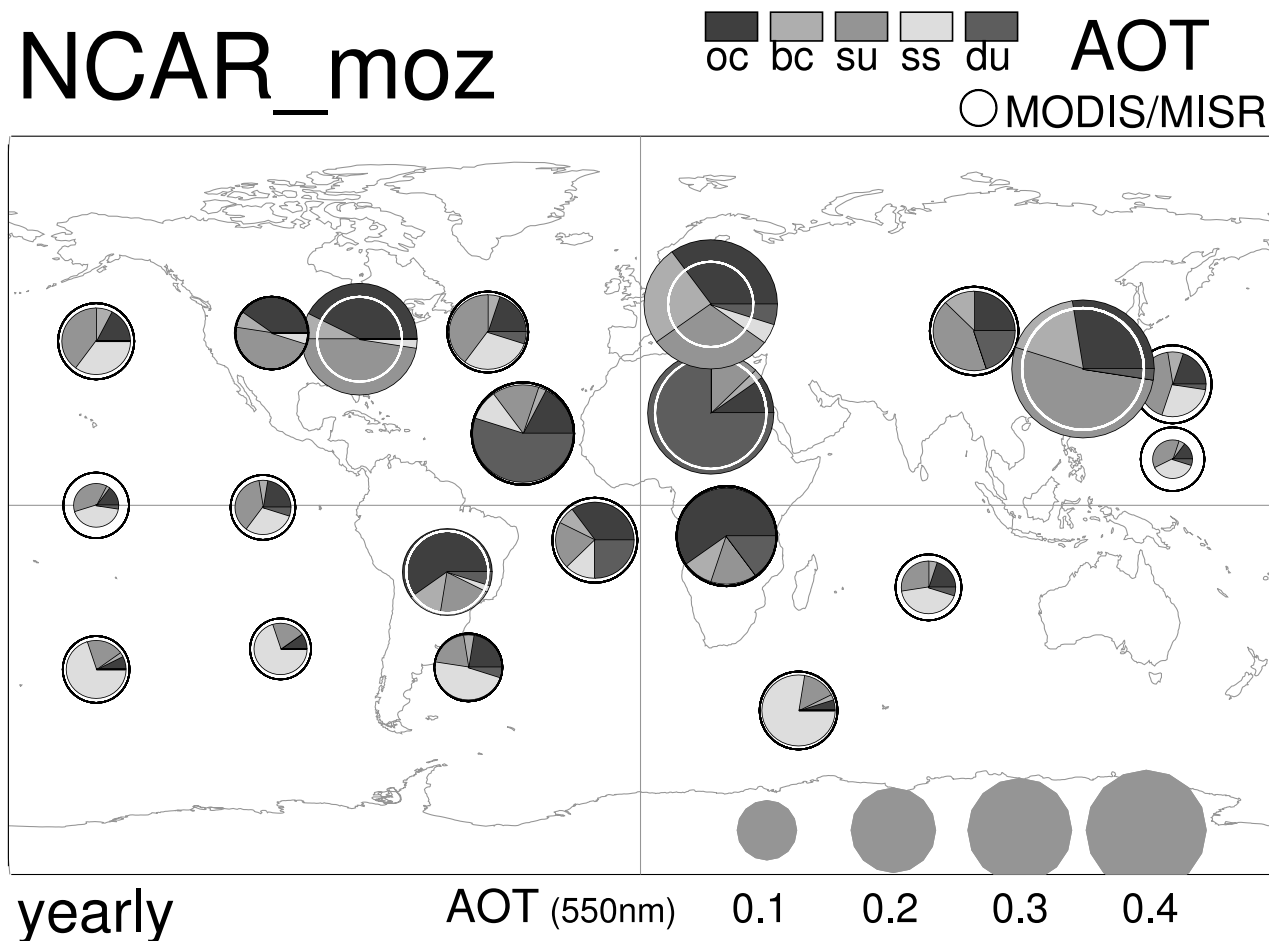


Figure 16b. Same to Figure 16a but for the MISR/MODIS satellite measurement in different regions of the world. See color version of this figure at back of this issue.

AOD is from OC and sulfate aerosols. One possible explanation is therefore that the anthropogenic emissions of OC and SO_2 used in the model are overestimated in Europe. Since retrievals of MODIS are not possible under cloudy conditions, it is also possible that the measured AOP is somewhat underestimated in this region.

[46] Figure 14 shows the measured distribution of coarse mode aerosols, which usually includes dust and sea-salt particles with radius sizes larger than $0.5 \mu\text{m}$. The measured and calculated geographical distributions of coarse aerosols are generally in agreement. Measurements as well as calculations show that the Sahara dust is subjected to long-range transport from the source region to the Atlantic Ocean. However, the calculated dust concentrations in the source region (Sahara desert) and in the dust plume are overestimated compared to the MODIS measurements, especially in February. The band of high sea-salt aerosol concentrations between 40°S and 60°S is also shown in both the measurements and the calculations. In September, the calculation seems, however, to slightly overestimate the sea-salt aerosol abundance in this region.

[47] In order to carefully study the discrepancies between the calculated and the measured aerosol optical depth, the individual optical depth for the various aerosol components are calculated for both the fine and the coarse modes. Figure 15 shows the optical depth at 550 nm for OC, sulfate,

BC, ammonium nitrate, sea salt, and dust. OC, sulfate, BC and ammonium nitrate are included only in the fine mode, while sea salt and dust are included in the coarse mode. The figure shows that in eastern Asia, sulfate is the dominant aerosol. In the United States, the sulfate aerosol has also the highest concentration, followed by OC, and ammonium nitrate, and BC. In Europe, the highest aerosol optical depths result from the presence of OC and sulfate, with a secondary contribution from ammonium nitrate and BC. In the Amazon and in Africa, OC in the fine mode contributes the most with a secondary contribution from BC. For coarse mode particles, sea-salt aerosol plays a major role between 40° and 60° latitudes over the oceans of both hemispheres. Dust contributes the most in the Sahara and in its surrounding regions.

[48] Observations provided by Aerosol Robotic Network (AERONET) can be used to further evaluate the MOZART-2 model. AERONET is an optical ground-based aerosol monitoring network and data archive supported by the NASA's Earth Observing System and expanded by a partnership with many non-NASA institutions. Data from this collaboration provides globally distributed near real time observations of aerosol spectral optical depths, aerosol size distributions, and precipitable water in diverse aerosol regimes. The AERONET website, <http://aeronet.gsfc.nasa.gov/>, provides access to the preliminary data, describes the

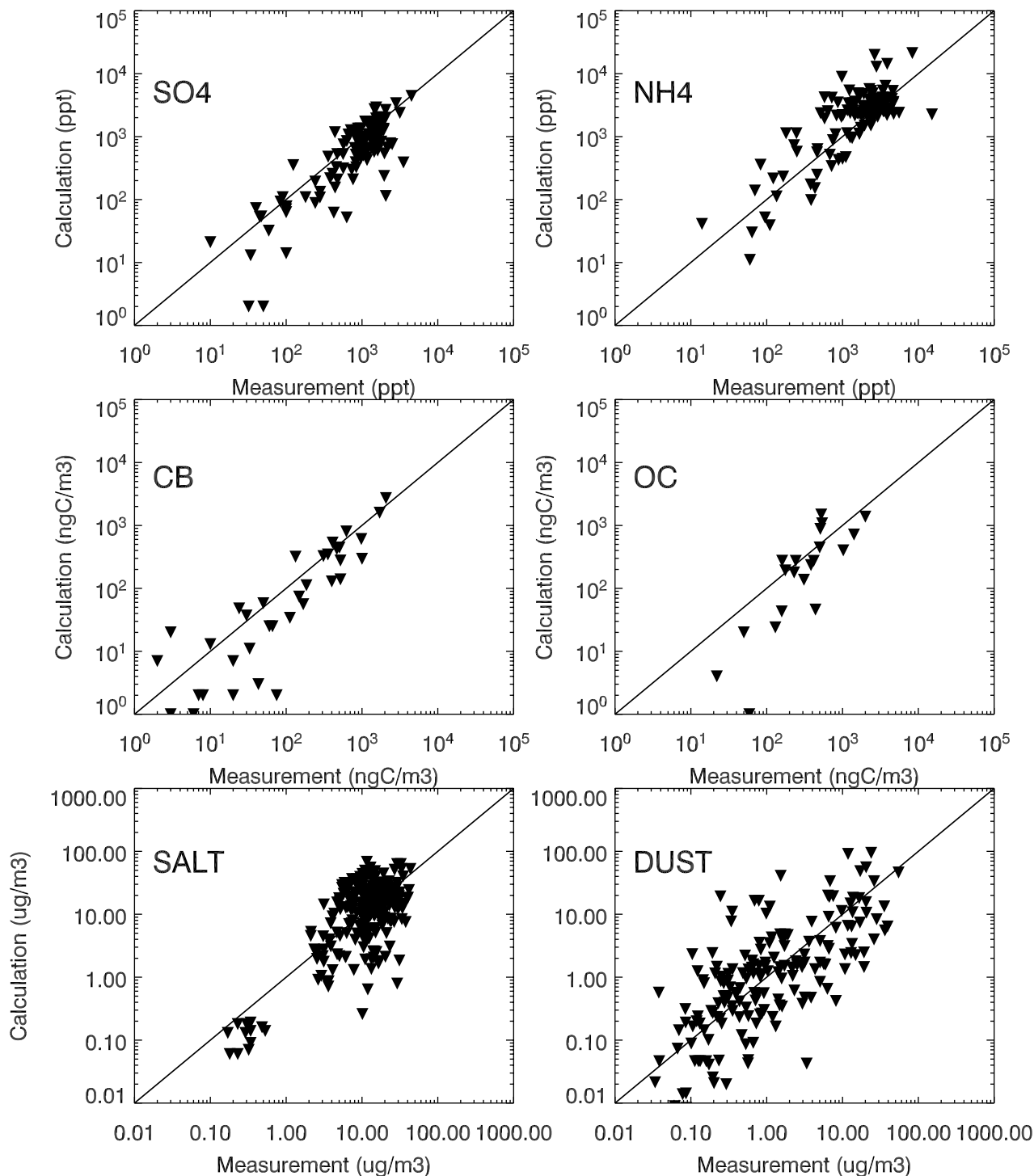


Figure 17. Comparison between calculated and surface measured aerosol concentrations for different type of aerosols. The x-axes represent the measurement value, and y-axes represent the calculated values. The solid line indicates the one-to-one correlation between calculations and measurements.

program objectives, affiliations, instruments, data products. Figure 16a shows the location of measured aerosol optical depths (at 550 nm) and provides a comparison with corresponding model results. Overall, the calculated values are in fair agreement with AERONET data. The comparison shows, however, that MOZART-2 overestimates the optical depth in eastern Asia by about 20%. In this region, aerosols

consist mainly of sulfate and carbonaceous particles. In India, the calculated aerosol optical depth is underestimated by about 20%, where dust aerosols provide a major contribution to particle composition. The calculated aerosol optical depth is also overestimated in the eastern United States by about 25%, but the difference is reduced to about 15% in the central United States, and the calculated values

are in good agreement with measurements in the western United States. In Europe, the calculated aerosol optical depth is 20% larger than the observed value with major contributions from sulfate and carbonaceous aerosols. In the important biomass burning regions (such as the Amazon and Africa), the calculated aerosol optical depth is in good agreement with measurements. In these regions, the carbonaceous aerosol provides the major contribution to aerosol optical depth. In and around the Sahara region, where mineral dust has a large contribution to aerosol composition, the calculated aerosol optical depth is also similar to the measured values. In remote regions, such as the Pacific and Atlantic oceans, the measured aerosol optical depth is well simulated by the model.

[49] Figure 16b compares the modeled aerosol optical depth with the combination of MISR (land) and MODIS (ocean) satellite data, which are currently probably the best data set from space. The MISR is the Multiangle Imaging Spectroradiometer instrument. MISR employs nine discrete cameras pointed at fixed angles, one viewing toward the nadir (vertically downward) direction, four viewing toward the forward directions and four viewing toward backward directions along the spacecraft flight. In addition to the nadir, the cameras image the Earth at 26.1, 45.6, 60.0, and 70.5 degrees forward and backward of the local vertical. In general, large viewing angles provide enhanced sensitivity to atmospheric aerosol effects and to cloud reflectance effects, whereas more modest angles are required for land surface viewing. Figure 16b shows that the aerosol optical depths (550 nm) calculated by our global model are generally close to the observed values. There are, however, some limited differences. For example, compared to the observations the aerosol optical depth calculated by MOZART-2 is larger by about 20% in the eastern United States and by 30% in Europe. However, there are also some differences when MOZART-2 is compared with AERONET and with space observations. For example, the calculated aerosol optical depth in eastern Asia is larger than the values provided by AERONET, but it is similar to the MODIS/MISR observations. As for the comparison with AERONET, the calculated aerosol optical depth is in good agreement with the measurements in the important biomass burning regions (of the Amazon and Africa), in the region of the Sahara desert, and in the remote regions of the Pacific and Atlantic oceans. Along the coast Asia and south of Hawaii, the calculated aerosol AOT is somewhat underestimated by the model.

[50] The amount of in situ observational data that can be used to evaluate global aerosol models is limited. There are, however, some surface measurements of sulfate, ammonium, black carbon, organic carbon, sea-salt, and dust aerosols that are used for this purpose. The sulfate and ammonium surface concentrations have been measured by several groups, and have been assembled by *Adams et al.* [1999]. The information on the measurements (locations, time, and reference) is listed in Table 7 of *Adams et al.* [1999]. Black carbon and organic carbon concentrations are provided by *Lioussé et al.* [1996], with measurement information listed in their Tables 4 and 5. Sea-salt aerosol data are reported by several groups and summarized by *Gong et al.* [1997]. Dust surface measurements are listed by *Zender et al.* [2003]. Figure 17 provides a comparison between measured and calculated

Table 1. Comparison of Global Mean Aerosol Column Mass Density Between MOZART and 13 Models Considered in AEROCOM Project^a

	MOZART	AEROCOM	
		Model Median	Range
SO ₄	4.30	3.65	2.2–5.6
BC	0.45	0.40	0.2–0.7
OC	2.00	2.59	1.5–5.3
Sea salt	25.9	14.2	9–42
Dust	30.4	30.5	9–121
All	63	54	27–139

^aValues are given in mg/m².

surface concentrations for different types of aerosol particles. From the data shown in this figure, one can derive that the calculated sulfate aerosol, black carbon aerosol, and organic carbon aerosol surface concentrations are overestimated on the average (statistical bias) by 21, 18, and 15%, respectively. The calculated ammonium, sea-salt, and dust surface concentrations are underestimated by 30, 12, and 15%, respectively. The high sulfate and carbonaceous concentrations derived by the model are consistent with the comparison of the model results with MISR, MODIS, and AERONET data reported above. It shows that model overestimates sulfate and carbonaceous aerosols, especially in the eastern United States, Europe, and eastern Asia. The overestimation of sulfate and black carbon aerosols can lead to overestimation in the impact of aerosol on tropospheric oxidants as described in sections 5 and 6.

[51] The total aerosol mass densities as derived by 13 global models (including the MOZART-2 aerosol model) are compared within the AEROCOM project. AEROCOM is an international initiative described on the web site, <http://nansen.ipsl.jussieu.fr/AEROCOM/data.html>. This model intercomparison (see the website and *Kinne et al.* [2003]) shows that there is a large variability among the different models (see Table 1). However, the models predict similar orders of magnitudes for the total aerosol mass. The highest mass density of aerosols is provided by mineral dust (DU, with model median of 30.5 mg/m²), and is followed by sea salt (SS, 25.9 mg/m²), sulfate (SU, 4.30 mg/m²), organic carbon (OC, 2.00 mg/m²), and black carbon (BC, 0.45 mg/m²). The calculated total mass density among the models ranges from 27 to 139 mg/m² (2.2 to 5.6 mg/m² for sulfate, 0.20 to 0.70 mg/m² for black carbon, 1.5 to 5.3 mg/m² for organic carbon, 9 to 121 mg/m² for dust, from 9 to 42 mg/m² for sea salt). The corresponding values calculated by MOZART-2 are 63 mg/m² for the total aerosol mass density and 4.3, 0.45, 3.2, 30.4, 25.3 for the individual aerosol types, respectively. Overall, the MOZART-2 model provides aerosol burdens that are in the range of the burdens provided by the 13 models.

5. Effect of Heterogeneous Reactions

[52] Heterogeneous reactions on the surface of aerosol particles have the potential to affect gas-phase oxidants [*Jacob, 2000*]. *DeMore et al.* [2000] summarize possible heterogeneous reactions on various aerosol surfaces. In Table 5–2 of *DeMore et al.* [2000], more than 60 reactions are considered. It is therefore important to

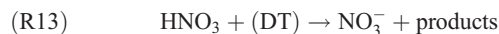
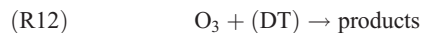
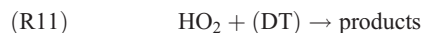
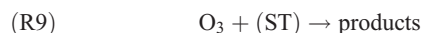
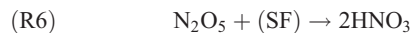
Table 2. Aerosol Properties Adopted in MOZART-2

	Density, g/cm ³	Mean Radius, μm	Refractive Index
Sulfate	1.7	0.24	1.36–10 ^{−8} _i
Ammonium nitrate	1.7	0.15	1.36–10 ^{−8} _i
Black carbon	1.0	0.04	1.75–0.46 _i
Organic carbon	1.8	0.13	1.42–0.002 _i
Secondary OC	1.8	0.13	1.42–0.002 _i
Sea salt			
Bin 1	2.2	0.3	1.37–10 ^{−8} _i
Bin 2	2.2	1.0	1.37–10 ^{−8} _i
Bin 3	2.2	3.3	1.37–10 ^{−8} _i
Bin 4	2.2	7.5	1.37–10 ^{−8} _i
Mineral dust			
Bin 1	2.5	0.75	1.58–0.014 _i
Bin 2	2.65	1.25	1.58–0.014 _i
Bin 3	2.65	2.50	1.58–0.014 _i
Bin 4	2.65	4.50	1.58–0.014 _i

determine which heterogeneous reactions are likely to affect the tropospheric composition. For such a reaction to be important, several conditions must be satisfied: (1) the probability of occurrence (uptake coefficient of oxidants on aerosol surface) of potential reactions must be sufficiently high, (2) the aerosol surface area, which provides reactive surfaces, must be large, and (3) the ratio between heterogeneous and gas phase reactions affecting a given compound must be close to or higher than 1. If the gas phase removal of a compound is faster than its heterogeneous removal, the heterogeneous reaction is unlikely to play a significant role.

[53] The reaction of N₂O₅ on sulfate aerosol, which produces HNO₃, has been measured by several groups who have reported reaction probabilities (γ) ranging from 0.02 to 0.20 [Van Doren *et al.*, 1991; Hanson and Ravishankara, 1992; Zhang *et al.*, 1995]. This reaction probability is less uncertain than other probabilities of heterogeneous reactions. In our model a value of 0.04 is used in the calculations. Hanson *et al.* [1992] have measured an uptake probability of 0.07 to 1.0 for HO₂ on sulfate aerosols. In the JPL report [DeMore *et al.*, 2000] values ranging from 0.05 to >0.2 are listed. A value of 0.2 is used in our model. The uptake of gas-phase formaldehyde, CH₂O, by sulfate aerosols has been measured by Jayne *et al.* [1996]. Their measurements show that the uptake coefficient for CH₂O by sulfate aerosols ranges from 0.012 to 0.025 when the weight percentage of sulfate varies from 55% to 70%, and the temperature changes from 240 K to 280 K. A value of 0.022 is adopted here. However, this value should be regarded as a solubility-determined upper limit. The reaction of O₃ on the surface of soot has been measured in a number of laboratory experiments, and the measured values are very different from each other. Fendel *et al.* [1995], Fendel and Ott [1993], and Rogaski *et al.* [1997] report that O₃ reacts on black carbon particles with an uptake coefficient ranging from 2 × 10^{−4} to 3.3 × 10^{−3}, but the recent study by Saathoff *et al.* [1999] shows that the uptake coefficient could be as low as 10^{−5}. Saathoff *et al.* [1999] argue that the smaller reaction coefficient for O₃ on soot surface provided by their measurements address the heterogeneous processes at longer timescale (hours). DeMore *et al.* [2000] recommend a small uptake probability for

aged soot of γ = 1.8 × 10^{−4} [exp (−1000/T)]; this expression is used in our study. The heterogeneous reactions on mineral dust are characterized by large uncertainties, which need to be resolved by laboratory measurements. In this study we used the recommended values from Dentener and Crutzen [1996] for O₃, HO₂, N₂O₅, HNO₃ with γ = 1.0 × 10^{−5}, 0.1, 0.04, and 0.1, respectively. In summary, seven heterogeneous reactions are included in MOZART-2.



where SF, ST, and DT represent the reactions on the surface of sulfate, soot, and dust aerosols, respectively. The adopted reaction coefficients should be regarded as exploratory and subject to further improvements through laboratory measurement.

[54] To study the heterogeneous reactions on the surface of aerosols, the aerosol surface area density needs to be estimated. To convert aerosol mass density calculated by the model to the surface area density, we assume that aerosols are spherical. The assumed mean radius and mass density of the aerosol particles are given in Table 2. With these assumptions, the aerosol surface area density A is calculated by

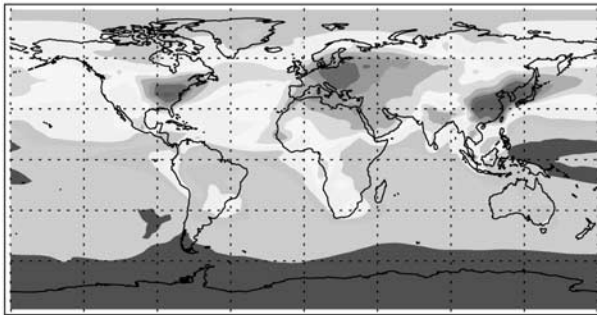
$$A = 3 M_a / (\rho r_m) \times 10^8 \quad (5)$$

where ρ(g/cm³) represents the mass density of the aerosol, r_m (cm) its mean radius, and M_a the aerosol mass (g/cm³). The pseudo first-order heterogeneous rate constant can be written as [Schwartz, 1986]

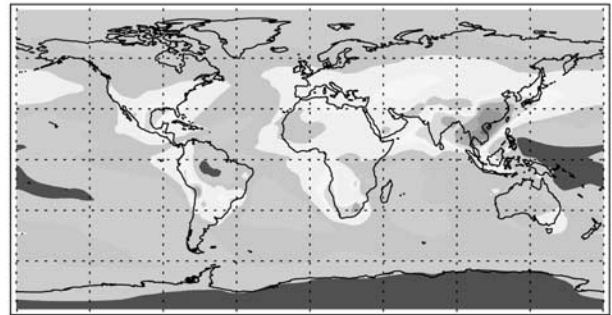
$$k_{\text{het}} = [r/D_g + 4/(c\gamma)]^{-1} A \times 10^8 \quad (6)$$

where c = [8kT/m]^{1/2} (cm/s) is the mean molecular speed of the gas at temperature T, A (m²/cm³) is the surface area density of the particles, γ is the uptake coefficient, and D_g (cm²/s) is the gas phase diffusion coefficient and r is the

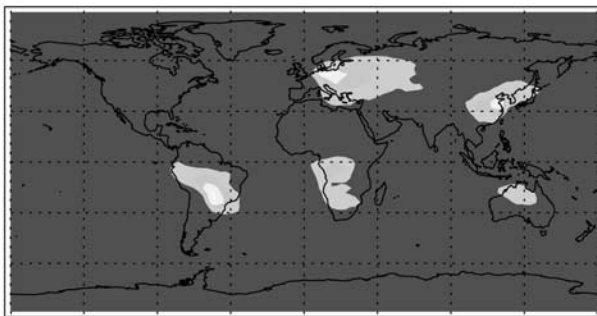
Sulfate (June)



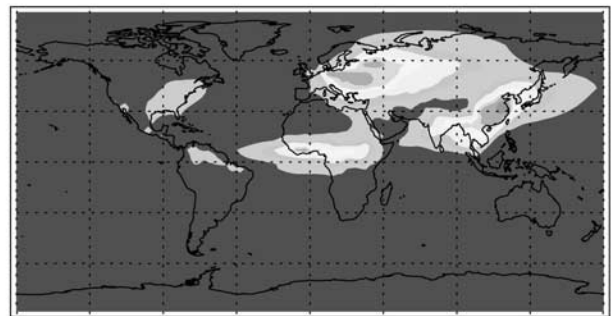
Sulfate (Dec.)



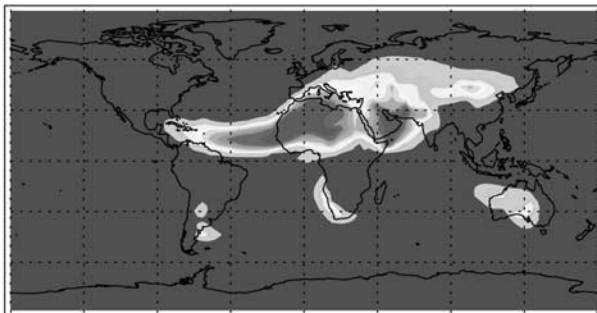
BC (June)



BC (Dec.)



Dust (June)



Dust (Dec.)

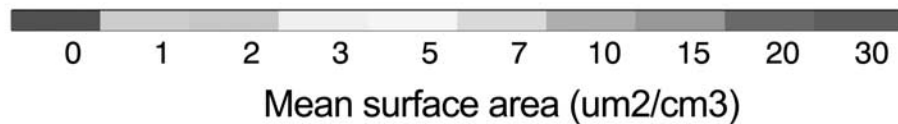
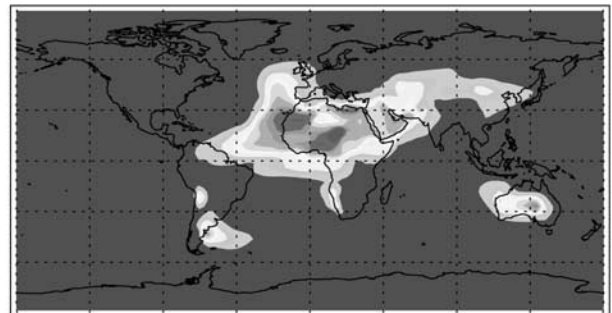


Figure 18. Calculated annual mean surface area density ($\mu\text{m}^2/\text{cm}^3$) for sulfate, black carbon, and mineral dust aerosols in June and December. See color version of this figure at back of this issue.

mean radius of the aerosol particles. According to calculations by *Perry and Green* [1984], D_g is close to $0.1 \text{ cm}^2/\text{s}$. Because the calculation of surface area is based on the assumption that the particles are spherical in shape, the uncertainty in surface areas is larger for BC and dust (which are typically clusters of small particles) than for sulfate, OC, and sea-salt particles (for which a spherical shape is more typical).

[55] Figure 18 shows the tropospheric mean surface area density ($\mu\text{m}^2/\text{cm}^3$) calculated for sulfate, black carbon, and dust in June and in December. The surface area density provided by sulfate particles is considerably larger than that

provided by dust, even though the mass density of dust is somewhat larger than that of sulfate. The soot has the smallest column mass (see Figure 6), so that its surface area is also small, but changes strongly with season. In December, the surface area density of soot increases and cannot be ignored. The highest sulfate surface area density is located in the United States, Europe, and eastern Asia, where anthropogenic sulfur emissions are largest. The maximum values are between 10 and $30 \mu\text{m}^2/\text{cm}^3$, which is equivalent to the stratospheric values following a large volcanic eruption such as that of Mt. Pinatubo in 1992 [*Brasseur et al.*, 1990; *Pitari and Rizi*, 1993; *Hofmann et*

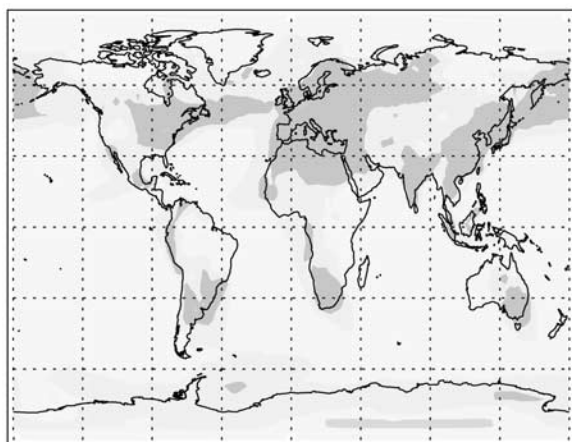
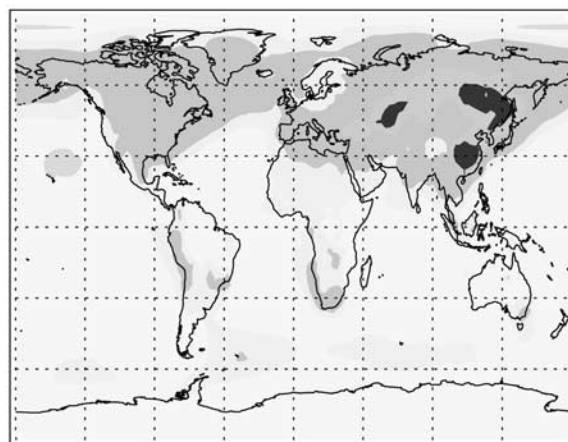
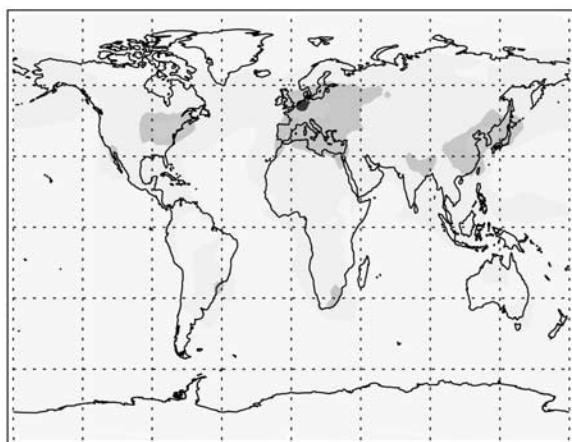
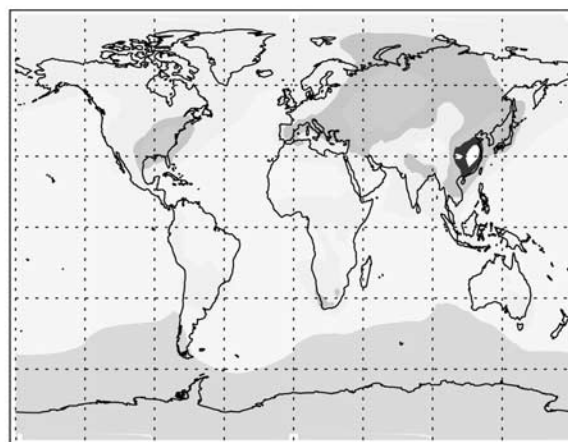
(HO_x (%) JJA)(HO_x (%) DJF)(O₃ (%) JJA)(O₃ (%) DJF)

Figure 19. Calculated changes (%) in the surface concentrations of HO_x and O₃ due to heterogeneous reactions of HO₂ on sulfate, CH₂O on sulfate, and O₃ on soot in June–July–August and December–January–February. See color version of this figure at back of this issue.

al., 1994; *Tie et al.*, 1994]. The highest soot surface area density is located in Europe and eastern Asia, but it also provides an important contribution in the Amazon and in Africa due to strong biomass burning events in these regions. However, in this case the surface area density is much smaller than in the case of sulfate particles with a maximum density of 3 to 10 $\mu\text{m}^2/\text{cm}^3$. The dust surface area density is highest in the Sahara and the surrounding regions with a maximum density of 20 to 30 $\mu\text{m}^2/\text{cm}^3$.

[56] The hydrolysis of N₂O₅ has a large effect on tropospheric oxidants as shown by several studies [*Dentener et al.*, 1993; *Tie et al.*, 2001a]. The role of this reaction will not be further investigated here. In this study, only the effects of (R7) to (R12) have been addressed.

[57] Figure 19 shows the calculated changes in the HO_x and O₃ concentrations due to the combined effects of (R7) (HO₂ + sulfate), (R8) (CH₂O + sulfate), and (R9) (O₃ +

soot) reactions at the Earth's surface. It shows that the uptake of HO₂ and CH₂O by sulfate aerosols significantly reduces the concentrations of HO_x (HO₂ + OH) in the boundary layer of the atmosphere, with up to 30 to 40% reductions in the United States, Europe, and eastern Asia where the surface area density of sulfate is the highest. Another important fact is that in those regions, NO_x concentrations are normally high [*Brasseur et al.*, 1998; *Horowitz et al.*, 2003]. As a result, the HO₂ + NO → NO₂ + OH reaction is reduced, leading to a reduced ozone production and hence to a decrease in the O₃ concentrations in these regions. The lower panels of Figure 19 shows that the largest O₃ reduction is located in the industrialized regions (United States, Europe, and eastern Asia), with a maximum decrease of 5–15%. The uptake of O₃ on soot particles plays a minor role in the reduction of O₃. For example, in central Africa, the reduction is only about 3%. However, as soot

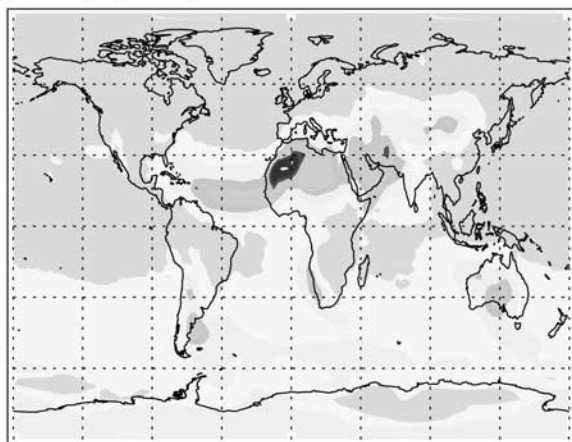
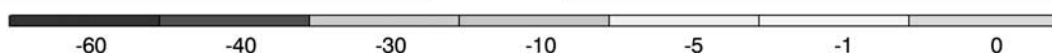
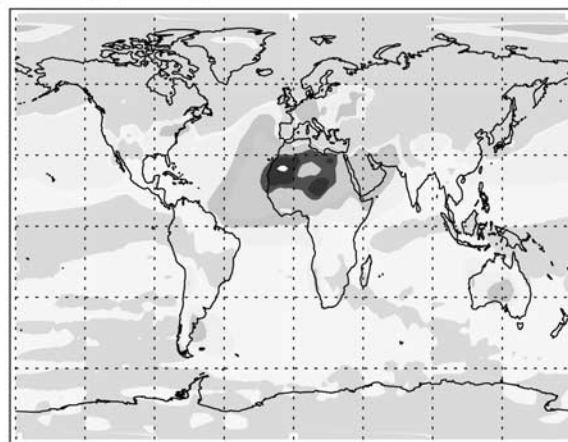
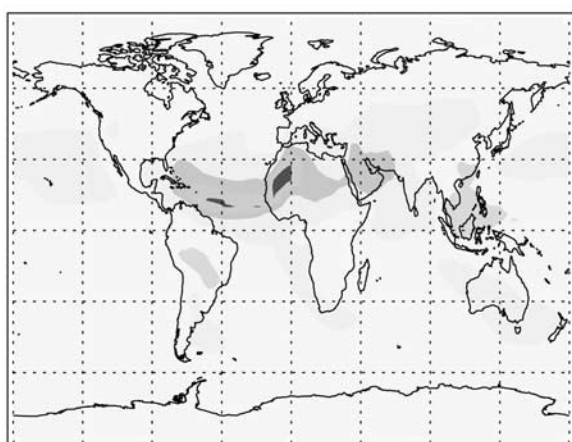
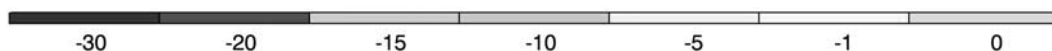
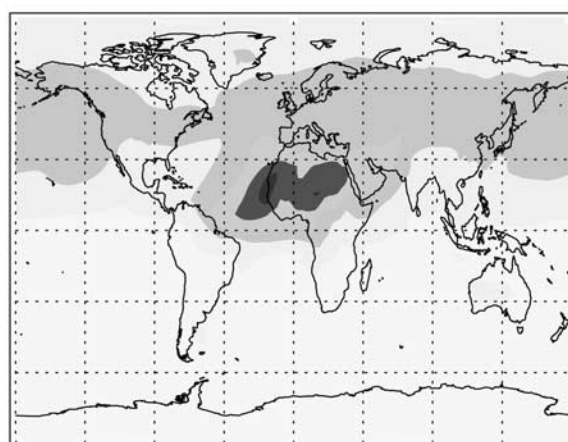
(HO_x (%) JJA)(HO_x (%) DJF)(O₃ (%) JJA)(O₃ (%) DJF)

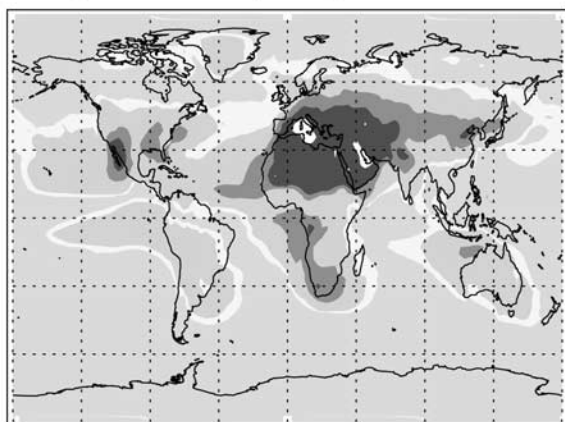
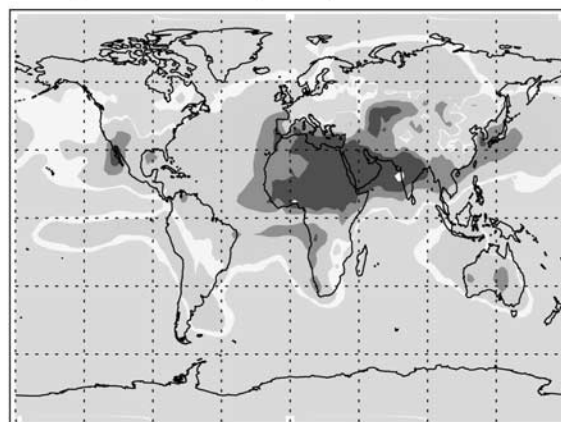
Figure 20. Calculated changes (%) in the surface concentrations of HO_x and O₃ due to heterogeneous reactions of HO₂, N₂O₅, and O₃ on dust averaged over June–July–August and December–January–February. See color version of this figure at back of this issue.

is the dominating aerosol in this region, the reduction of O₃ is mainly caused by uptake on soot. Similarly, in other soot-rich regions, an O₃ reduction of a few percent is also expected.

[58] As suggested by *Dentener and Crutzen* [1996], calcium-rich mineral dust is likely to play an important role in providing surfaces for heterogeneous reactions. Figure 20 represents the calculated changes in the concentrations of HO_x and O₃ due to the combination of the effects resulting from the (R10) (N₂O₅ + dust), (R11) (HO₂ + dust), and (R12) (O₃ + dust) reactions at the Earth's surface. It shows that the uptake of HO₂ by dust reduces significantly the HO_x concentrations, by as much as 30–40% in the region of the Sahara. Dust also affects the O₃ concentrations, e.g., with a maximum reduction of about 20% in the region of the Sahara. Because O₃ has a long chemical lifetime (a few weeks, see *Hauglustaine et al.* [1998]), the reduction of O₃

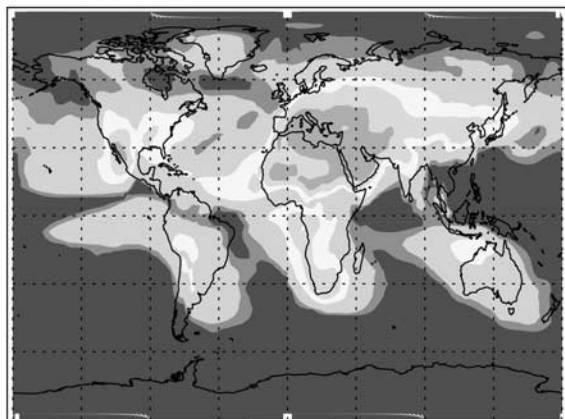
by dust affects the entire Northern Hemisphere, especially during winter. The maximum O₃ reduction of 25% shown near the Sahara was also obtained by *Dentener and Crutzen* [1996], however using a reaction coefficient ($\gamma = 2 \times 10^{-4}$) higher than that adopted in our model. Because the change in percent is strongly dependent on the background concentrations, the differences in O₃ background concentrations may be one of the reasons to explain this agreement between the two models.

[59] There is also a suggestion by *Dentener and Crutzen* [1996] that nitric acid molecules can react on the dust surface to produce nitrate (NO₃⁻ particles). This reaction reduces gas-phase HNO₃ concentrations, which are generally overestimated in global models. Figure 21 shows the calculated changes in annual mean gas phase HNO₃ surface concentrations and nitrate concentrations produced because of this reaction. It shows that the surface nitrate concentra-

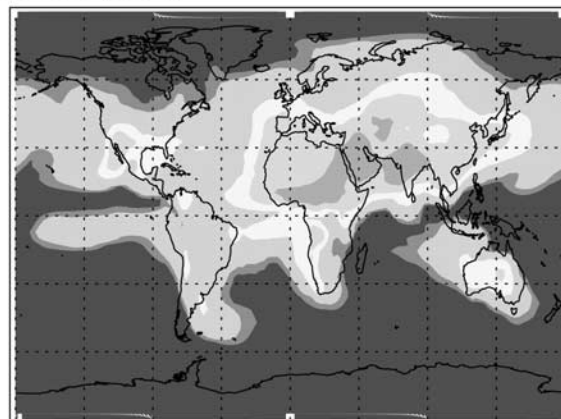
Change in HNO₃ (June)Change in HNO₃ (Dec.)

-1000 -300 -100 -30 -10 -5 0
[pptv]

Nitrate (June)



Nitrate (Dec.)



0 5 10 30 100 300 1000
[pptv]

Figure 21. Calculated concentrations of nitrate (pptv) due to the heterogeneous reaction of HNO₃ on dust (top) at surface and (bottom) at 433 mbar in June (left panels) and in December (right panels). See color version of this figure at back of this issue.

tion reaches a maximum of 1 ppb in the dust-rich regions (such as the Sahara), while a significant amount of HNO₃ (with a maximum of 1 ppbv) is removed from the gas phase. The nitrate concentration is significantly lower in the free troposphere (about 100 pptv, not shown). The calculated values for the nitrate abundance are consistent with the earlier calculations of *Liao et al.* [2003]. The impact of the decrease in gas-phase HNO₃ on ozone concentration averaged between equator and 35°N is about -5.3 percent that is consistent with the calculation by *Bauer et al.* [2004] (ranging from -3.8 to -9.0 in this region).

6. Effect on Photolysis Rates

[60] In order to assess the perturbation of aerosol particles on photolysis, the optical properties (optical depth, single

scattering albedo, and asymmetry factor) of the aerosols must be known accurately. Section 4 indicates how the optical depth is derived. The other aerosol optical parameters (single scattering albedo, asymmetry factor) are calculated according to the aerosol properties given in Table 2 using Mie theory for assumed spherical particles. The global distributions of the calculated optical depths at 550 nm are shown in Figure 15. The largest optical depth is provided by dust, followed by OC, sulfate, sea salt, BC, and ammonium nitrate. However, the magnitude of the optical depth is not the only factor that determines the effect of aerosols on the tropospheric photolysis rates and the concentrations of oxidants. Other important factors including the location of the aerosols (low latitudes are more photochemically active than high latitudes), their seasonal variations (summer photochemical activity being larger than in winter), and the ratio of absorption to scattering (single

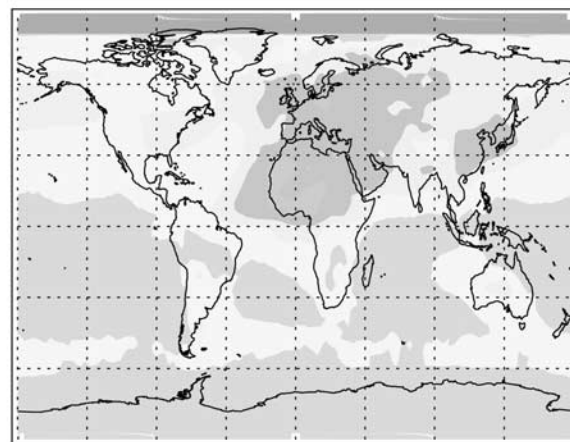
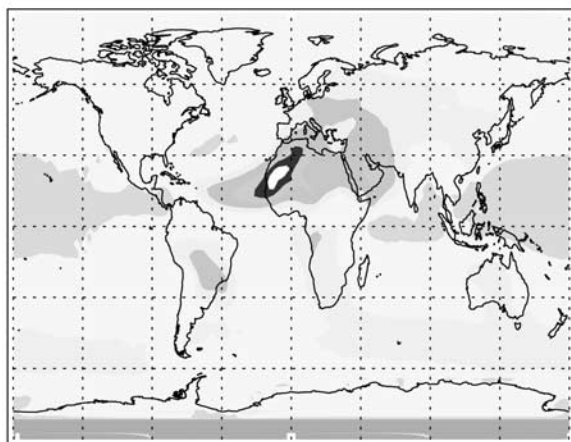
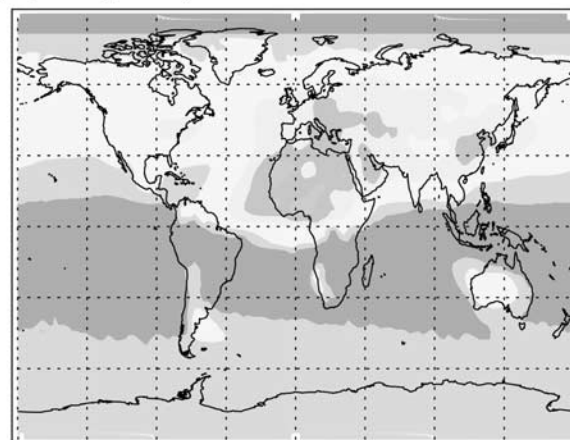
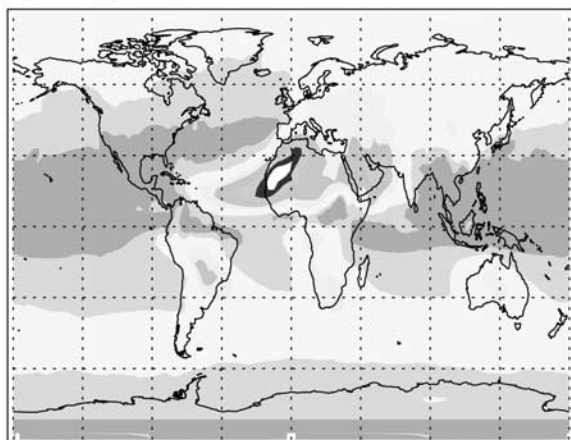
(J[O₃] -> O¹D JJA)(J[O₃] -> O¹D DJF)(J[NO₂] JJA)(J[NO₂] DJF)

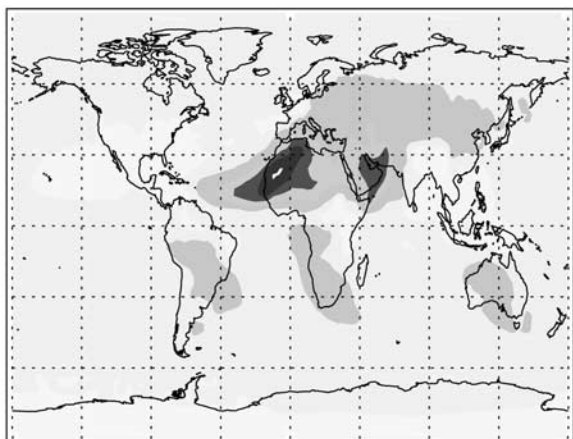
Figure 22. Calculated changes (%) in the surface photolysis frequency of O₃ and NO₂ due to the effect of aerosols on photolytic radiation averaged over June–July–August and December–January–February. See color version of this figure at back of this issue.

scattering albedo) also play substantial roles. For example, the absorption by BC is strongest among the aerosols, and the absorption of UV by BC not only reduces the UV radiation below the layer of aerosols, but also above the layer of aerosols. However, nonabsorbing (scattering) aerosols reduce the UV below the layer of aerosols, but enhance it above the aerosol layer. As a result, absorbing aerosols reduce UV radiation more efficiently than scattering aerosols. Dust aerosol has a weak absorption spectrum in the UV, and other aerosols (OC, sulfate, sea salt, and ammonium nitrate) are considered as pure scattering aerosols. *Jacobson [1998]* has estimated UV absorption by organic aerosols within Los Angeles, but this absorption is not considered here.

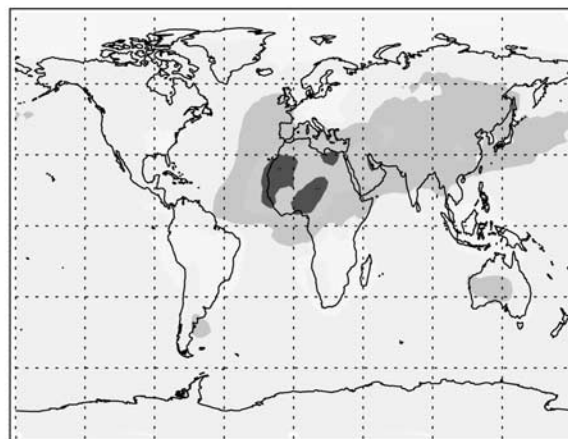
[61] The perturbation in the photolysis rates induced by aerosols is calculated by coupling the fast TUV radiation scheme with MOZART-2. Figure 22 shows the resulting changes in the $J[\text{O}_3] \rightarrow \text{O}^1\text{D} + \text{O}$ and $J[\text{NO}_2] \rightarrow \text{NO} + \text{O}_2$ rate coefficients at the Earth's surface. Photolysis of ozone

is the initial step in the production of the OH radical, and the photolysis of NO₂ is an important process in the production of tropospheric ozone. The $J[\text{O}_3]$ frequency is significantly reduced at the surface with a maximum reduction reaching 10 to 40% in the Sahara, in Europe, eastern Asia, and in the Amazon. The reduction in the Sahara is due primarily to the effect of dust, while the reductions in Europe and eastern Asia result from OC, BC, and sulfate with a small contribution from ammonium nitrate. The reduction in the Amazon is associated with the high concentrations of OC and BC. The 5–10% reduction between 40°S and 60°S is due to sea-salt aerosol. The changes in the NO₂ photolysis frequency (see lower panels of Figure 22) have a similar distribution as that of O₃ photolysis, but with magnitudes that are somewhat smaller. The location and magnitudes of the changes in $J[\text{O}_3]$ are generally similar to those calculated by *Martin et al. [2003]*, except that in the latter model the reductions are larger in India and southern Africa.

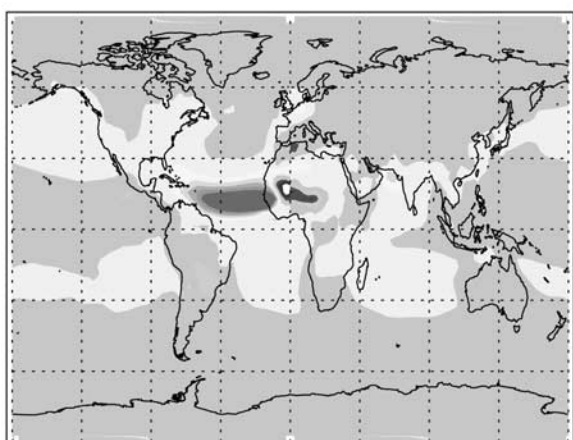
(HOX JJA)



(HOX DJF)



(O3 JJA)



(O3 DJF)

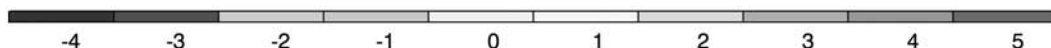
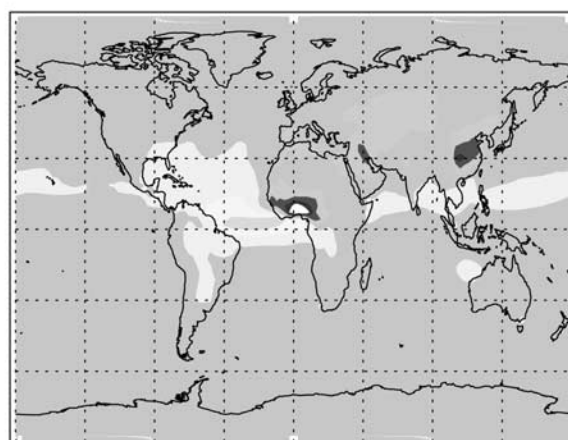


Figure 23. Calculated changes (%) in the HO_x and O₃ surface concentrations due to the effect of aerosols on radiation, averaged over June–July–August and December–January–February. See color version of this figure at back of this issue.

[62] The reduction of photolysis rate coefficients produces changes in the concentrations of tropospheric oxidants, especially HO_x and O₃. Figure 23 shows the calculated changes in the surface concentration of these species due to the perturbation in the photolysis frequencies illustrated in Figure 22. Consistent with the reduction of $J[\text{O}_3]$, HO_x is reduced by 5 to 40% with the maximum of 40% located in the Sahara. The effect on O₃ is modest compared to the impact on HO_x. The O₃ changes range globally from +5 to −4% at the surface. There is a small increase in O₃ over the Atlantic Ocean in the vicinity of the Sahara because HO_x is reduced in this region.

7. Summary

[63] A global interactive chemical and aerosol model has been developed to assess the effects of aerosols (sulfate, soot, primary organic carbon, secondary organic carbon,

ammonium nitrate, sea salt, and mineral dust) on tropospheric oxidants. This model accounts for (1) the conversion of gas-phase oxidants to condensed-phase during the aerosol formation, (2) several key heterogeneous reactions on the surface of aerosols, and (3) the effects of aerosol on photolysis rates and oxidant concentrations. We use a version of MOZART-2 that includes a fast online radiative transfer code based on the NCAR's TUV model and a newly developed scheme that describes the formation of aerosols and their interaction with tropospheric oxidants. The global aerosol distributions derived by the model are compared with satellite measurements (MODIS). The calculated aerosol abundances are in fair agreement with observations in several aspects. For example, the calculated aerosol abundances have maxima located in southern Africa, in the Amazon, and in eastern Asia in accordance with measurements. The calculated maximum optical depths in these regions are ranging from 0.4 to 0.5 in good

agreement with measurements. The outflow of the aerosols observed over the Atlantic near southern Africa is reproduced by the model. Some discrepancies are also noted. For example, the calculated aerosol mean densities are overestimated in Europe. Since the major contribution to optical depths in this region is provided by OC and sulfate aerosols, one possible explanation is that the specified anthropogenic emissions of OC and SO₂ are overestimated in Europe.

[64] Aerosols have important impacts on regional oxidants through different processes: (1) wet deposition of ammonium affects total nitrogen deposition on the surface and hence the biogeochemical cycle of nitrogen; (2) the formation of secondary organic carbon has a modest impact on tropospheric oxidants globally; (3) the heterogeneous reactions of HO₂ and CH₂O on the surface of sulfate aerosols have an important effect on the global HO_x and O₃ concentrations, leading to a 30 to 40 % reduction in the HO_x concentrations in the United States, Europe, and eastern Asia and to a 5–15% O₃ decrease; (4) the uptake of HO₂ and O₃ by dust reduces significantly HO_x and O₃ concentrations with a maximum HO_x reduction of 30–60% near the Sahara, and a 5–30% reduction ozone in almost the entire northern hemisphere in winter; and (5) aerosols also affect significantly the photolysis of O₃ and NO₂ with a maximum reduction of 10 to 40% at the surface in the Sahara, in Europe, eastern Asia, and in the Amazon, leading to a 5 to 40% reduction in the HO_x abundance and to a +5 to –4% change in O₃. All of these results should be regarded as exploratory and subject to further improvements as new laboratory measurements become available.

[65] **Acknowledgments.** The authors are grateful to Jim Smith and John Orlando for useful comments on the manuscript. Renyi Zhang acknowledges the support from the NASA New Investigator Program in Earth Science. The authors would like to thank Allen Chu at NASA GSFC for providing them with the MODIS data and Steven Kinne of the AEROCOM project for providing the intercomparison of global aerosol models. They also thank the AERONET program for providing the AOT data. The National Center for Atmospheric Research is sponsored by the National Science Foundation.

References

- Adams, P. J., H. Seinfeld, and D. M. Koch (1999), Global concentrations of tropospheric sulfate, nitrate, and ammonium aerosol simulated in a general circulation model, *J. Geophys. Res.*, *104*, 13,791–13,823.
- Bauer, S. E., Y. Balkanski, M. Schulz, D. A. Hauglustaine, and F. Dentener (2004), Global modeling of heterogeneous chemistry on mineral aerosol surfaces: Influence on tropospheric ozone chemistry and comparison to observations, *J. Geophys. Res.*, *109*, D02304, doi:10.1029/2003JD003868.
- Benkovitz, C. M., C. M. Berkowitz, R. C. Easter, S. Nemesure, R. Wagener, and S. E. Schwartz (1994), Sulfate over the North Atlantic and adjacent continental regions: Evaluation for October and November 1986 using a three-dimensional model driven by observation-derived meteorology, *J. Geophys. Res.*, *99*, 20,725–20,756.
- Benkovitz, C. M., M. T. Scholtz, J. Pacyna, L. Tarrason, J. Diagon, E. C. Voldner, P. A. Spiro, J. A. Logan, and T. E. Graedel (1996), Global gridded inventories of anthropogenic emissions of sulfur and nitrogen, *J. Geophys. Res.*, *101*, 29,239–29,253.
- Bian, H., and C. S. Zender (2003), Mineral dust and global tropospheric chemistry: Relative roles of photolysis and heterogeneous uptake, *J. Geophys. Res.*, *108*(D21), 4672, doi:10.1029/2002JD003143.
- Bouwman, A. F., D. S. Lee, W. A. H. Asman, F. J. Dentener, K. W. Van Der Hoek, and J. G. J. Olivier (1997), A global high-resolution emission inventory for ammonia, *Global Biogeochem. Cycles*, *11*, 561–587.
- Brasseur, G. P., C. Granier, and S. Walters (1990), Future changes in stratospheric ozone and the role of heterogeneous chemistry, *Nature*, *348*, 626–628.
- Brasseur, G. P., D. A. Hauglustaine, S. Walter, J. F. Muller, P. Rasch, C. Granier, and X. Tie (1998), MOZART: A global three-dimensional chemical-transport-model of the atmosphere, *J. Geophys. Res.*, *103*, 28,265–28,289.
- Chin, M., D. Jacob, G. M. Gardner, M. S. Foreman-Fowler, P. A. Spiro, and D. L. Savoie (1996), A global three-dimensional model of tropospheric sulfate, *J. Geophys. Res.*, *101*, 18,667–18,690.
- Chin, M., R. B. Rood, S.-J. Lin, J. F. Muller, and A. M. Thompson (2000), Atmospheric sulfur cycle simulated in the global model GOCART: Model description and global properties, *J. Geophys. Res.*, *105*, 24,671–24,687.
- Chu, D. A., Y. J. Kaufman, G. Zibordi, J. D. Chern, J. Mao, C. Li, and B. N. Holben (2003), Global monitoring of air pollution over land from the Earth Observing System-Terra Moderate Resolution Imaging Spectroradiometer (MODIS), *J. Geophys. Res.*, *108*(D21), 4661, doi:10.1029/2002JD003179.
- Cooke, W. F., and J. J. N. Wilson (1996), A global black carbon aerosol model, *J. Geophys. Res.*, *101*, 19,395–19,409.
- Cunnold, D. M., et al. (2002), In situ measurements of atmospheric methane at GAGE/AGAGE sites during 1985–2000 and resulting source inferences, *J. Geophys. Res.*, *107*(D14), 4225, doi:10.1029/2001JD001226.
- DeMore, W. B., et al. (2000), Chemical kinetics and photochemical data for use in stratospheric modeling, *JPL*, 200.
- Dentener, F. J., and P. J. Crutzen (1994), A three-dimensional model of the global ammonia cycle, *J. Atmos. Chem.*, *19*, 331–369.
- Dentener, F. J., and P. J. Crutzen (1996), Role of mineral aerosol as a reactive surface in the global troposphere, *J. Geophys. Res.*, *101*, 2869–2889.
- Dentener, F. J., G. Carmichael, Y. Zhang, J. Lelieveld, and P. J. Crutzen (1993), Reaction of N₂O₅ on tropospheric aerosols: Impact on the global distributions of NO_x, O₃, and OH, *J. Geophys. Res.*, *98*, 7149–7163.
- Edwards, D. P., et al. (2003), Tropospheric ozone over the tropical Atlantic: A satellite perspective, *J. Geophys. Res.*, *108*(D8), 4237, doi:10.1029/2002JD002927.
- Emmons, L., et al. (2000), Data composites of airborne observations of tropospheric ozone and its precursors, *J. Geophys. Res.*, *105*, 20,497–20,538.
- Emmons, L. K., et al. (2003), Budget of tropospheric ozone during TOPSE from two chemical transport models, *J. Geophys. Res.*, *108*(D8), 8372, doi:10.1029/2002JD002665.
- Feichter, J., E. Kjellstrom, H. Rodhe, F. Dentener, J. Lelieveld, and G. Roelofs (1996), Simulation of the tropospheric sulfur cycle in a global climate model, *Atmos. Environ.*, *30*, 1693–1707.
- Fendel, W., and A. S. Ott (1993), Ozone depletion potential of carbon aerosol particles, *J. Aerosol Sci.*, *24*, 317–318.
- Fendel, W., D. Matter, H. Burtscher, and A. Schmidt-Ott (1995), Interaction between carbon or iron aerosol particles and ozone, *Atmos. Environ.*, *29*, 967–973.
- Friedl, R. (1997), Atmospheric effects of subsonic aircraft: Interim assessment report of the advanced subsonic technology program, *NASA Ref. Publ.*, *2400*, 143 pp.
- Friedlingstein, P., I. Fung, E. Holland, J. John, A. Brasseur, D. Erickson, and D. Schimel (1995), On the contribution of CO₂ fertilization to the missing biospheric sink, *Global Biogeochem. Cycles*, *9*, 541–556.
- Gilliland, A. B., T. J. Butler, and G. E. Likens (2002), Monthly and annual bias in weekly (NADP/NTN) versus daily (AIRMON) precipitation chemistry data in the eastern USA, *Atmos. Environ.*, *36*, 5197–5206.
- Ginoux, P., M. Chin, I. Tegen, J. Prospero, B. Holben, O. Dubovik, and S.-J. Lin (2001), Sources and distributions of dust aerosols simulated with the GOCART model, *J. Geophys. Res.*, *106*, 20,225–20,273.
- Golden, D. M., and J. Manion (1992), Applications of chemical kinetics, *Adv. Chem. Kinet. Dyn.*, *1*, 187–276.
- Gong, S., L. A. Barrie, and I.-P. Blanchet (1997), Modeling sea-salt aerosols in the atmosphere: 1. Model development, *J. Geophys. Res.*, *102*, 3805–3818.
- Hack, J. J., B. A. Boville, B. P. Briegleb, J. T. Kiehl, P. J. Rasch, and D. L. Williamson (1993), Description of the NCAR community climate model (CCM2), *Tech. Note NCAR/TN-382+STR*, 108 pp., Natl. Cent. for Atmos. Res., Boulder, Colo.
- Hagen, D. E., M. B. Trueblood, and P. D. Whitefield (1992), A field sampling of jet exhaust aerosols, *Particulate Sci. Technol.*, *10*, 53–63.
- Hansen, J. E., and L. D. Travis (1974), Light scattering in planetary atmospheres, *Space Sci. Rev.*, *16*, 527–610.
- Hanson, D. R., and A. R. Ravishankara (1992), Investigation of the reactive and nonreactive processes involving ClONO₂ and HCl on water and nitric acid doped ice, *J. Phys. Chem.*, *96*, 2682–2691.
- Hanson, D. R., J. B. Burkholder, A. R. Ravishankara, and C. J. Howard (1992), The accommodation coefficients of OH and HO₂ on aqueous surfaces, *J. Phys. Chem.*, *96*, 4979.
- Hansson, M., and K. Holmen (2001), High latitude biospheric activity during the last glacial cycle revealed by ammonium variations in Greenland ice cores, *Geophys. Res. Lett.*, *28*, 4239–4242.

- Hauglustaine, D. A., G. P. Brasseur, S. Walter, P. Rasch, J. F. Muller, L. Emmons, and M. A. Carroll (1998), MOZART: A global three-dimensional chemical-transport-model of the atmosphere: 2. Model results and evaluation, *J. Geophys. Res.*, *103*, 28,291–28,335.
- Hauglustaine, D. A., G. P. Brasseur, and J. S. Levine (1999), A sensitivity simulation of tropospheric ozone changes due to the 1997 Indonesian fire emissions, *Geophys. Res. Lett.*, *26*, 3305–3308.
- Hauglustaine, D. A., et al. (2001), On the role of lightning NO_x in the formation of tropospheric ozone plumes: A global model perspective, *J. Atmos. Chem.*, *38*, 277–294.
- He, S., and G. R. Carmichael (1999), Sensitivity of photolysis rates and ozone production in the troposphere to aerosol properties, *J. Geophys. Res.*, *104*, 26,307–26,324.
- Hofmann, D. J., S. J. Oltmans, W. D. Komhyr, J. M. Harris, J. A. Lathrop, A. O. Langford, T. Deshler, B. J. Johnson, A. Torres, and W. A. Matthews (1994), Ozone loss in the lower stratosphere over the United States in 1992–1993: Evidence for heterogeneous chemistry on the Pinatubo aerosol, *Geophys. Res. Lett.*, *21*, 65–68.
- Horowitz, L. W., et al. (2003), A global simulation of tropospheric ozone and related tracers: Description and evaluation of MOZART, version 2, *J. Geophys. Res.*, *108*(D24), 4784, doi:10.1029/2002JD002853.
- Intergovernmental Panel on Climate Change (IPCC) (2001), *Climate Change 2001: The Scientific Basis, Contribution of Working Group I to the Third Assessment Report of the Intergovernmental Panel on Climate Change*, edited by J. T. Houghton et al., 881 pp., Cambridge Univ. Press, New York.
- Jacob, D. J. (2000), Heterogeneous chemistry and tropospheric ozone, *Atmos. Environ.*, *34*, 2131–2159.
- Jacobson, M. (1998), Studying the effects of aerosols on vertical photolysis rate coefficient and temperature profiles over an urban air shed, *J. Geophys. Res.*, *103*, 10,593–10,604.
- Jayne, J. T., D. R. Worsnop, C. E. Kolb, E. Schwartz, and P. Davidovits (1996), Uptake of gas-phase formaldehyde by aqueous acid surfaces, *J. Phys. Chem.*, *100*, 8015–8022.
- Kaufman, Y. J., A. E. Wald, L. A. Remer, B. C. Gao, and R. R. Li (1997), The MODIS 2.1- μ m channel: A correlation with visible reflectance for use in remote sensing of aerosol, *Geosci. Remote Sens.*, *35*(5), 1286–1298.
- Kinne, S., et al. (2003), Monthly averages of aerosol properties: A global comparison among models, satellite data, and AERONET ground data, *J. Geophys. Res.*, *108*(D20), 4634, doi:10.1029/2001JD001253.
- Lacis, A. A., and M. I. Mishchenko (1995), Climate forcing, climate sensitivity, and climate response: A radiative modeling perspective on atmospheric aerosols, in *Aerosol Forcing of Climate*, edited by R. J. Charlson and J. Heintzenberg, pp. 11–42, John Wiley, Hoboken, N. J.
- Lack, D. A., X. X. Tie, N. D. Bofinger, A. N. Wiegand, and S. Madronich (2004), Seasonal variability of secondary organic aerosol: A global modeling study, *J. Geophys. Res.*, *109*, D03203, doi:10.1029/2003JD003418.
- Lamarque, J.-F., and P. G. Hess (2003), Model analysis of the temporal and geographical origin of the CO distribution during the TOPSE campaign, *J. Geophys. Res.*, *108*(D4), 8354, doi:10.1029/2002JD002077.
- Lamarque, J.-F., B. V. Khattatov, J. C. Gille, and G. P. Brasseur (1999), Assimilation of Measurement of Air Pollution from Space (MAPS) CO in a global three-dimensional model, *J. Geophys. Res.*, *104*, 26,209–26,218.
- Liao, H., Y. L. Yung, and J. H. Seinfeld (1999), Effects of aerosols on tropospheric photolysis rates in clear and cloudy atmospheres, *J. Geophys. Res.*, *104*, 23,697–23,707.
- Liao, H., P. J. Adams, S. H. Chung, J. H. Seinfeld, L. J. Mickley, and D. J. Jacob (2003), Interactions between tropospheric chemistry and aerosols in a unified general circulation model, *J. Geophys. Res.*, *108*(D1), 4001, doi:10.1029/2001JD001260.
- Li-Jones, X., H. B. Maring, and J. M. Prospero (1998), Effect of relative humidity on light scattering by mineral dust aerosol as measured in the marine boundary layer over the tropical Atlantic Ocean, *J. Geophys. Res.*, *103*, 31,113–31,121.
- Liousse, C., H. Cachier, and S. G. Jennings (1993), Optical and thermal measurements of black carbon content in different environments: Variation of the specific attention cross-section, σ_0 , *Atmos. Environ.*, *27*, 1203–1211.
- Liousse, C., J. E. Penner, C. Chang, J. J. Walton, H. Eddleman, and H. Cachier (1996), A global three-dimensional model study of carbonaceous aerosols, *J. Geophys. Res.*, *101*, 19,411–19,432.
- Luo, C., N. M. Mahowald, and J. del Corral (2003), Sensitivity study of meteorological parameters on mineral aerosol mobilization, transport, and distribution, *J. Geophys. Res.*, *108*(D15), 4447, doi:10.1029/2003JD003483.
- Madronich, S. (1987), Photodissociation in the atmosphere: 1. Actinic flux and the effect of ground reflections and clouds, *J. Geophys. Res.*, *92*, 9740–9752.
- Martin, R. V., D. J. Jacob, R. M. Yantosca, M. Chin, and P. Ginoux (2003), Global and regional decreases in tropospheric oxidants from photochemical effects of aerosols, *J. Geophys. Res.*, *108*(D3), 4097, doi:10.1029/2002JD002622.
- Mauzerall, D. L., D. Narita, H. Akimoto, L. Horowitz, S. Walters, D. Hauglustaine, and G. Brasseur (2000), Seasonal characteristics of tropospheric ozone production and mixing ratios over east Asia: A global three-dimensional chemical transport model analysis, *J. Geophys. Res.*, *105*, 17,895–17,910.
- McFiggans, G., R. A. Cox, J. C. Mössinger, B. J. Allan, and J. M. C. Plane (2002), Active chlorine release from marine aerosols: Roles for reactive iodine and nitrogen species, *J. Geophys. Res.*, *107*(D15), 4271, doi:10.1029/2001JD000383.
- Parungo, F., C. Nagamoto, M. Y. Zhou, A. D. A. Hansen, and J. Harris (1994), Aeolian transport of aerosol black carbon from China to the ocean, *Atmos. Environ.*, *28*, 3251–3260.
- Penner, J. E., H. Eddleman, and T. Novakov (1993), Towards the development of a global inventory for black carbon emissions, *Atmos. Environ., Part A*, *27*, 1277–1295.
- Perry, R. H., and D. Green (1984), *Perry's Chemical Engineers' Handbook*, pp. 3–285, McGraw-Hill, New York.
- Pickering, K. E., et al. (1998), Vertical distribution of lightning NO_x for use in regional and global chemical transport models, *J. Geophys. Res.*, *103*, 31,203–31,216.
- Pitari, G., and V. Rizzi (1993), An estimate of the chemical and radiative perturbation of stratospheric ozone following the eruption of Mt. Pinatubo, *J. Atmos. Sci.*, *50*, 3260–3276.
- Price, C., J. Penner, and M. Prather (1997), NO_x from lightning: 1. Global distribution based on lightning physics, *J. Geophys. Res.*, *102*, 5929–5941.
- Rasch, P. J., N. M. Mahowald, and B. E. Eaton (1997), Representations of transport, convection, and the hydrologic cycle in chemical transport models: Implications for the modeling of short-lived and soluble species, *J. Geophys. Res.*, *102*, 28,127–28,138.
- Rogaski, C. A., et al. (1997), Reactive uptake and hydration experiments on amorphous carbon treated with NO₂, SO₂, O₃, HNO₃, and H₂SO₄, *Geophys. Res. Lett.*, *24*, 381–384.
- Saathoff, H., S. Kamm, O. Mohler, K.-H. Naumann, and U. Schurath (1999), The interaction of soot aerosol with O₃, NO₂, NO₃, N₂O₅, HNO₃, and HO₂, paper presented at Sixth Scientific Conference of the International Global Atmospheric Chemistry Project (IGAC), Int. Global Atmos. Chem. Proj., Bologna, Italy, 13–17 Sept.
- Sander, R., Y. Rudich, R. von Glasow, and P. J. Crutzen (1999), The role of BrNO₂ in marine troposphere chemistry: A model study, *Geophys. Res. Lett.*, *26*, 2857–2860.
- Schwartz, S. E. (1986), Mass-transport considerations pertinent to aqueous phase reactions of gases in liquid water clouds, in *Chemistry of Multiphase Atmospheric System, NATO ASI Ser., Ser. G*, vol. 6, edited by W. Jaeschke, pp. 415–471, Springer, New York.
- Seinfeld, J. H., and S. N. Pandis (1998), *Atmospheric Chemistry and Physics*, John Wiley, Hoboken, N. J.
- Stelson, A. W., and J. H. Seinfeld (1982), Relative humidity and pH dependence of the vapor pressure of ammonium nitrate-nitric acid solutions at 25°C, *Atmos. Environ.*, *16*, 993–1000.
- Stubenrauch, C. J., A. D. Del Genio, and W. B. Rossow (1997), Implementation of subgrid cloud vertical structure inside a GCM and its effect on the radiation budget, *J. Clim.*, *10*, 273–287.
- Tanre, D., Y. J. Kaufman, M. Herman, and S. Mattoo (1997), Remote sensing of aerosol properties over oceans using the MODIS/EOS spectral radiances, *J. Geophys. Res.*, *102*, 16,971–16,988.
- Tegen, I., and R. Miller (1998), A general circulation model study on the interannual variability of soil dust aerosol, *J. Geophys. Res.*, *103*, 25,975–25,995.
- Tie, X., G. P. Brasseur, B. Briegleb, and C. Granier (1994), Two-dimensional simulation of Pinatubo aerosol and its effect on stratospheric ozone, *J. Geophys. Res.*, *99*, 20,545–20,562.
- Tie, X., G. Brasseur, L. Emmons, L. Horowitz, and D. Kinnison (2001a), Effects of aerosols on tropospheric oxidants: A global model study, *J. Geophys. Res.*, *106*, 2931–2964.
- Tie, X., G. Brasseur, R. Zhang, L. Emmons, and W. Lei (2001b), Effects of lightning on reactive nitrogen and nitrogen reservoir species in the troposphere, *J. Geophys. Res.*, *106*, 3167–3178.
- Tie, X., R. Zhang, G. Brasseur, and W. Lei (2002), Global NO_x production, *J. Atmos. Chem.*, *43*, 61–74.
- Tie, X., A. Guenther, and E. Holland (2003a), Biogenic methanol and its impacts on tropospheric oxidants, *Geophys. Res. Lett.*, *30*(17), 1881, doi:10.1029/2003GL017167.
- Tie, X., S. Madronich, S. Walters, R. Zhang, P. Rasch, and W. Collins (2003b), Effect of clouds on photolysis and oxidants in the troposphere, *J. Geophys. Res.*, *108*(D20), 4642, doi:10.1029/2003JD003659.

- Tie, X., et al. (2003c), Effect of sulfate aerosol on tropospheric NO_x and ozone budgets: Model simulations and TOPSE evidence, *J. Geophys. Res.*, *108*(D4), 8364, doi:10.1029/2001JD001508.
- Van Doren, J. M., L. R. Watson, P. Davidovits, D. R. Worsnop, M. S. Zahniser, and C. E. Kolb (1991), Uptake on N_2O_5 and HNO_3 by aqueous sulfuric acid droplets, *J. Phys. Chem.*, *95*, 1684–1689.
- Wesely, M. L. (1989), Parameterization of surface resistance to gaseous dry deposition in regional-scale numerical models, *Atmos. Environ.*, *23*, 1293–1304.
- Zender, C. S., H. Bian, and D. Newman (2003), Mineral Dust Entrainment and Deposition (DEAD) model: Description and 1990s dust climatology, *J. Geophys. Res.*, *108*(D14), 4416, doi:10.1029/2002JD002775.
- Zhang, G. J., and N. A. McFarlane (1995), Sensitivity of climate simulations to the parameterization of cumulus convection in the Canadian Climate Center general circulation model, *Atmos. Ocean*, *33*, 407–446.
- Zhang, R., M. T. Leu, and L. F. Keyser (1995), Sulfuric acid monohydrate: Formation and heterogeneous chemistry in the stratosphere, *J. Geophys. Res.*, *100*, 18,845–18,854.
- Zhang, R., X. Tie, and D. Bond (2003), Impacts of anthropogenic and natural NO_x sources over the U.S. on tropospheric chemistry, *Proc. Natl. Acad. Sci. U. S. A.*, *100*, 1505–1509.
-
- G. Brasseur, Max Planck Institute of Meteorology, Bundestrasse 55, D-20146 Hamburg, Germany.
- D. P. Edwards, S. Madronich, N. Mahowald, X. Tie, and S. Walters, National Center for Atmospheric Research, 1850 Table Mesa Drive, Boulder, CO 80305, USA. (xxtie@ucar.edu)
- P. Ginoux, Geophysical Fluid Dynamics Laboratory, NOAA, Forrester Campus, Route 1, P. O. Box 308, Princeton, NJ 08542, USA.
- C. Lou, Institute for Computational Earth Systems Science, University of California, Santa Barbara, Box 3060, Santa Barbara, CA 93106-3060, USA.
- R. Zhang, Department of Atmospheric Science, Texas A&M University, 1204 Eller O&M Building, 50 TAMU, College Station, TX 77843-3150, USA.

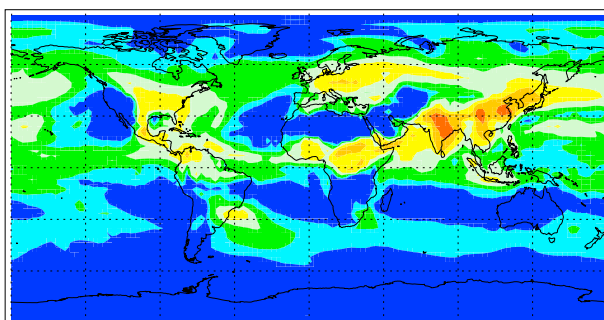
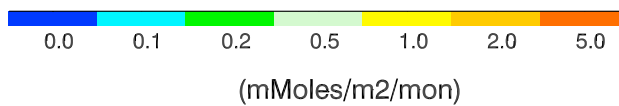
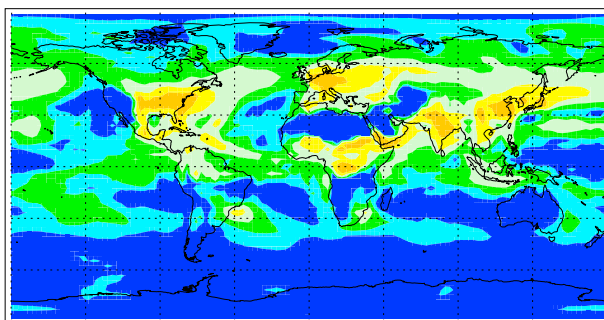
NH₄ Wet DepositionNO₃ Wet Deposition

Figure 4. Calculated global distribution of annually averaged ammonium (NH₄⁺) and nitrate (NO₃⁻) deposition (mmol/m²/month).

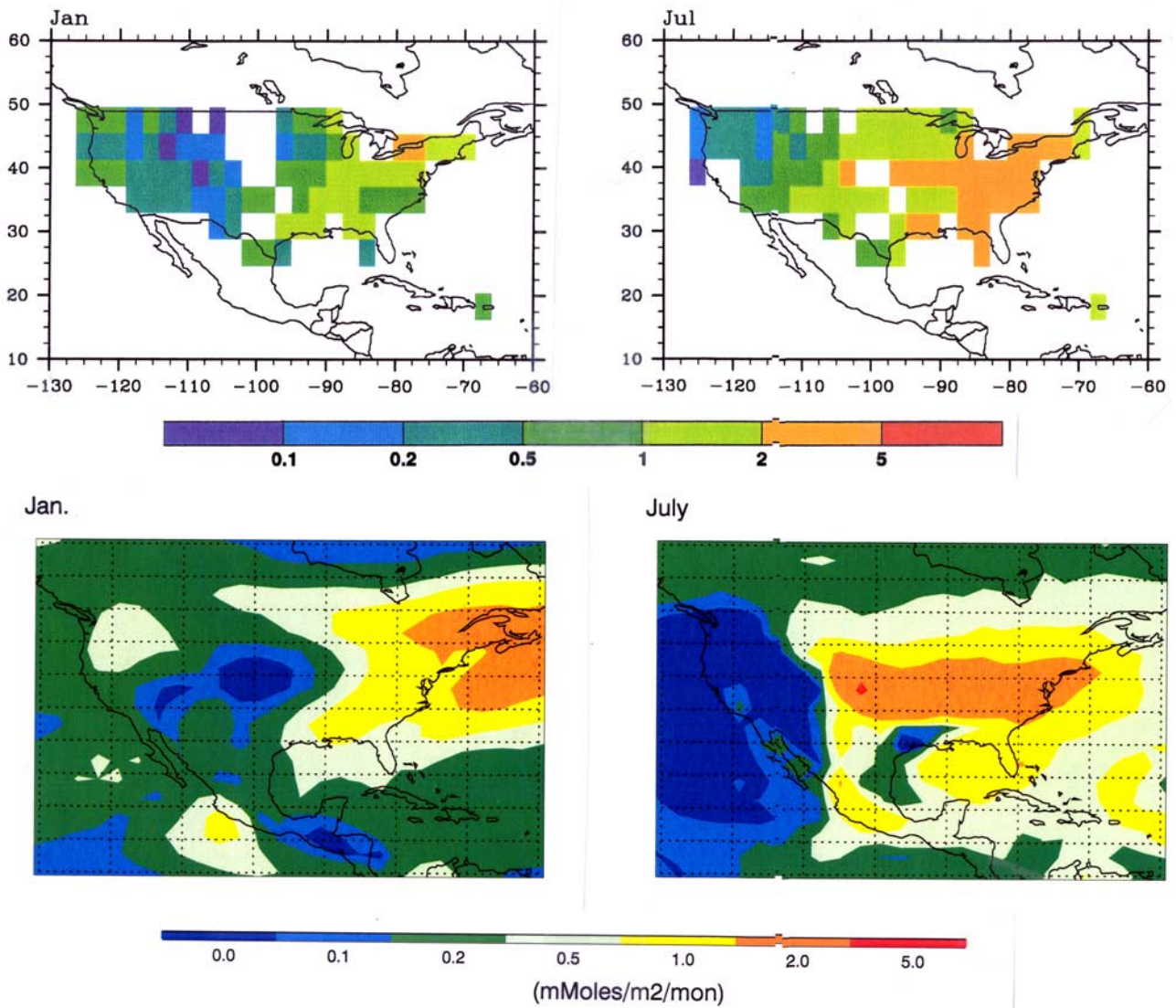
NADP Monthly Mean Nitrate Wet Deposition (mMoles/m²/mon)

Figure 5. Calculated and observed (NADP) ammonium (NH_4^+) and nitrate (NO_3^-) deposition ($\text{mmol/m}^2/\text{month}$) in the United States in January and July.

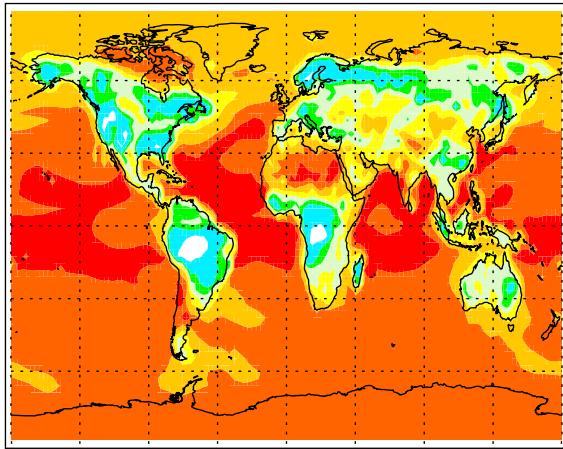
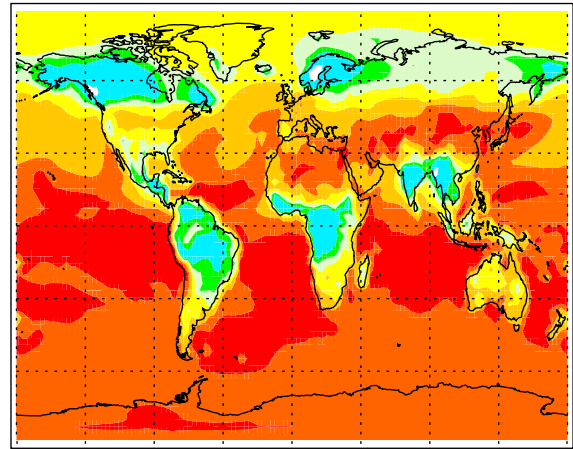
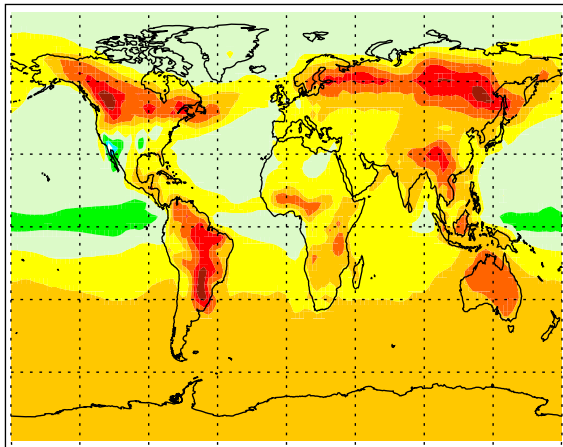
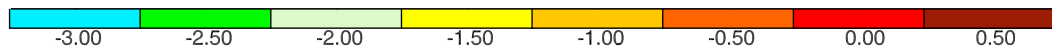
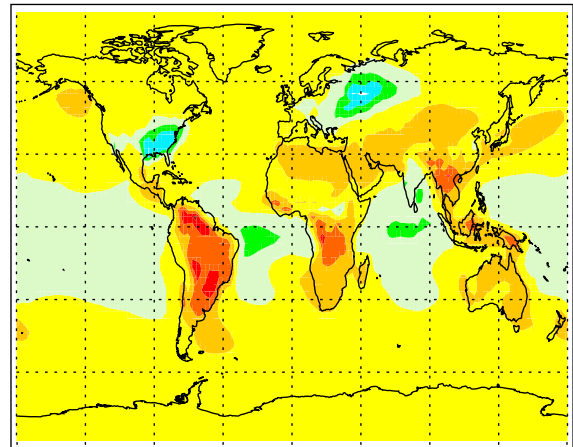
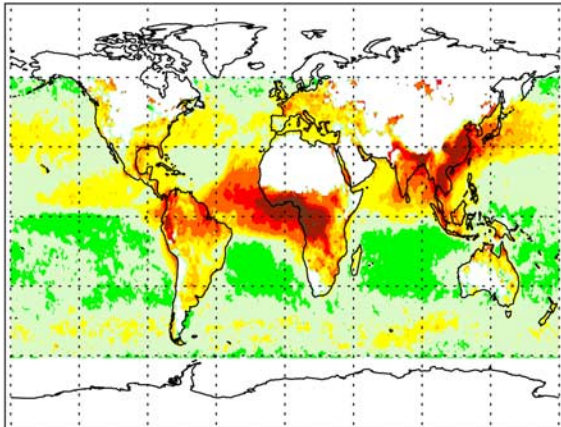
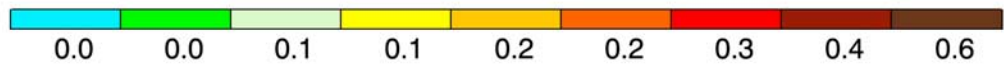
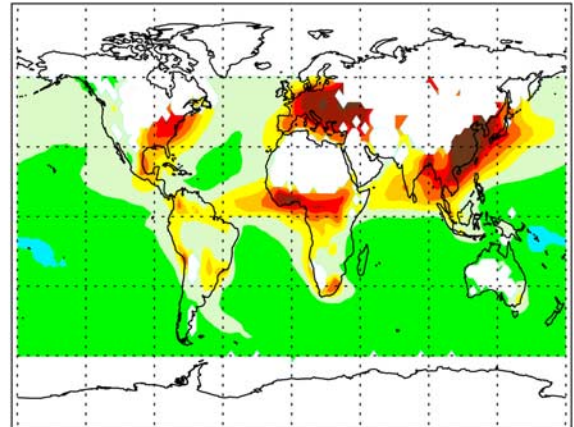
Changes in CH₂O(%) (June)Changes in CH₂O(%) (Dec.)Changes in O₃(%) (June)Changes in O₃(%) (Dec.)

Figure 10. Calculated changes in the surface concentration of CH₂O and O₃ (%) due to the formation of SOA in June and December.

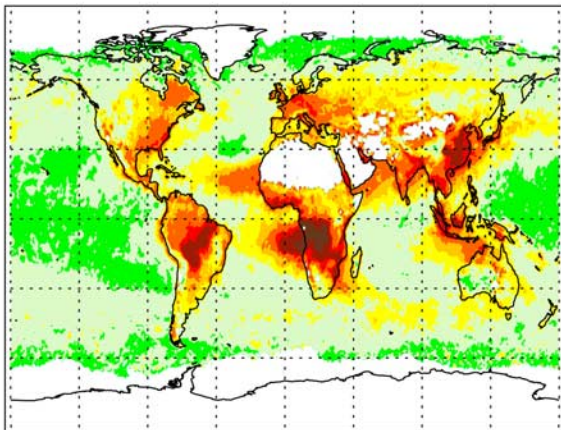
MODIS Fine Mode (Feb)



MOZART-2 Fine Mode (Feb)



MODIS Fine Mode (Sept)



MOZART-2 Fine Mode (Sept)

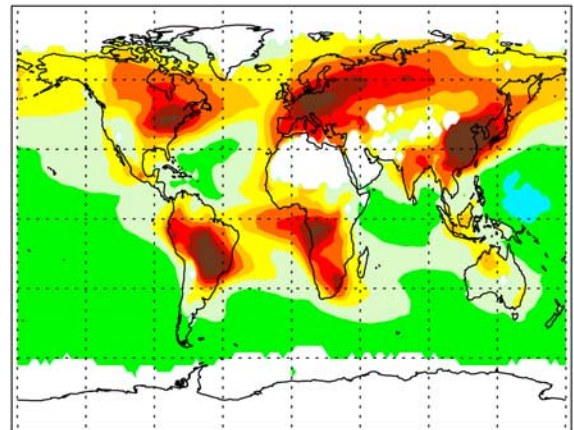
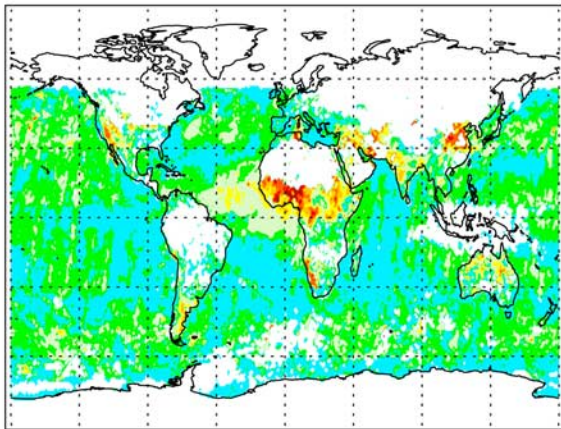
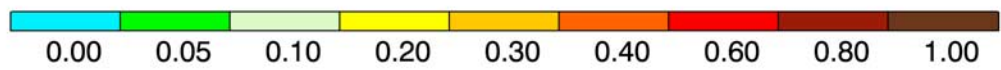
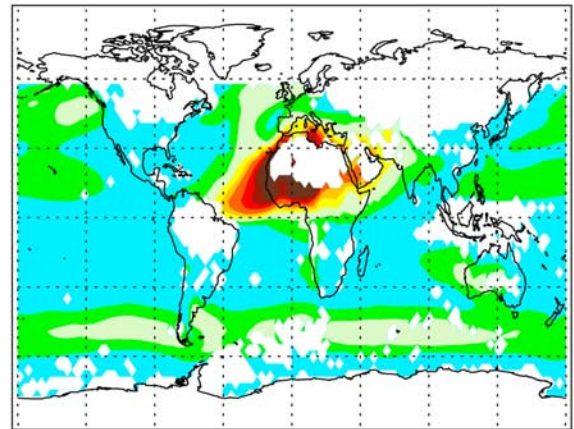


Figure 13. Calculated (right column) and observed (MODIS) (left column) optical depth at 550 nm for fine mode aerosol (including sulfate, black carbon, organic carbon, and ammonium nitrate).

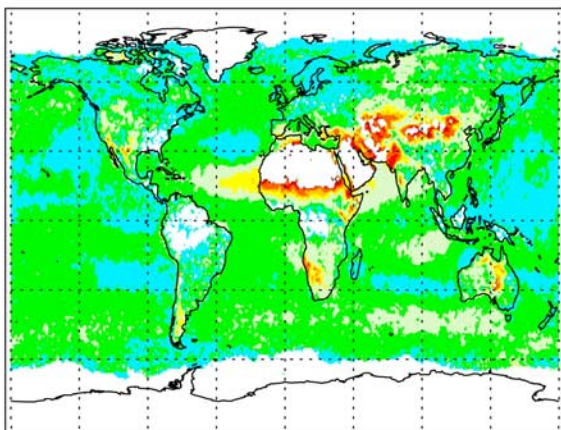
MODIS Coarse Mode (Feb)



MOZART-2 Coarse Mode (Feb)



MODIS Coarse Mode (Sept)



MOZART-2 Coarse Mode (Sept)

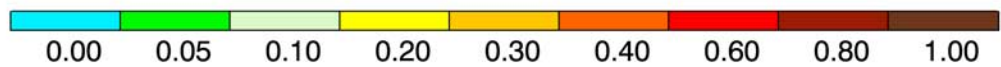
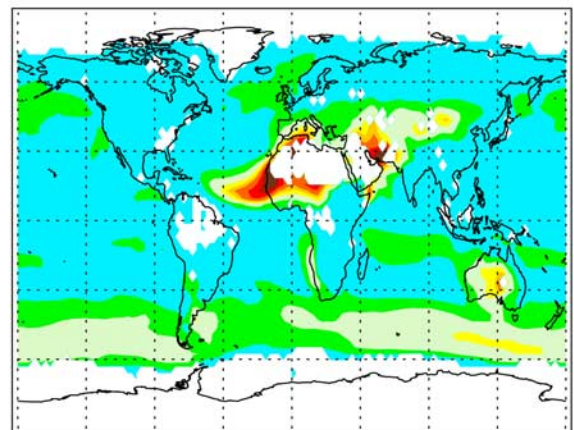


Figure 14. Calculated (right column) and observed (MODIS) (left column) total vertical optical depth at 550 nm for coarse mode aerosols (including mineral dust and sea salt).

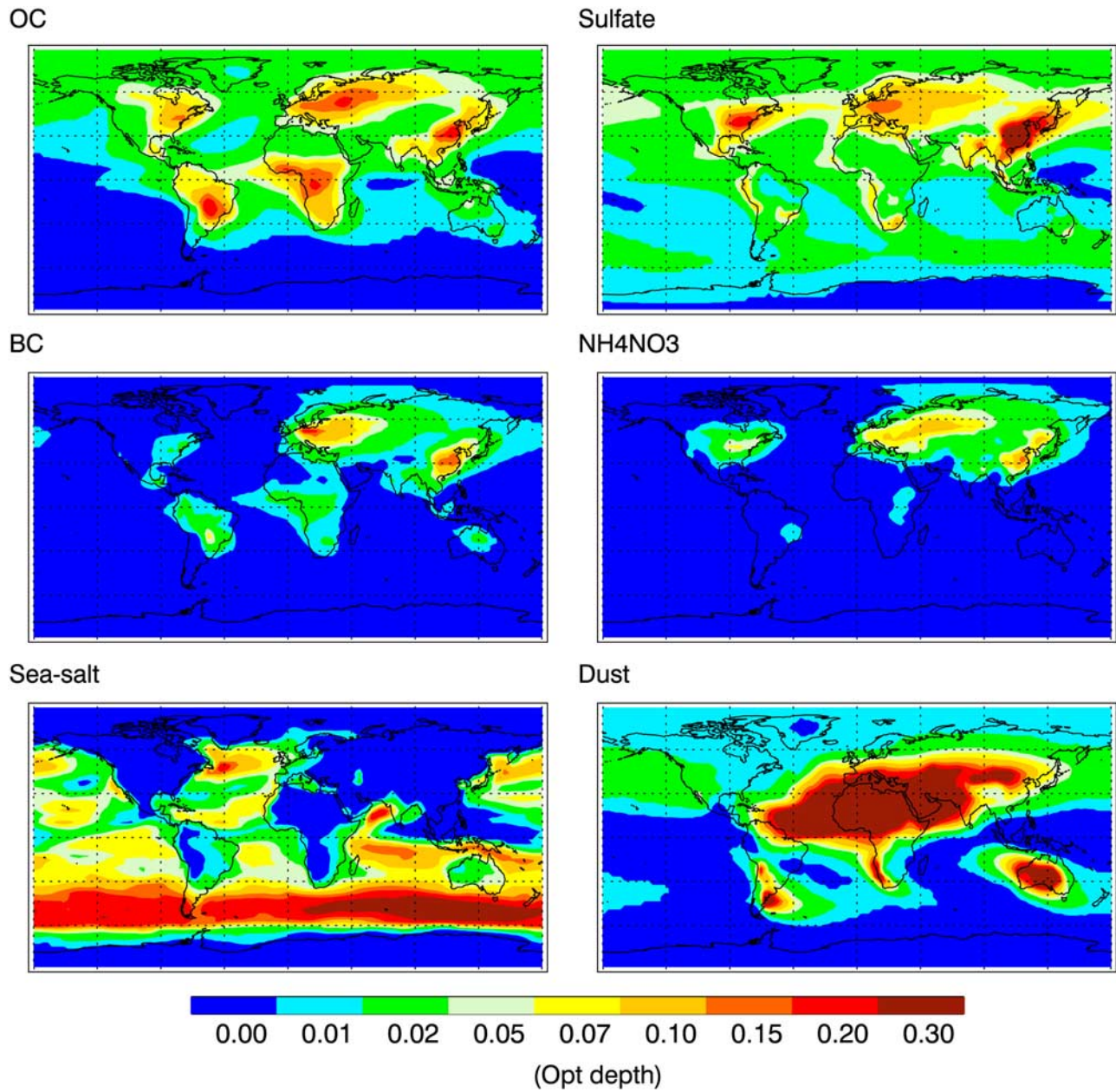


Figure 15. Calculated annual mean total vertical optical depth at 550 nm for sulfate, black carbon, organic carbon, ammonium nitrate, sea-salt, and mineral dust aerosols.

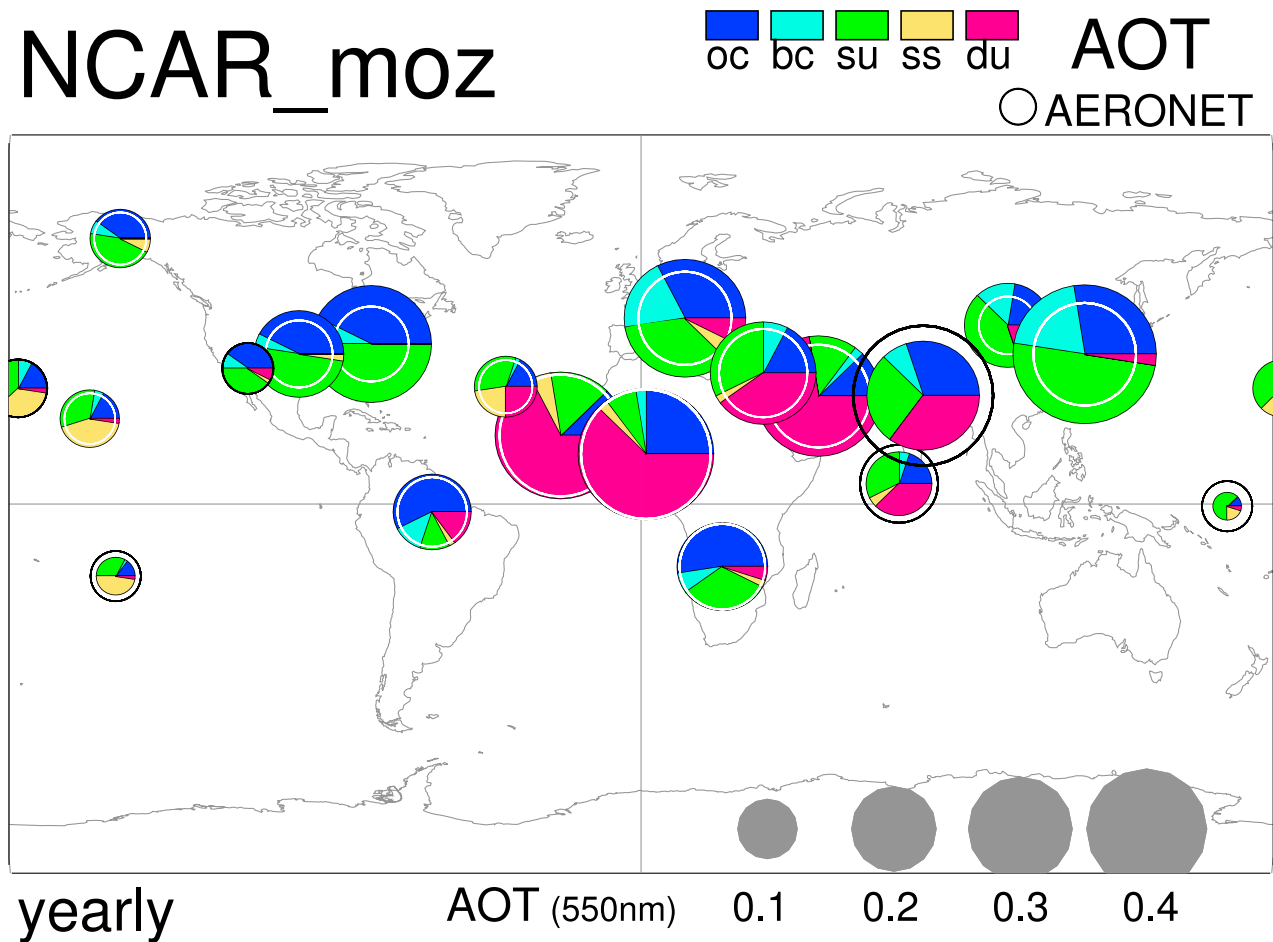


Figure 16a. Comparison between calculated and measured aerosol optical depth (AOT) at different AERONET sites. The colors represent the calculated contribution of different types of aerosols to the AOT (blue for organic carbon, light blue for black carbon, green for sulfate, yellow for sea salt, and red for dust). The circles represent the AERONET measurement for the total AOT.

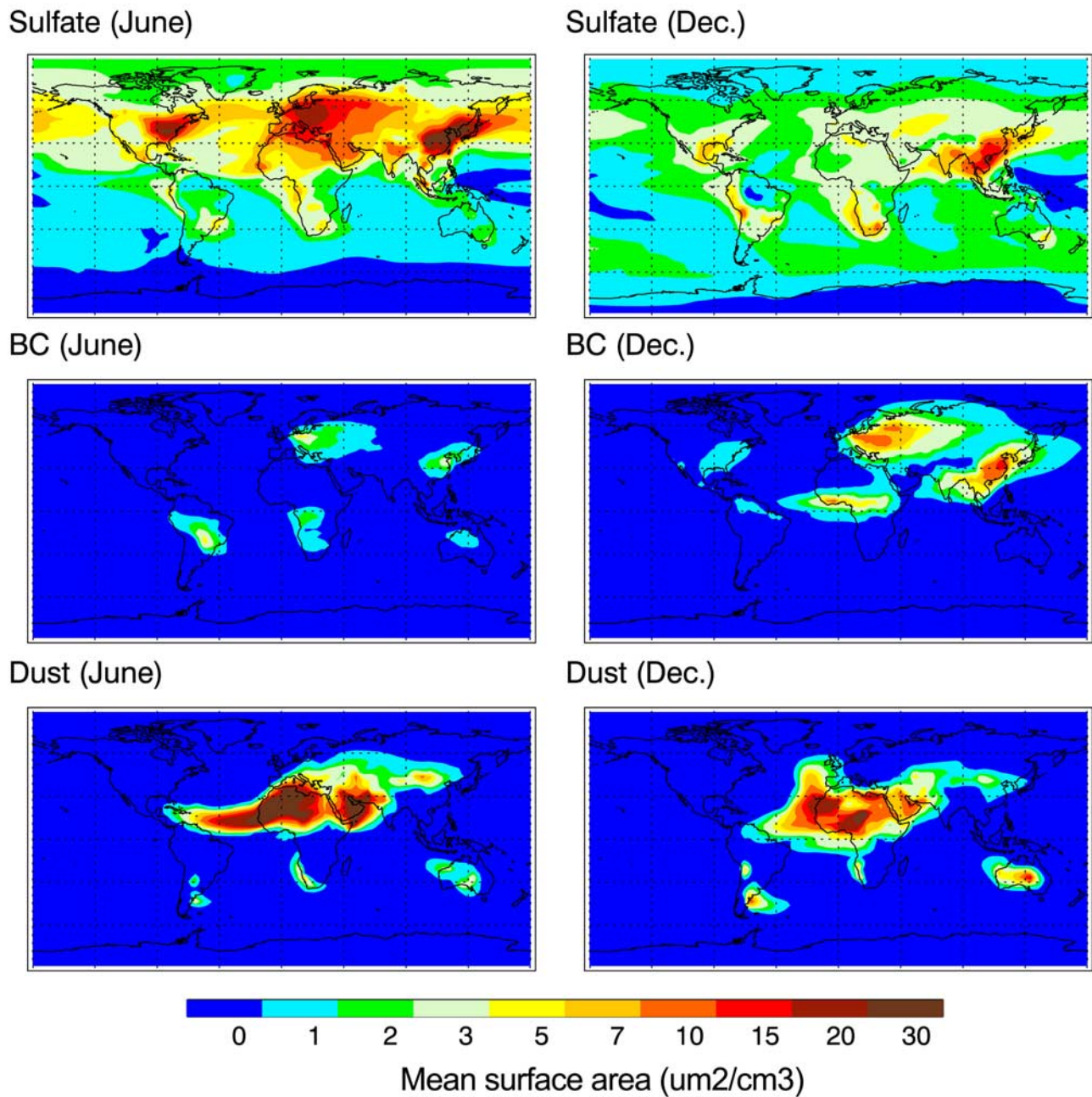


Figure 18. Calculated annual mean surface area density ($\mu\text{m}^2/\text{cm}^3$) for sulfate, black carbon, and mineral dust aerosols in June and December.

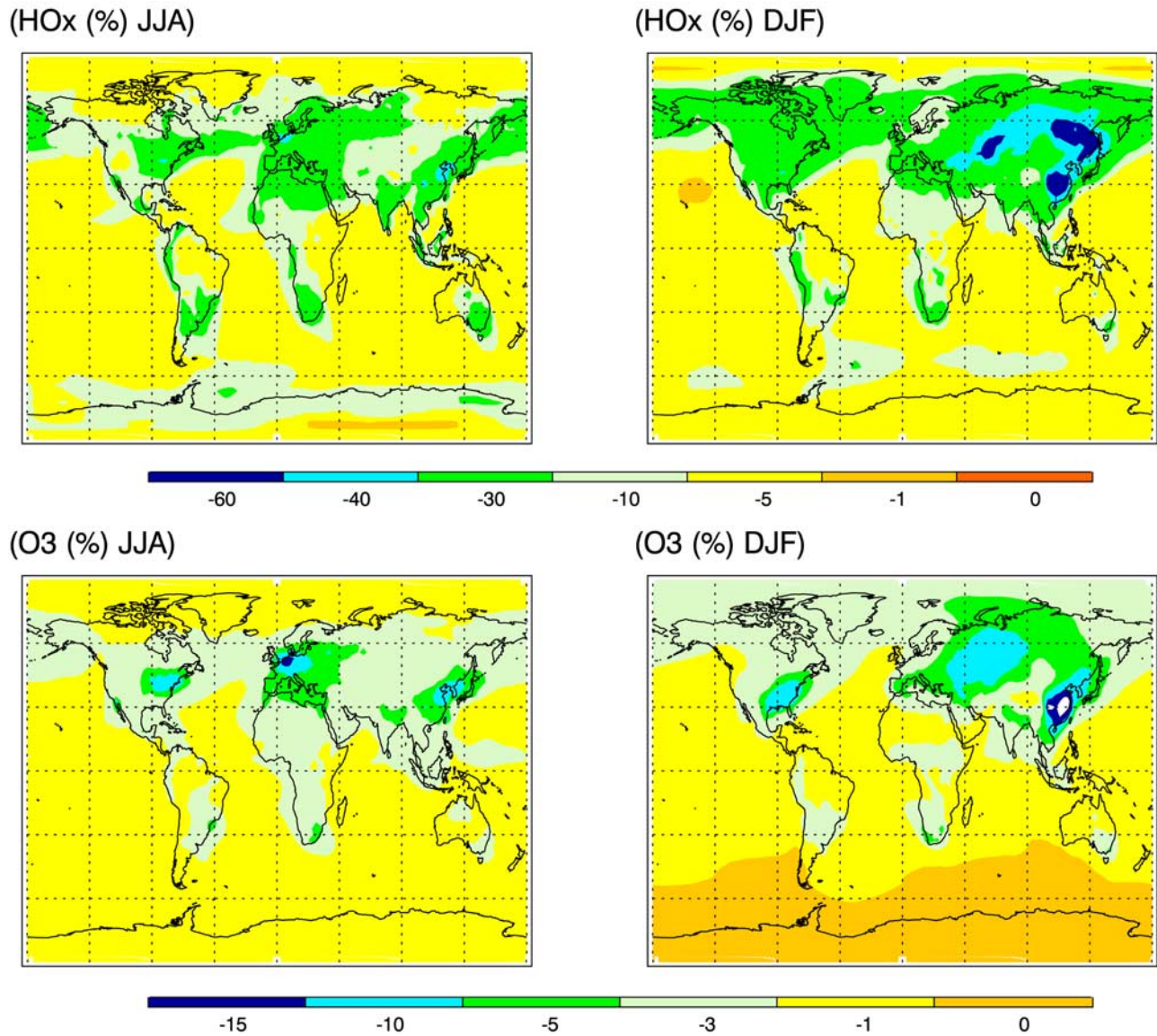


Figure 19. Calculated changes (%) in the surface concentrations of HO_x and O₃ due to heterogeneous reactions of HO₂ on sulfate, CH₂O on sulfate, and O₃ on soot in June–July–August and December–January–February.

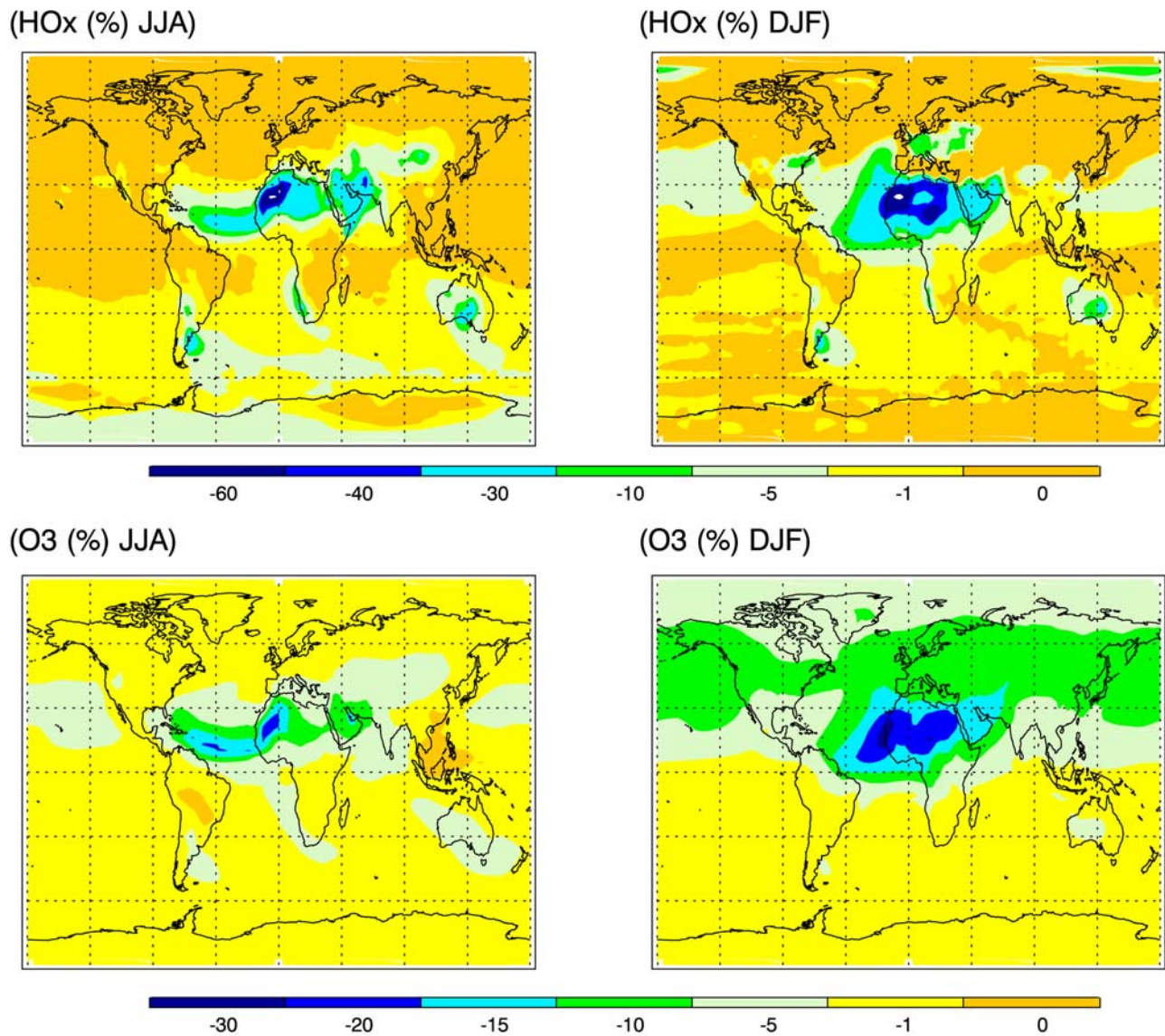
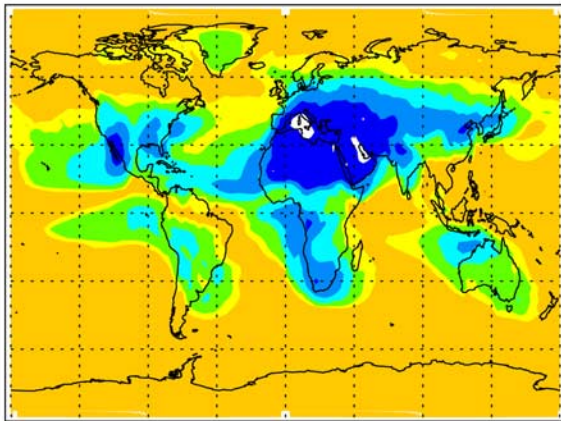
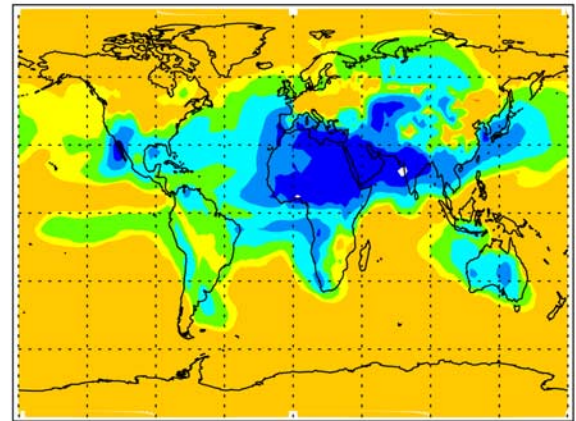


Figure 20. Calculated changes (%) in the surface concentrations of HO_x and O₃ due to heterogeneous reactions of HO₂, N₂O₅, and O₃ on dust averaged over June–July–August and December–January–February.

Change in HNO₃ (June)Change in HNO₃ (Dec.)

-1000

-300

-100

-30

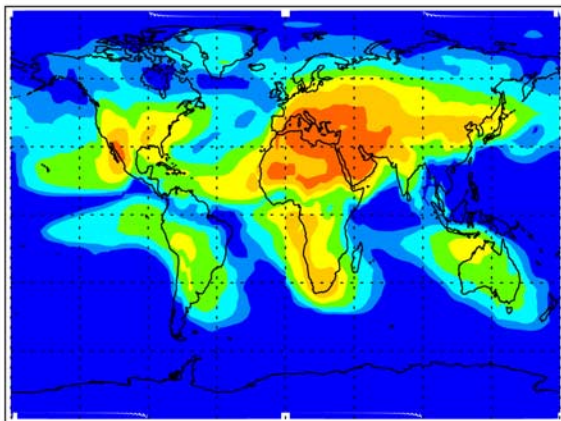
-10

-5

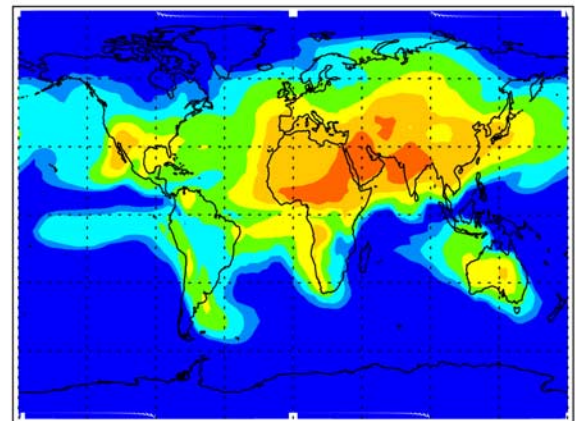
0

[pptv]

Nitrate (June)



Nitrate (Dec.)



0

5

10

30

100

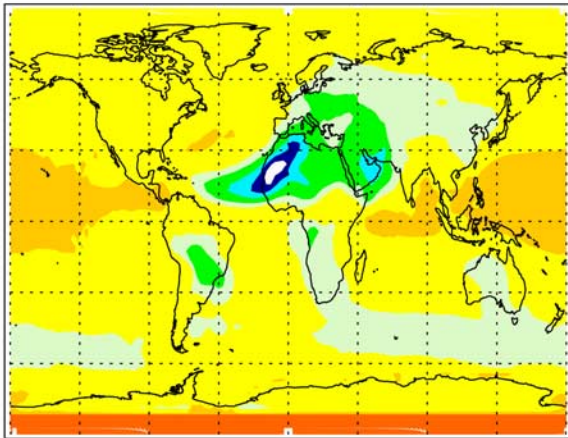
300

1000

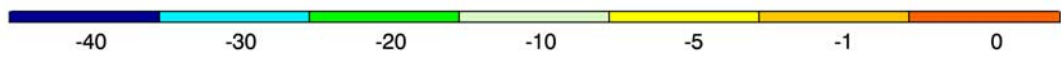
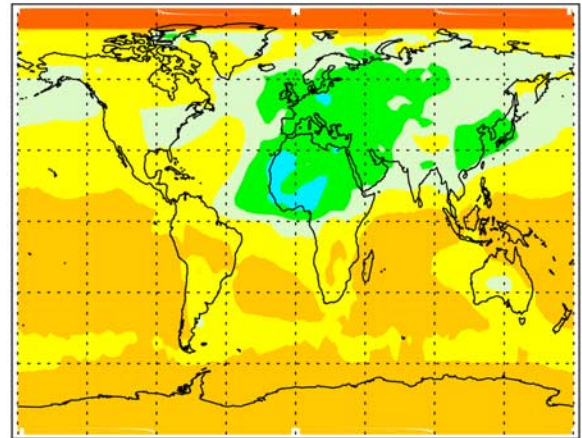
[pptv]

Figure 21. Calculated concentrations of nitrate (pptv) due to the heterogeneous reaction of HNO₃ on dust (top) at surface and (bottom) at 433 mbar in June (left panels) and in December (right panels).

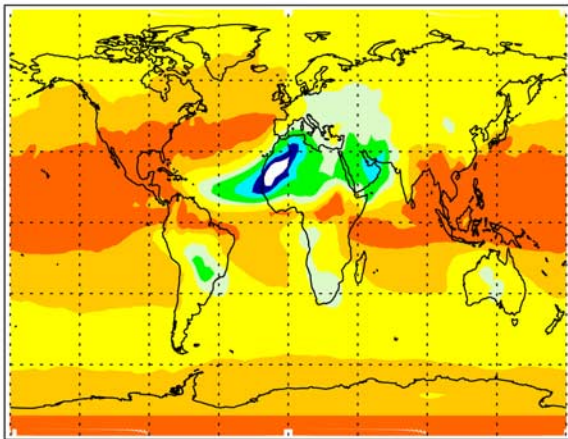
(J[O3] -> O1D JJA)



(J[O3] -> O1D DJF)



(J[NO2] JJA)



(J[NO2] DJF)

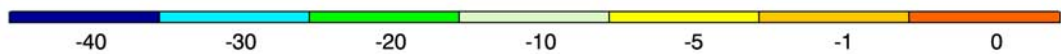
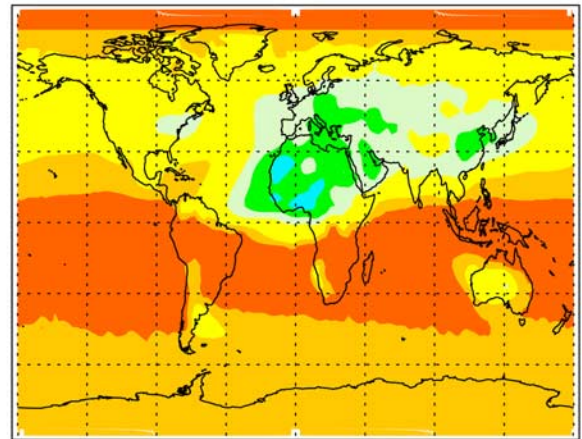


Figure 22. Calculated changes (%) in the surface photolysis frequency of O_3 and NO_2 due to the effect of aerosols on photolytic radiation averaged over June–July–August and December–January–February.

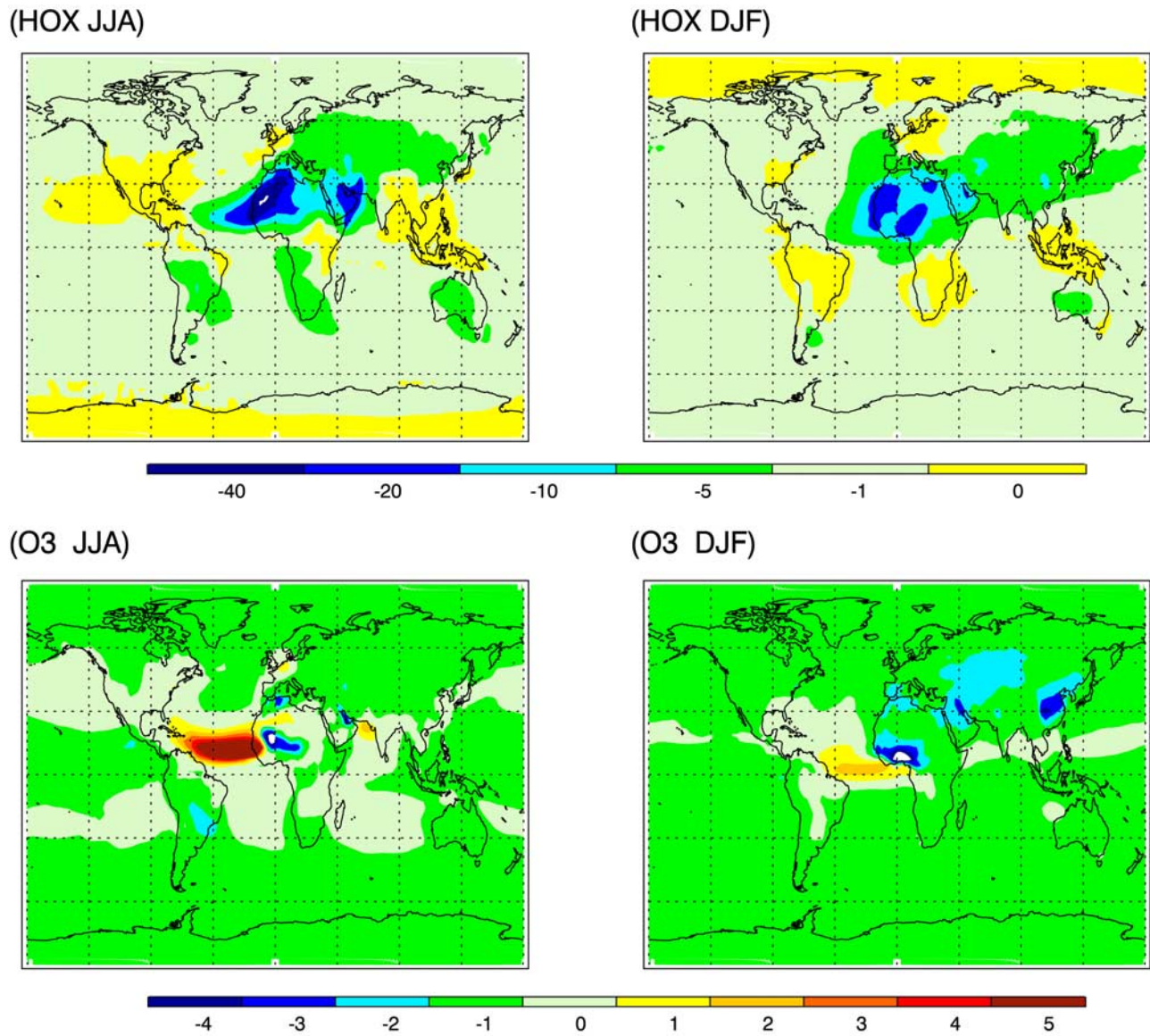


Figure 23. Calculated changes (%) in the HO_x and O₃ surface concentrations due to the effect of aerosols on radiation, averaged over June–July–August and December–January–February.